Adriano Boaron

DESENVOLVIMENTO E VALIDAÇÃO DE UM MÉTODO DINÂMICO, BASEADO EM EMISSÃO ACÚSTICA, PARA A CARACTERIZAÇÃO EM PROCESSO DE REBOLOS CONVENCIONAIS

Tese submetida ao Programa de Pós-Graduação em Engenharia Mecânica (POSMEC) da Universidade Federal de Santa Catarina (UFSC) para a obtenção do Grau de Doutor em Engenharia Mecânica.
Orientador: Prof. Dr.-Ing. Walter Lindolfo Weingaertner
Coorientadores: Prof. Dr. Eng. Júlio Apolinário Cordioli e Prof. Dr. h. c. Dr.-Ing. Eckart Uhlmann

Florianópolis
2015

Adriano Boaron

DESENVOLVIMENTO E VALIDAÇÃO DE UM MÉTODO DINÂMICO, BASEADO EM EMISSÃO ACÚSTICA, PARA A CARACTERIZAÇÃO EM PROCESSO DE REBOLOS CONVENCIONAIS

Esta Tese foi julgada adequada para obtenção do Título de "Doutor em Engenharia Mecânica", e aprovada em sua forma final pelo Programa de Pós-Graduação em Engenharia Mecânica (POSMEC)
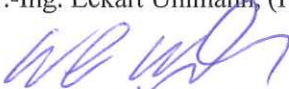
Florianópolis, 27 de março de 2015.

_____
Prof. Armando Albertazzi Gonçalves Júnior, Dr.Eng.
(Coordenador do POSMEC)

Orientador: Prof. Dr.-Ing. Walter Lindolfo Weingaertner, (LMP/UFSC)
Coorientadores: Prof. Dr. Eng. Júlio Apolinário Cordioli, (LVA/UFSC) e
Prof. Dr. h. c. Dr.-Ing. Eckart Uhlmann, (IWF/TU-Berlin)
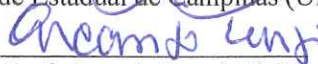
Banca Examinadora:
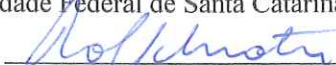
_____
Prof. Walter Lindolfo Weingaertner, Dr.-Ing. (Orientador)
Universidade Federal de Santa Catarina (UFSC)

_____
Prof. Anselmo Eduardo Diniz, Dr.Eng. (Relator)
Universidade Estadual de Campinas (UNICAMP)

_____
Prof. Arcanjo Lenzi, Ph.D.
Universidade Federal de Santa Catarina (UFSC)

_____
Prof. Rolf Bertrand Schroeter, Dr.Eng.
Universidade Federal de Santa Catarina (UFSC)

_____
Prof. João Carlos Espíndola Ferreira, Ph.D.
Universidade Federal de Santa Catarina (UFSC)

_____
Fabio Wagner Pinto, Dr.Sc.
Empresa Eins Soluções em Engenharia

Dedico este trabalho aos meus pais.

ACKNOWLEDGMENTS

Measure what is measurable, and make measurable what is not so.

(Galileo Galilei, 1564 – 1642)

RESUMO

A tecnologia de emissão acústica (EA) é utilizada no desenvolvimento de um método dinâmico para caracterização em processo (*DICM*) da topografia de rebolos convencionais. Experimentos planejados são conduzidos em uma bancada de ensaios desenvolvida, contendo um *software* de aquisição de sinais de EA. A bancada de ensaios e o *software* de aquisição possibilitam o reconhecimento de interferências entre rebolo (v_s= 30 m/s) e uma ponta de diamante, na faixa de deformação elástica das ferramentas. Os sinais de EA_{RAW} adquiridos de forma *on-line* e originados destas interferências são utilizados como dados de entrada para técnicas de processamento de sinal e para uma Rede Neural (RN). Ambas as análises são efetuadas fora do processo de retificação, representando um método dinâmico de caracterização pós-processo (*DPCM*) da topografia de rebolos. Os resultados do *DPCM* são validados através de medições específicas nas peças retificadas (p. ex., rugosidade, microscopia, camada termicamente afetada, desvio de forma) e em réplicas extraídas da topografia do rebolo. Com base nas técnicas de processamento de sinais validadas e propostas no *DPCM*, implementa-se o *DICM*. Para este método, desenvolve-se uma bancada experimental baseada na aquisição de sinais de múltiplos transdutores, na qual sinais de EA e de força são medidos. A bancada experimental e seu software de aquisição permitem a caracterização em processo da topografia de rebolos convencionais através da extração de informações quantitativas dos sinais *on-line* de EA_{RAW} adquiridos durante as interferências entre rebolo (v_s= 30 m/s) e ponta de diamante na faixa de 1 μm. A informação quantificada associada com a topografia do rebolo é baseada na análise em processo dos sinais de EA_{RAW} nos domínios do tempo e frequência. Os resultados de ambas as análises são obtidos de forma instantânea em processo sem reduzir a velocidade de corte do rebolo, e sem alterar o *setup* do processo de retificação. Visando-se otimizar o *DICM*, os principais fatores que apresentam influência sobre a resposta no domínio do tempo são analisados através de uma Análise Fatorial Fracionada. O *DICM* é validado correlacionando-se a informação quantitativa obtida da topografia, com as análises pós-processo de sinais de força de retificação e com medições da rugosidade efetiva do rebolo (parâmetro R_{ts}).

Palavras-chave: Processo de Retificação. Monitoramento de Processos. Emissão Acústica (EA). Planejamento de Experimentos (DoE). Processamento de Sinais. Redes Neurais (NN).

ABSTRACT

A Dynamic In-process Characterization Method (DICM) based on acoustic emission (AE) is developed and validated, aiming at the in-process appraisal of the topography of conventional grinding wheels. For implementing the method, planned experiments are carried out by firstly developing an AE-based experimental rig with its particular software application. This enables to recognize shallow interferences amid the grinding wheel (v_s= 30 m/s) and a diamond tip, in the elastic deformation range of the tools. The on-line acquired AE_{RAW} signals derived from such interferences are used as input data for signal processing techniques and a Neural Network (NN). Both analyses are implemented out of the grinding process and therefore consist in a Dynamic Post-process Characterization Method (DPCM). The DPCM´s results are validated by measuring both the ground workpieces (i.e. roughness, microscopy, thermally affected layer and form deviation) and the replicas extracted from the grinding wheel´s topography. Based on the validated signal processing techniques proposed by the DPCM, the DICM is implemented. This is achieved by employing a transducer-fused experimental rig in which both AE and force signals are measured. The experimental rig and its developed software application enable in-process characterization of the topography of the conventional grinding wheel by extracting quantitative information from the AE_{RAW} signals which are on-line acquired during the interferences between the grinding wheel (v_s= 30 m/s) and a diamond tip in a range of 1 μm. The quantified information associated with the grinding wheel´s topography is based on both a time domain and a frequency domain in-process analysis. The resulting outputs from these analyses are obtained instantaneously in-process by neither interrupting the grinding process nor decelerating the grinding wheel´s cutting speed. In order to define an optimized experimental condition to assess the grinding wheel´s topography, the main factors which present direct influence on the time domain output were analyzed by using a Fractional Factorial Analysis. The DICM is validated by correlating the obtained quantified information from the grinding wheel´s topography with both the post-process evaluation of the grinding cutting force and the post-process measurements of the effective roughness of the grinding wheel (parameter R_{ts}).

Keywords: Grinding Process. Process Monitoring. Acoustic Emission (AE). Design of Experiments (DoE). Signal Processing. Neural Networks (NN).

ABBREVIATIONS

A.D	After Dressing
ADC	Analog to Digital Converter
AE	Acoustic Emission
AE/MD	AE/Monitoring Device
AE-MS	AE-Monitoring System
AI	Analog Input
B	Signal bandwidth
BNC/DAC	Connectors
CBN	Cubic Boron Nitride
CD	Code width
CI	Computational Intelligence
CLP	Programmable Logic Controller
D1	Initial dressing in the experiment series
D2	Second dressing in the experiment series
DAD	Data Acquisition Device
DICM	Dynamic In-process Characterization Method
DPCM	Dynamic Post-process Characterization Method
FFT	Fast Fourier Transform
Force/MD	Force/Monitoring Device
Force-MSC	Force-Multichannel Signal Conditioner
FSO	Full Scale Output
HP	High-Pass filter
IWF	*Institut für Werkzeugmaschinen und Fabrikbetrieb*
LMP	*Laboratório de Mecânica de Precisão*
LP	Low-Pass filter
N	Number of AE digitized points that overstep a fixed predefined threshold during t_{scan}
NC	Numerical Control
NN	Neural Networks
POSMEC	*Programa de Pós-Graduação em Engenharia Mecânica*
PSD	Power Spectral Density function
RMS	Root Mean Square
SEM	Scanning Electron Microscopy
SOM-NNs	Self-Organizing Maps Neural Networks
SR	Signal Range
T.S	Type of Signal (AE_{RAW} or AE_{RMS})
TU-Berlin	*Technische Universität Berlin*
UFSC	*Universidade Federal de Santa Catarina*
USB	Universal Serial Bus cable

SYMBOLS

A	V	AE wave amplitude
AE_{RAW}	V	Acoustic emission raw signal
AN	-	Proportionality constant
A_{rep}	mm^2	Measuring area on grinding wheel´s replicas
C_1	mm^{-3}	Cutting edge density
C_{stat}	mm^{-3}	Static cutting edge density
E_s	mm	Grinding wheel´s radial runout
F_n	N	Normal force
$F´_n$	N/mm	Specific normal force
F_t	N	Tangential force
$F´_t$	N/mm	Specific tangential force
F_x	N	Grinding cutting force component (along the x-axis of the dynamometer)
F_y	N	Grinding cutting force component (along the y-axis of the dynamometer)
F_z	N	Grinding cutting force component (along the z-axis of the dynamometer)
H(f)	Hz	Frequency response
L_{eff}	mm	Effective width of the grinding wheel
L_{kin}	mm	Kinematic cutting edged distance
L_{scan}	mm	AE tactile scanning length
$L_{static,average}$	mm	Average static grain separation
M_z	N.mm	Torque around the Z-axis of the dynamometer
N	number	AE oversteps
N_{AX}	number	Average value of N (AE oversteps) by using the axial scanning trajectory
N_{kin}	mm^{-2}	Number of kinematic cutting edges per surface area
N_{mom}	-	Momentary cutting edge number
N_{stat}	mm^{-2}	Cutting edge density per surface unit
N_{TAN}	number	Average value of N (AE oversteps) by using the tangential scanning trajectory
O_s	mm	Grinding wheel´s circularity error
$Q´_w$	$mm^3/mm.s$	Specific material removal rate
R_a	µm	Arithmetic mean surface roughness
R_{pk}	µm	Reduced peak roughness
R_{sk}	µm	Surface roughness skewness

R_{tip}	μm	Radius of the single-point diamond tip
$R_{tip/A}$	μm	Radius of the single-point diamond tip (after experiments)
$R_{tip/B}$	μm	Radius of the single-point diamond tip (before experiments)
R_{ts}	μm	Actual grinding wheel surface roughness
R_{vk}	μm	Reduced valley roughness
$R_{xx}(\tau)$	-	Autocorrelation function
R_z	μm	Surface roughness depth
$Smr(c)$	%	Material proportion of the surface as a function of the height (c)
S_{stat}	mm^{-1}	Number of cutting edges per unit length
$S_{xx}(f)$	V^2/Hz	Power spectral density (PSD) function
T_h	V	Threshold: set fixed limit based on the AE signal
$T_{scratch}$	s	Total time duration of the AE_{RAW} signal regarding the Scratch Experiments
U	V	Voltage analog signal
U_d	-	Overlap ratio
V'_w	mm^3/mm	Specific material removal
X	-	Random variable
$\{X(t)\}$	-	Set of realizations (ensemble)
W_s	mm	Overall waviness of the grinding wheel
a_e	mm	Depth of cut
a_{ed}	μm	Depth of dressing cut
$a_{e,scan}$	μm	AE tactile scanning depth
a_p	mm	Width of cut
b_d	mm	Active width of the dressing form roller
b_s	mm	Grinding wheel width
d_{eq}	mm	Equivalent grinding wheel diameter
d_r	mm	External diameter of the dressing form roller
d_s	mm	Grinding wheel diameter
d_w	mm	Workpiece diameter
$f_{cut-off}$	Hz	Cut-off frequency
f_{MAX}	Hz	Maximum frequency content in the analog signal

f_s	Samples/s	Sampling rate
f_{stop}	Hz	Maximum frequency content in the transition band
h_{cu}	µm	Statistically average maximum underformed chip thickness
n_w	min^{-1}	Number of workpiece revolutions
q	-	Rotational ratio between the grinding wheel and the workpiece while plunge grinding
q_d	-	Dressing speed ratio
r_{stylus}	µm	Stylus´ tip radius
t_{scan}	s	AE tactile scanning duration
$v_{fa,scan}$	mm/min	Axial velocity during AE tactile scanning
v_{fad}	mm/min	Axial dressing feed rate
v_{fr}	mm/min	Radial infeed velocity
v_R	m/s	Circumferential speed of the dressing form roller
v_s	m/s	Cutting speed
v_{sd}	m/s	Circumferential speed of the grinding wheel during dressing
v_w	m/s	Workpiece circumferential speed
$\bar{x}$	V	Mean value of the digitized AE_{RAW} signal (time domain estimate)

α	%	Statistical significance level
δ	µm	Thermally affected layer
$\delta T_{scratch}$	s	Segmented time duration of the AE_{RAW} signal regarding the Scratch Experiments
Δ_c	µm	Interference depth during contact recognition
Δ_R	mm	Diameter deviation
ΔT	ms	Integration time constant
λ_c	mm	Wavelength cut-off for roughness measurements
$\hat{\sigma}_x$	V	Estimation of the standard deviation
σ_x	V	Standard deviation
$\bar{\sigma}_x$	V	Average standard deviation of the ensemble

CONTENTS

1 INTRODUCTION

In the context of today´s globalized and competitive manufacturing industry, the trend towards a sustainable and effective production requires constant process optimization. Therefore, technical and innovative solutions which permit both a better use of the available resources and product quality are unremittingly in evidence. Among the wide range of machining processes, the grinding process is usually used when parts with close tolerances and high surface quality are demanded. As grinding is normally placed at the end of the manufacturing chain, errors and unexpected faults must be avoided, otherwise it results in high production costs and also scraped components.

Due to the technological developments regarding innovative machine tools and machining strategies in grinding, higher cutting speeds and higher material removal rates are continuously employed. Thus, the grinding tools are often utilized at the limit of their physical properties and capabilities (KLOCKE; KÖNIG, 2005; MARINESCU et al., 2007).

Despite the continuous trend for using superabrasive grinding wheels in production lines, conventional grinding wheels still play an important role in several industry applications. Fused aluminum oxide grinding wheels represent a particular class of conventional grinding wheels which are often employed in industry. In comparison with superabrasive grinding wheels, fused aluminum grinding wheels enable efficient process due to their higher profile flexibility (easy dressing of contours and forms) and lower machine tool requirements (i.e., low power demand) (ROWE et al., 2004).

Among the existing disturbances in the grinding process, the continuous variation of the grinding wheel´s topography during the process as well as the random distribution of grains over its topography represent a major challenge for process control and automatization. Such disturbances take place when employing both conventional and superabrasive grinding wheels (DAVIS et al., 1995; KÖNIG, 1989).

On account of the actual techniques used to manufacture conventional grinding wheels, the repeatability of the production of grinding tools in terms of their properties, and the forecast of their in-process behavior are very difficult and present an increasing importance for process control. Small variations in the properties of the grinding wheels often have significant influences on the grinding process (KLOCKE; KÖNIG, 2005; ROWE, 2009).

In addition, owing to the complex structure of the conventional grinding wheels, a general association between the known specifications (as delivered by the grinding wheel manufacturer) and the in-process behavior of the tool is not possible. This prevents the implementation of databases for the selection of grinding wheels for specific workpiece materials and machining tasks. It is required to establish a procedure which could be internationally adopted aiming at a suitable process programming independently from the manufacturing source of the grinding wheel (ROWE et al., 2004). Many research works and studies have been conducting in order to develop methods to evaluate the topographic characteristics of the grinding wheels, but the success for in-process prediction has been still limited (LACHANCE; WARKENTIN; BAUER, 2003; ROWE et al., 2004).

In the wake of such a context, the determination of an experimental approach which allows in-process characterizing the topography of conventional grinding wheels consists the main goal to be achieved in the scope of the current doctoral research. The suggested experimental approach comprises two complementarily experimental methods: a) Dynamic Post-process Characterization Method (DPCM) and; b) Dynamic In-process Characterization Method (DICM). The grinding wheels´ topographic characterization in both the DPCM and the DICM is implemented through a specific technique based on the on-line detection of AE_{RAW} events resulting from minimal interferences (about 1 μm) between a grinding wheel and a single diamond tip dressing tool. The proposed technique enables to detect the active kinematic cutting edges on the grinding wheel´s topography, in order to extract relevant information about the variations occurring in its topography over the experiments.

The DPCM aims at defining and validating a reliable AE-based procedure for characterizing the topography of the investigated fused aluminum oxide grinding wheel, after stopping the grinding process (post-process analysis). This is carried out by using appropriate signal processing techniques (both in the time and frequency domain) based on the AE signals acquired during the experiments. Additionally, a Self-Organizing Map (SOM) neural network technique is utilized in order to cluster the different wear states of the grinding wheel over the experiment series. The validation of the DPCM occurs by evaluating the grinding results on the ground workpieces (roughness, form deviation, thermally affected layer, and microscopy images) and on the replicas extracted from the grinding wheel´s topography.

Based on the signal processing techniques employed and validated by the DPCM, further similar experiments are carried out in order to validate the proposed DICM. The DICM has the main goal of defining and validating a suitable AE-based quick test method (AE Quick Test Method) for the in-process characterization of the topography of a similar conventional grinding wheel. The in-process characterization of the grinding wheel´s topography by means of the proposed AE Quick Test Method consists in the great novelty and contribution of the current research. In order to optimize the time domain outputs derived from the AE Quick Test Method, a Fractional Factorial Analysis is conducted, based on the factors which exert influence on the time domain output. The validation of the proposed AE Quick Test Method is carried out by correlating the obtained quantified information associated with the topography of the grinding wheel (through time and frequency domain in-process analysis) with the post-process measurements of the grinding cutting force (components F_t and F_n) and with the effective roughness of the grinding wheel (parameter R_{ts}), after grinding specimens without spark-out time.

The current research has been conducted in the scope of a sandwich doctorate work which is inserted in the context of the international cooperation program called Bragecrim (Brazilian–German Collaborative Research Initiative on Manufacturing Technology) and within the project named "A Quick Test Method for the Characterization of In-Process Properties of Conventional Grinding Wheels". The activities were carried out in a partnership between the LMP (*Laboratório de Mecânica de Precisão*) at UFSC (*Universidade Federal de Santa Catarina*), in Florianópolis, Brazil, and the IWF (*Institut für Werkzeugmaschinen und Fabrikbetrieb*), at TU-Berlin (*Technische Universität Berlin*), in Berlin, Germany.

The structure of this doctoral thesis is as follows: In Chapter 2, the main concepts related to the state of the art concerning the fundamental topics of the current research are mentioned. Chapter 3 highlights the problem description and the motivation to conduct the research. In Chapter 4, the devices and measuring methods which have been used for accomplishing the goals of the research are described. Chapter 5 describes the experimental planning and the proposed methodology. Chapter 6 describes and discusses the achieved results in the scope of this research as well as the main procedures and measurements for validating the results. In Chapter 7, the conclusions derived from the current research are summarized and the suggestions for future works are also presented.

2 STATE OF THE ART

2.1 BASIC ASPECTS OF THE GRINDING PROCESS

The grinding process is largely used as a precision machining process in which chip formation occurs within the range of a few micrometers and to a large extent hampers direct observation. Grinding can usually be described independently of the grinding method being used. This is achieved with the help of appropriate grinding parameters or characteristics. Various process parameters allow a systematically comprehensive evaluation of the distinct grinding strategies, and offer the grinding technician the possibility of comparing various existing methods. Furthermore, it is also possible to interpret the process´s outputs in order to optimize the grinding process. The most important parameters in grinding can be subdivided into input, process and resulting parameters (KLOCKE; KÖNIG, 2005; KÖNIG, 1989), Figure 1.

Figure 1 – Grinding process parameters.

Input Parameters		Process Parameters	Resulting Parameters
System / **Variables**		Process Characteristics	Technology
Machine -Type - Properties	**Primary** Depth of cut	Force	**Workpiece** - Accuracy of shape - Accuracy of dimension - Surface quality - Damage of the surface layer
Workpiece - Geometry - Material	Workpiece speed	Power	
Grinding Wheel - Geometry - Specification	Feed rate Cutting speed	Grinding wheel wear Temperature	**Grinding Wheel** - Wear - Clogging/Loading
Dressing Tool - Type - Specification	**Secondary** Dressing conditions	Grinding duration Acoustic Emission	**Cooling Lubricant** - Contamination - Property changes
Cooling Lubricant - Type - Supply	Coolant pressure Flow rate	**Disturbances** Vibrations Temperatures	Efficiency - Productivity - Manufacturing costs

Source: Adapted and based on (KLOCKE; KÖNIG, 2005; KÖNIG, 1989).

The input parameters are divided into both system and variable parameters. Among the system parameters are those related to the

machine, workpiece, grinding wheel, dressing tool, and cooling lubricant. On the other hand, the variable parameters can be subdivided into primary and secondary parameters. The primary variable parameters describe the kinematics of the grinding process and the resultant material removal during the grinding process. The secondary variable parameters are associated with the conditioning of the grinding wheel as well as additional aspects regarding lubrication conditions.

Process characterization is carried out by correctly interpreting the main process parameters with the measurement of acoustic emission, grinding force, power, temperature, grinding wheel wear and process duration. External disturbances on the grinding process (e.g., vibrations and temperature) directly influence the process efficiency, thus affecting the final quality of ground products.

The outputs from the grinding process are evaluated by considering the resulting parameters, which in turn can be subdivided into both technological and efficiency aspects. Technological aspects are generally related to the workpiece, the grinding wheel and the cutting fluid, whereas the efficiency aspects comprise the process viability and overall costs (KÖNIG, 1989).

2.1.1 External Cylindrical Peripheral Plunge Grinding

The external cylindrical peripheral plunge grinding (also called external cylindrical infeed grinding, or even outer diameter plunge grinding) is commonly utilized in industrial praxis for machining bearing carriers, shaft cranks and grooves (KLOCKE; KÖNIG, 2005). Such grinding process is characterized by a linear and continuous infeed movement of the grinding wheel against the workpiece´s surface. The infeed movement of the grinding wheel normally occurs either in the radial direction (labelled as v_{fr}), or at an specific angle in relation to the workpiece´s axis, Figure 2 (ROWE et al., 2004).

The infeed movement can be subdivided into several process stages, which are characterized by the fact that, for each further stage, there is a smaller specific material removal rate. Throughout the spark-out stage, no radial infeed occurs, and therefore shape errors due to deformations caused by machining forces can to some extent be balanced out (DAVIS et al., 1995; KLOCKE; KÖNIG, 2005).

Figure 2 – Input variable parameters and grinding force components on external cylindrical peripheral plunge grinding.
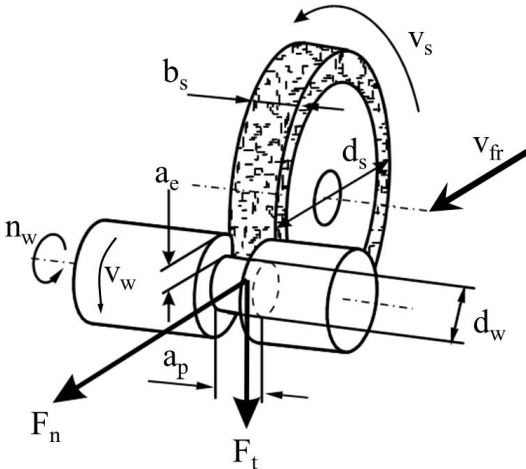
Source: Adapted and based on (DIN8589-11, 2003; KÖNIG, 1989; MARINESCU et al., 2007).

Simultaneously to v_{fr}, the workpiece and the grinding wheel rotate with predefined peripheral velocities (v_w and v_s, respectively) by usually employing a velocity ratio of 1:60 ($v_w = v_s/60$). The interaction between the grinding wheel and the workpiece under such process conditions leads to the material removal on the surface of the workpiece. Due to the combined interaction of both v_{fr} and v_w during the process, the ground surface presents usually a geometric deviation form (cross-section as spiral form), which is proportional to the magnitude of v_{fr} per rotation of the workpiece. Figure 2 also detaches complementary parameters used on the external cylindrical peripheral plunge grinding process. Among those parameters, the most important are the width of cut (a_p), the depth of cut (a_e), the grinding wheel´s diameter (d_s), the workpiece´s diameter (d_w), the cutting speed (v_s), the workpiece´s circumferential speed (v_w), and the number of revolutions of the workpiece (n_w). Additionally it is also shown the main components of the grinding force, namely the normal force (F_n) and the tangential force (F_t) (DAVIS et al., 1995; KÖNIG, 1989; MARINESCU et al., 2007).

2.2 MAIN DISTURBANCES IN GRINDING

As a consequence of the intense push for low manufacturing costs, high productivity and high quality products, both the monitoring

and the feedback control of the grinding process (by controlling for example: grinding wheel wear, contact recognition for gap elimination, grinding wheel loading, thermal damage of the workpiece, chatter, truing/dressing verifications, etc.) are increasingly required by industry. This necessity motivated wide research in the field of grinding process monitoring over the past decades (DORNFELD; LEE, 2008; LEE et al., 2005; LIAO, 2010; LINKE, 2007; WEBSTER; DONG; LINDSAY, 1996).

        The grinding process is influenced by both periodic and stochastic disturbances whose effects cannot always be fully compensated in non-monitored process. The behavior of the effective grinding wheel´s life is subjected to unpredictable dispersions which lead in automated manufacturing processes to a conservative process design in order to assure the target quality level. Nevertheless, inconsistent machining sequences and workpieces can still often be found (KÖNIG; MEYEN, 1990).

        Besides the variation in the initial condition of the workpieces (hardness, composition, etc.), other significant disturbances in grinding are the varying grinding wheel properties, dressing tool wear as well as operator-related parameter modifications, Figure 3.

Figure 3 – Disturbances in the grinding process and necessity for monitoring.
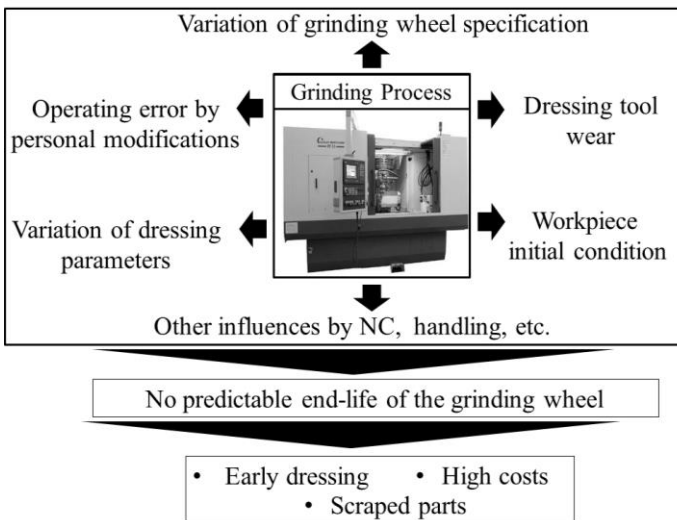
Source: Adapted and based on (DAVIS et al., 1995; KLOCKE; KÖNIG, 2005).

All the mentioned disturbances in the grinding process conduct to unpredictable fluctuations in the grinding wheel´s life, which in turn lead to significant process waste as for example, early dressing, scraped parts and high costs. In order to meet the ever-increasing requirements for reliable and flexible production, the grinding process should become more self-directed, and also independent from misinterpretations (INASAKI, 1998). In addition, the availability of modern numerical controlled (NC) grinding machines in recent years is accelerating the need for making the grinding process more autonomous (INASAKI, 1999; KARPUSCHEWSKI, 2001; MALKIN; GUO, 2008).

2.3 ACOUSTIC EMISSION IN GRINDING

When a material is deformed by an external stimulus, as occurring in grinding operations (contact and friction between grits and workpiece) the lattice structure of the material is distorted and rearranged. This process provides enough energy and generates elastic tension waves within a material, also known as Acoustic Emission waves (often just called AE). These AE waves travel in a solid, liquid and gas medium and can be detected by a suitable AE transducer (DORNFELD; LEE, 2008; KÖNIG; MEYEN, 1990; LINKE, 2007; LIU; CHEN; GINDY, 2005; MOKBEL; MAKSOUD, 2000; SUSIC; GRABEC, 2000).

AE waves spread within a medium as a volumetric propagation, that is, they present both longitudinal and traversal motion components. The amplitude of the AE wave (A) depends on its distance (r) from the AE source, and this dependence can approximately be defined as Equation 1, (DORNFELD; LEE, 2008; LINKE, 2007; MARGOT, 2005).

$$A \approx \frac{1}{r} \tag{1}$$

Equation 1 detaches the need for using AE transducers as close as possible to the AE source for achieving correct process monitoring.

2.3.1 Sources of Acoustic Emission in Grinding

The grinding process is characterized by the random interaction of a large quantity of cutting edges on the surface of the workpiece. All the individual contacts caused by the grits can be considered as a source of pulse deformation or stress energy on

the workpiece. Figure 4 exemplifies the major AE sources that can be found in the grinding process (DORNFELD; LEE, 2008; KARPUSCHEWSKI, 2001; LINKE, 2007).

      During the grinding process, as the wear of grains increases over time, the individual characteristics of the grinding wheel also change, leading to different cutting edges and grain distributions on the periphery of the grinding wheel (LACHANCE; WARKENTIN; BAUER, 2003). Therefore, many distinct sources of AE in grinding need be considered.

Figure 4 – Sources of AE in grinding.
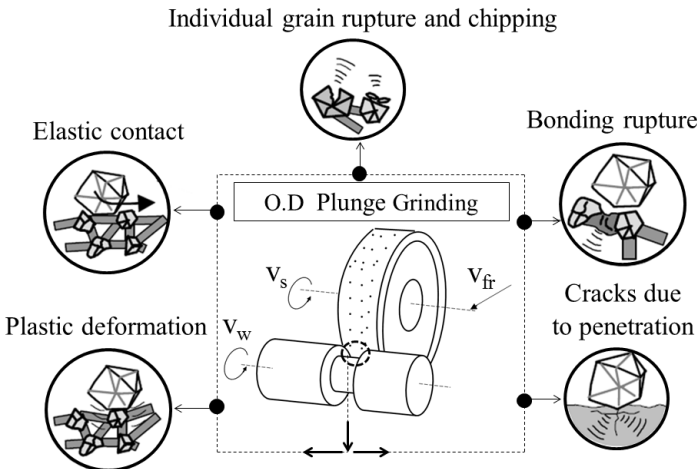
Source: Adapted and based on (DORNFELD; LEE, 2008; KARPUSCHEWSKI, 2001; LINKE, 2007).

      AE events in the grinding process derive from the combination of singular sources as the grain penetration on the workpiece´s surface (elastic and plastic deformation), cracks due to penetration, bonding rupture as well as the individual grain rupture and chipping. Additionally, changes in the workpiece´s microstructure due to thermal loads also act as potential source of AE during the grinding process (BIFANO; YI, 1992; DIMLA, 2000; DORNFELD; LEE, 2008; HASSUI et al., 1998; KARPUSCHEWSKI, 2001; LINKE, 2007).

2.3.2 Acoustic Emission Frequency Range in Grinding

The frequency range in which AE signals are feasibly employed to monitoring the grinding process is not exactly defined. Usually, the characteristic frequency range varies from about 30 kHz up to 1 MHz, thus highly above the audible frequencies, and also higher than the major environmental noises external to the grinding process. The lower and upper limits of the AE frequency range are at the same time influenced by the constructive and technical characteristics of the AE transducer (DORNFELD; LEE, 2008; HASSUI et al., 1998).

During the grinding process, some disturbances are associated with moving components in the grinding machine. The influence of such disturbances is accentuated in lower frequency ranges, and is considerably reduced in higher frequency ranges. The most significant disturbances related to the constructive aspects of the grinding machine (i.e., motor, transmission, machine, etc.) are situated in the frequency range of about 10 Hz up to 300 Hz, Figure 5 (BIFANO; YI, 1992; HASSUI et al., 1998; KÖNIG; ALTINTAS; MEMIS, 1994; RAVINDRA; SRINIVASA; KRISHNAMURTHY, 1997).

Figure 5 – AE spectrum in grinding and its related disturbances.
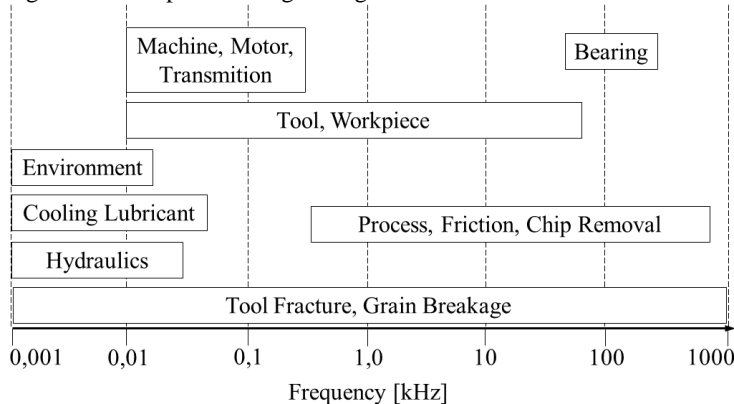
Source: Adapted and based on (KLOCKE; KÖNIG, 2005; MARGOT, 2005).

Hydraulic noise and electrical disturbances commonly exhibit magnitudes which do not considerably influence the spectrum in grinding. Disturbances may also take effect due to the flow of the cooling lubricant. Nevertheless, their intensities decrease expressively above 15 kHz up to 20 kHz, so that in this condition a high-pass filtering

affords enough isolation of the grinding process signal (KLOCKE; KÖNIG, 2005). The disturbances caused by bearings can reach higher frequencies which lie inside the grinding spectrum and may cause false interpretation of the AE signals. When possible, the critical disturbances shall be reduced by choosing the proper positioning of the AE transducer in the grinding machine, or by employing suitable analog filters in the measuring chain (MARGOT, 2005).

2.4 GRINDING WHEELS TOPOGRAPHY

In a general perspective, the term topography refers to the definition and mapping of the shape of a particular surface (ROWE et al., 2004). The topography of a grinding wheel can be summarized as being the sum and interaction of both macro and microgeometric quantities on the grinding wheel´s surface (also labelled as macrotopography and microtopography) (TÖNSHOFF; FRIEMUTH; BECKER, 2002). The macrotopography as well as the microtopography change during the grinding process due to the inherent wear behavior of the grinding wheel, which therefore is strongly related to the grinding process, the dressing parameters, and to the structure of the grinding wheel (ROWE et al., 2004).

The grinding wheel´s shape is part of the macrotopography and is important for the overall accuracy of the ground workpiece´s profile (ROWE et al., 2004). The basic macrotopographic aspects associated with the grinding wheel can be resumed as the diameter deviation Δ_r, the radial runout E_s, and the circularity deviation O_s. The sum of these macrotopographic aspects leads to the overall waviness W_s in grinding wheels, Figure 6-a (MARINESCU et al., 2007; ROWE et al., 2004).

The microtopographic characteristics are defined by the shape of the cutting edges and are directly influenced by the grinding wheel's wear which conducts to the flattening and the breakage of grains as well as to the loading of the grinding wheel and to the drop-out of grains, Figure 6-b. The overlap of such combined effects influences the roughness characteristics of the grinding wheel, which can be evaluated by means of common roughness parameters (MARINESCU et al., 2007).

Besides the significant influence on the accuracy of the ground components, the microtopography also plays an important role on: a) workpiece profile and roughness; b) energy requirements in grinding; c) down-time for redressing; d) grinding wheel´s life, and e) removal rates during the grinding process (ROWE et al., 2004).

During the grinding process, the material removal process occurs through the sum of particular microscopic events. The local and temporal overlap of such events leads to a macroscopic material removal. As an outcome, the principle of cause-and-effect in grinding can only be defined based on the cutting behavior of the singular abrasive grains. In this case, the most significant parameter consists in the amount of the currently cutting edges engaged during the process. However, the exact assessment of the engagement conditions of the individual cutting edges is not feasible in the grinding process. Due to the random distribution of the cutting edges over the grinding wheel´s circumferential surface, their positions and shapes cannot be precisely determined during the process (MARINESCU et al., 2007).

Figure 6 – Topographic aspects of grinding wheels.

Topographic Aspects of Grinding Wheels	
a) Macrotopography:	b) Microtopography:
• Diameter deviation, Δr	• Flattening and breakage
• Radial runout, E_s	• Loading
• Circularity deviation, O_s	• Drop-out
$\sum$ Waviness, W_s	$\sum$ Roughness

Topography of grinding wheels

→500 µm
→0 µm
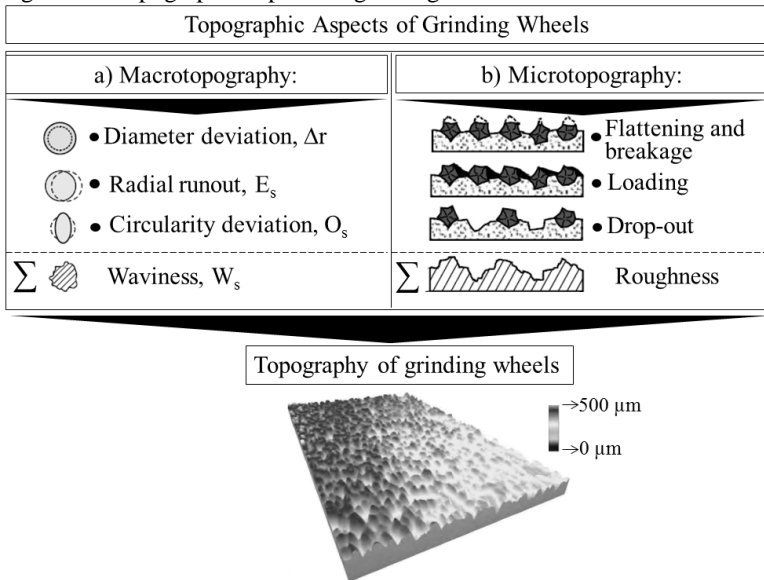
Source: Adapted and based on (DIN EN ISO 25178-2, 2008; DUSCHA; KLOCKE; WEGNER, 2009; MARINESCU et al., 2007).

As a consequence, the position, amount, and shape of the abrasive grains are statistically examined and associated with both the process kinematics and geometry in order to determine the engagement conditions of the abrasive grains. Hence, the results of the grinding process can be correlated with events at the effective area of the grinding contact for specific input values regarding machine, workpiece,

and other process specifications. The main cutting parameters related to the removal process are the engagement angle, the theoretical chip thickness and the chip length. Based on the knowledge of the overall effect between the input values and the output values of the grinding process, the process characteristics can thus be determined and used to process optimization (MARINESCU et al., 2007).

2.5 GRINDING WHEELS CHARACTERIZATION METHODS

Various methods are currently available for determining the topography of grinding wheels. Although the specifications of the grinding wheel, as grain type, grain size, wheel hardness, wheel porosity and bonding are indicated by the manufacturer, such information are often insufficient for an appropriately dimensioning and optimization of the grinding process. Only a suitable knowledge of the topography allows conclusions on the tool capability for the grinding process (DUSCHA; KLOCKE; WEGNER, 2009).

The determination of the grinding wheel´s topography is fundamentally based on three different methods: a) static methods; b) dynamic methods; and c) kinematic simulation methods. The static methods consider all abrasive grains on the surface of the grinding wheel. Such methods do not take into account the kinematics of the grinding process. In the dynamic methods, the measurement of the number of actual abrasive grain engagements is evaluated. The kinematic methods associate the kinematic effects of the grinding process with the statistically evaluated grain distribution for the microkinematic specifications at the individual grain, namely, for the assessment of cutting parameters. Kinematic simulation methods are independent of the grinding conditions (SHAW; KOMANDURI, 1977; VERKERK, 1977 *apud* MARINESCU et al., 2007).

2.5.1 Static Methods

In the static methods, mainly all cutting edges in the cutting area are involved in the topography analysis, thus, there exists no distinction whether a cutting edge of the grinding wheel is actively engaged in the cutting process. Such methods are independent of the grinding conditions (SHAW; KOMANDURI, 1977; VERKERK, 1977 *apud* MARINESCU et al., 2007; KÖNIG, 1989). Figure 7 schematically shows a simplified representation of a cross-section to the rotation axis of a grinding wheel whose circumference is engaged. All grits protruding

from the bond have cutting edges. The area between the cutting edges is named as the cutting space or chip space. Since one grain can certainly have several cutting edges, the distance between the static cutting edges (L_{static}) does not coincide with the average static grain separation ($L_{static,average}$) on the grinding wheel (KLOCKE; KÖNIG, 2005; MARINESCU et al., 2007). Therefore, in place of the distance between the static cutting edges, the number of cutting edges is specified per unit length, namely, the static cutting edge number S_{stat}, or the cutting edge density per surface unit N_{stat}, or even the cutting edge amount per unit volume C_{stat} of the cutting area (DAUDE, 1966; LORTZ, 1975; KAISER, 1977; SHAW; KOMANDURI, 1977 *apud* MARINESCU et al., 2007).

Figure 7 – Static cutting edges.
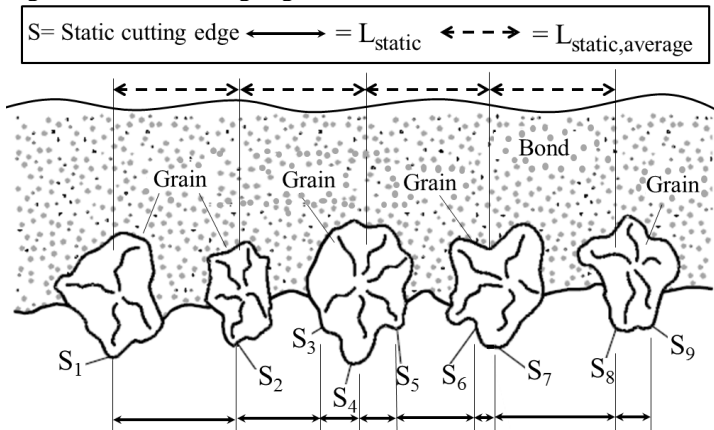
Source: Adapted and based on (KÖNIG, 1989; MARINESCU et al., 2007).

2.5.2 Dynamic Methods

On the contrary to the static methods, the dynamic methods depend on the grinding conditions (MARINESCU et al., 2007). By superimposing the movements of the grinding wheel and the workpiece, the effective cutting edges´ paths in the material can be obtained (KLOCKE; KÖNIG, 2005; KÖNIG, 1989). By considering the grinding process (i.e., process parameters as well as the geometric engagement conditions), information is achieved regarding the areas of the effective surface of the grinding wheel which are actually involved in the process (VERKERK, 1977; GAERTNER, 1982 *apud* MARINESCU et al., 2007). Only part of the cutting edges protruding from the bond (the so-called

kinematic cutting edges), take active part in material removal, Figure 8. The number and density of the kinematic cutting edges (S_{kin} and C_{kin}, respectively) are hence smaller than the number and density of the static cutting edges (S_{stat} and C_{stat}, respectively). The values of S_{kin} and C_{kin} are mainly determined by the geometric and kinematic parameters. Due to the inherent wear of the grinding wheel and the constant changes in the topography of the grinding wheel, the cutting edge density has continually changing values (KÖNIG, 1989; MARINESCU et al., 2007).

Figure 8 – Kinematic cutting edges.
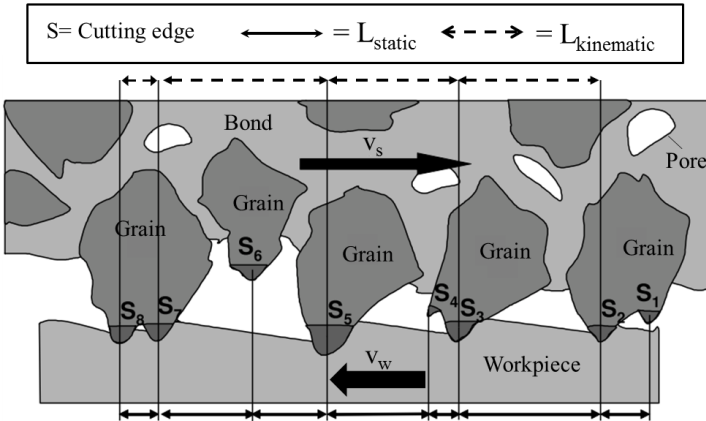
Source: Adapted and based on (KLOCKE; KÖNIG, 2005).

The number of kinematic cutting edges N_{kin} per mm^2 of the grinding wheel´s circumference can be calculated from Equation 2 (KLOCKE; KÖNIG, 2005; SPUR, 1980), where A_N is a proportionality constant, C_1 is the cutting edge density, and d_{eq} is the equivalent grinding wheel diameter. The coefficients α and β are experimental coefficients based on the cutting edge distribution.

$$N_{kin} = A_N . C_1^{\beta} . \left(\frac{v_w}{v_s}\right)^{\alpha} . \left(\frac{a_e}{d_{eq}}\right)^{\alpha/2} \tag{2}$$

Equation 2 shows that N_{kin} increases with both higher infeed velocities (i.e., higher a_e) and v_w, and decreases with higher values of v_s. By knowing the value of N_{kin} the theoretic distance between the kinematic cutting edges can be evaluated, then also allowing the estimation of the statistically average maximum underformed chip

thickness (h_{cu}). At a constant specific material removal rate $Q´_w$, the average number of cutting edges momentarily engaging (N_{mom}) can be estimated (KLOCKE; KÖNIG, 2005; KÖNIG, 1989).

2.5.3 Kinematic Simulation Methods

In the kinematic simulation approach, the kinematics of the grinding process are in addition considered for the determination of the effective cutting area. Based on the kinematically determined cutting edge number, the trajectories of the individual grains are reproduced by considering the grinding process and its process parameters as well as the geometric engagement conditions (LORTZ, 1975; GAERTNER, 1982 *apud* MARINESCU et al., 2007).

2.6 ASSESSMENT OF THE TOPOGRAPHY OF GRINDING WHEELS

Among the distinct existing methods for the characterization of the grinding wheel´s topography (see Section 2.5), some particular measuring techniques have been increasingly applied over time both in industry and academy.

Each measuring technique has its advantages and disadvantages depending on some specific factors as resolution, measuring depth, ease of application, and data analysis and interpretation. With each new technique, further comprehension is gained into the nature of the grinding wheel´s topography. No single approach affords a complete description of the topography of grinding wheels (MALKIN; GUO, 2008). Figure 9 schematically illustrates the main measuring methods and their measuring techniques for characterizing the topography of grinding wheels.

In the static methods, a first possible approach for measuring the grinding wheel´s topography can be carried out by using imprint methods, Figure 9-a. Imprint methods commonly involve replicating or imprinting the grinding wheel´s topography on a second material or structure. Replication is often utilized as an alternative to overcome technical difficulties of making direct measurements on large grinding wheels or of monitoring the tool when it is undesirable to remove and replace the grinding wheel. This often occurs when it is desirable to monitor changes in the topography of the grinding wheel within a redress cycle. A replica can be prepared by using either a setting compound or a soft metal (MALKIN; GUO, 2008; ROWE et al., 2004).

The replication material is poured or pressed onto the area of analysis on the grinding wheel´s surface. After cured, this leads to a solid surface which should be ideally identical with the area of analysis. The replicas can afterwards be measured and observed by employing different measuring procedures by means of stylus, optical, and even microscopy techniques (CAI et al., 2003; ROWE et al., 2004). Based on such measuring techniques, the number of static cutting edges per unit area of the grinding wheel´s surface (N_{stat}) can be estimated (MARINESCU et al., 2007).

Figure 9 – Usual methods for characterizing the topography of grinding wheels.

Methods for characterizing the topography of grinding wheels

	Static Methods
Post-Process	a) Imprint methods
	b) Microscopy methods
	c) Profile tactile methods (2D/3D)

	Dynamic Methods	
In-Process	d) Piezoelectric methods	g) Pneumatic methods
	e) Thermoelectric methods	h) Inductive methods
	f) Laser triangulation methods	
Post-Process	i) Photoelectric methods	
	j) Scratch methods	

	Kinematic Methods
Post-Process	k) Methods for kinematic simulation of the process

Source: Adapted and based on (DUSCHA; KLOCKE; WEGNER, 2009; MARINESCU et al., 2007).

Investigations on a water-based plastic system and on epoxy resin systems have shown that both approaches present the ability to replicate surface structure and have relatively low shrinkage (ROWE et al., 2004). Gel-type materials have also been used for imprinting the grinding wheel´s topography. After a few minutes the gel-type material is hardened and the topography of the grinding wheel is printed on it. By sectional cutting the hardened gel material and afterwards scanning it on a high resolution scanner, the measurement of the grinding wheel´s

topography can be fulfilled (BASERI, 2010). As an alternative to both the plastic-base and resin-base imprints, it is also possible to imprint the surface of the grinding wheel onto mild steel specimens which are kept static. The evaluation of the topography of the grinding wheel is then implemented by measuring the roughness parameters on the ground specimens (MOKBEL; MAKSOUD, 2000).

A second possible approach for measuring the grinding wheel´s topography can be carried out by using microscopy methods, Figure 9-b. These methods are based on the analysis of images extracted from the surface of the grinding wheel in order to initially obtain qualitative information related to the wear process of the grinding wheel (HWANG et al., 2000). Such information can be acquired by means of special techniques as for example optical, stereo-microscopy, or scanning electron microscopy (SEM), (SCHLEICHL, 1982; STUCKENHOLZ, 1988 *apud* MARINESCU et al., 2007). Meanwhile, the microscopy methods can also be used aiming at obtaining quantitative information about the grinding wheel´s topography. For that purpose, the cutting edges or the distinct wear characteristics of the grinding wheel can be statistically evaluated. Measurements are then conducted either directly on the grinding wheel´s surface or indirectly by extracting an imprint of the grinding wheel. As a result, information about the number of static cutting edge per unit surface (N_{stat}) as well as the amount of static cutting edges per unit volume (C_{stat}) can be estimated (LACHANCE; WARKENTIN; BAUER, 2003; MARINESCU et al., 2007).

Yet in the static methods, a third possible approach for characterizing the topography of grinding wheels can be achieved by using a stylus technique, Figure 9-c. This technique consists in horizontally dragging a stylus with a very small tip radius across the surface of the grinding wheel, as usually done in roughness measurements. The vertical movements of the stylus are measured by using a displacement transducer and the measurement results are plotted as 2D records of the grinding wheel´s topography (ROWE et al., 2004). 3D records of the grinding wheel´s topography are also possible to be obtained, by displacing the stylus sideway in small precisely and well-defined distances. Despite the versatility of the stylus measuring approach, some disadvantages also need to be addressed, such as: a) measurement accuracy highly dependent on the size and shape of the stylus´ tip; b) stylus wear during continuous measurements of the grinding wheel; and c) positioning of the grinding wheel on the measuring instruments (ROWE et al., 2004). Based on such measuring technique, it is possible to estimate both the number of static cutting

edges per unit area of the grinding wheel´s surface (N_{stat}) and the number of static cutting edges per unit volume of the grinding wheel´s surface (C_{stat}). The cutting edges are estimated based on the envelope curve of the effective area of the grinding wheel, which is defined by the external cutting edges. With increasing depth of the stylus, more interaction is achieved, thus making it possible to obtain frequency curves of the existing cutting edges (MARINESCU et al., 2007).

In the dynamic methods, the measurement of the grinding wheel´s topography can be evaluated either during the grinding process (i.e., in-process dynamic methods) or after the grinding process (i.e., post-process dynamic methods). Both variations of the dynamic methods aim to estimate the number of kinematic cutting edges per surface area (N_{kin}) on the surface of the grinding wheel which effectively are involved in the cutting process (DUSCHA; KLOCKE; WEGNER, 2009; MARINESCU et al., 2007).

In the in-process dynamic methods, five different measuring approaches are commonly used: piezoelectric methods (Figure 9-d); thermoelectric methods (Figure 9-e); laser triangulation methods (Figure 9-f); pneumatic methods (Figure 9-g); and inductive methods (Figure 9-h). Piezoelectric and thermoelectric methods can be employed for the determination of N_{kin} based on the measurements of force, temperature, and AE of single active cutting edges (DAUDE, 1966; KAISER, 1977 *apud* MARINESCU et al., 2007). The piezoelectric methods (Figure 9-d) are preferably usable for small contact surfaces, since it needs to be guaranteed that at any time no more than one cutting edge is involved in the contact zone.

In the thermoelectric methods (Figure 9-e), a thermocouple wire with a small diameter is insulated by means of a thin layer from the surrounding material within the workpiece. The contact of each active cutting edge damages the insulating layer and originates a thermocouple junction through plastic deformation. This produces the emission of a recognizable thermoelectric voltage signal from which an equivalent temperature can be determined. Hence, the material must have good electrical conductivity and enough ductility (MARINESCU et al., 2007).

In grinding operations a laser triangulation transducer can be used to sense the grinding wheel´s topography at working speed (Figure 9-f). The maximum allowed v_s for detecting the macrotopography is about 300 m/s, whereas for the microtopography v_s must not exceed 20 m/s (TÖNSHOFF; FRIEMUTH; BECKER, 2002). Light emitted from a laser diode is reflected from the grinding wheel´s topography and focused on a receiver diode by means of a lens. The reduced peak roughness R_{pk}

and the reduced valley roughness R_{vk} can be identified from the measured signal, thus allowing the topography of the grinding wheel to be evaluated (BYRNE et al., 1995). Generally, such measuring approach is influenced by dirt and chips, and appropriate cautions have to be taken. As a consequence of such limitation, this measuring approach has been slow to find acceptance in industry (DORNFELD; LEE, 2008).

The pneumatic methods (Figure 9-g) are basically used for determining the macrotopography of grinding wheels. In principle, such measuring approach is not able to detect the microtopography of grinding wheels due to the nozzle diameter of about 1 mm or higher that is usually utilized. Systems with compressed air supply or those without air supply have to be distinguished. The latter are characterized by the airflow measurement around the rotating grinding wheel. The achieved results with this measuring approach show a dependence of the airflow on: a) the distance between the transducer and the surface of the grinding wheel; b) the cutting speed v_s; and c) the topography of the grinding wheel, to a small amount. Systems with compressed air supply are based on the nozzle-bounce plate principle, being the grinding wheel the bounce plate. These systems are suitable for measuring distance changes and thus allow measuring radial wear with a resolution in the range of 0,2 μm. These aspects in particular, in conjunction with the reasonable costs and the straightforward set-up are the main reasons why pneumatic transducers have found acceptance in industry (MARINESCU et al., 2007; TÖNSHOFF; FRIEMUTH; BECKER, 2002).

The grinding wheel loading with conductive metallic particles during the process is associated with the microtopography of a grinding wheel and can be identified by employing the inductive methods (Figure 9-h). In general, the transducer consists of a high permeability core and a winding and is usually positioned a short distance from the surface of the grinding wheel. The metallic particles generate an impedance change which can be measured and further processed to assess the condition of the grinding wheel loading. Due to the fact that such microtopographic characteristic (loading) is only detected when grinding metallic material, the inductive methods did not reach so far a wide application in industrial practice (TÖNSHOFF; FRIEMUTH; BECKER, 2002).

In the scope of the dynamic post-process methods, a possible attempt for determining the topography of the grinding wheel can be achieved by using a photoelectric approach, Figure 9-i. Based on the scattered light principle, the light reflected by the cutting area is collected by means of a radiator detector. Therefore, the distribution of the scattered light as well as the duration and amount of light impulses

(in the direction of the regular direct reflection) are evaluated (WERNER, 1994 *apud* MARINESCU et al., 2007; OLIVEIRA, 1992 *apud* GOMES, 2001). This measuring approach allows estimating the number of kinematic cutting edges per surface area (N_{kin}) of the grinding wheel (MARINESCU et al., 2007).

Scratch methods (Figure 9-j) are based on producing isolated scratch marks by grinding a relatively smooth and soft workpiece. Aiming at obtaining isolated scratches (rather than a ground surface consisting of overlapping scratches), the workpiece is moved reasonably quickly past a slowly rotating grinding wheel (MALKIN; GUO, 2008). The roughness profile of the ground workpiece derives from the N_{kin} overlapping profiles in the removal process. Such measuring technique is suitable for a comparative evaluation of the grinding wheel´s topography. However, any statements concerning the amount and shape of the cutting edges are not possible (LORTZ, 1975; WERNER, 1994 *apud* MARINESCU et al., 2007).

The topography of grinding wheels can also be assessed by using kinematic simulation methods, Figure 9-k. In these methods, a kinematic simulation of the grinding process is carried out, thus aiming at the estimation of N_{kin}. The kinematic simulation of the grinding process is based on numeric models which simplify diverse aspects related to the grinding process (MARINESCU et al., 2007).

2.7 SIGNAL PROCESSING AND ANALYSIS

Signal processing refers to the utilized procedures on measured data to reveal the contained information in the measurements from a specific physical phenomenon. These procedures basically depend on several transformations which are mathematically based and that generally are implemented by employing digital techniques (SHIN; HAMMOND, 2008). The aim of signal processing is to extract information from a signal related to a process or physical phenomena, Figure 10-a. This commonly involves some basic requirements which follow a logic progress, as summarized in Figure 10.

The first step that one must consider in order to obtain reliable information from the investigated process is the adequately choice of transducers and their correlated instrumentation, Figure 10-b. The selected transducers should be able to detect the variations of the process characteristics (e.g., force, power, acoustic emission, vibration, temperature, etc.) and convert them into appropriate signals (KÖNIG; MEYEN, 1990; SHIN; HAMMOND, 2008).

Thereafter, the following step is related to the conditioning of the transducers´ analog output signals, aiming at reducing mechanical and electrical noises which are commonly present in the original signal, Figure 10-c. For that, specific signal conditioning techniques are employed (i.e., signal amplification, band-pass, signal filtering, signal rectifying, low-pass filtering) for the sake of preparing the analog signals for digitization. An important issue during signal conditioning consists in band limiting the acquired analog signal before sampling it (KÖNIG; MEYEN, 1990; SHIN; HAMMOND, 2008).

After conditioning the analog signal, it is possible to sample it in order to convert the analog signal into the digital domain, Figure 10-d. This is often carried out by means of an Analog to Digital Converter (ADC). The signal is sampled by the ADC in discrete time intervals based on a specific sampling rate which is defined by the Nyquist´s theorem in order to avoid aliasing errors (BENDAT; PIERSOL, 1971; GERGES, 2006).

Figure 10 – Logic progress and main requirements for signal processing.

a) Process

b) Transducers/Instrumentation

c) Signal Conditioning

d) Analog to Digital Conversion

e) Signal Analysis (time/frequency domain)

f) Feature Extraction
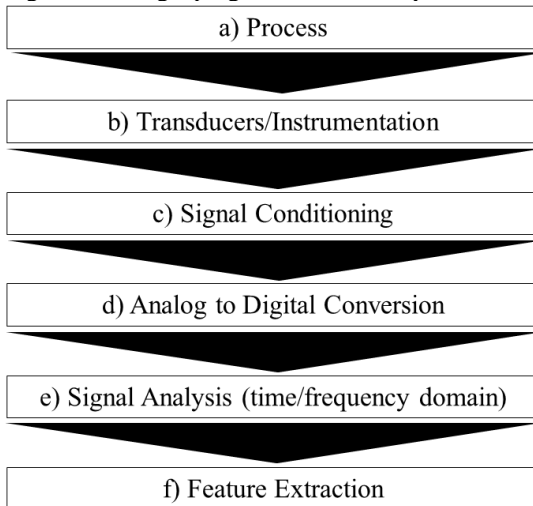
Source: Adapted and based on (XIAOQI; HAO; WILDERMUTH, 2001).

Based on the digitized signal, appropriate signal processing techniques can be employed aiming at extracting different types of information from the signal, Figure 10-e. The diverse possibilities to analyze the signals derived from physical events are usually divided into two groups of techniques: a) time domain analysis, and b) frequency

domain analysis. Both distinct ways of analyzing the signals are interchangeable, that is, there is no information lost in changing from one domain to the other. The benefit of analyzing signals under different domains is that of change in perspective. For example, by altering the perspective from the time domain to the frequency domain, the solution to complex problems can frequently become quite clear. Each of both signal domain analyses presents distinct techniques whose efficiency depends strongly on the particular characteristics of the problem and the system being investigated (PACKARD, 1994; SHIN; HAMMOND, 2008). The correct analysis of the digitized signals allows extracting features from the digitized signals which in turn lead to the process characterization, Figure 10-f.

In the scope of the grinding process, signal processing techniques have been employed on the acquired signals of the process (mainly the AE, force, temperature, and power), to obtain a better knowledge of the process and to solve specific problems. Table 1 briefly summarizes several research works which have been employing signal processing techniques in grinding in order to solve specific problems on both academy and industry.

As shown in the Table 1, the AE, force (F), power (P), vibration (V), temperature (T), and the grinding wheel wear (W) are among the main grinding process characteristics which have been investigated in such research works. The signal processing and analysis techniques which have been based on the acquired signals, are used either directly (aiming at extracting useful information from the grinding process) or combined with computational intelligence (CI) techniques. The combined use of both signal processing techniques and CI techniques allows solving particular problems as detached in Table 1. Some of the most commonly used CI techniques in grinding are: Neural Networks (NN), Fuzzy Logic (FL), Genetic Algorithms (GA), and Ant Colony Optimization (ACO).

Table 1 – Signal processing and analysis techniques employed in grinding.

References	Charac.	Signal Processing	CI	Results/Detection
GOVINDHASAMY et al., 2005	AE, P	RMS, FFT	NN	Modelling, process control, chatter and burn detection
SOUZA, 2001	AE	RAW, RMS, FFT	no	Tool wear
SCHÜHLI, 2007	AE, P	RMS	no	Contact recognition, tool run out
CHEN; LIMCHIMCHOL, 2006	F	Short time Fourier Transform	no	Tool wear and chatter
HASSUI et al., 1998	AE, V	FFT, RMS	no	Prediction of tool life
BRINKSMEIER; HEINZEL; MEYER, 2005	AE, F, T	RMS	no	Ground surface quality control
AGUIAR et al., 2006	AE	RMS, Kurtosis, Skew, Mean value, dispersion, autocorrelation	no	Prediction of tool burn
REHSTEINER; KUSTER; HUNDT, 1997	AE, F	FFT	no	Contact recognition
TAYLOR et al., 1995	AE	RMS, Spectral Density, Filtering	no	Gap elimination
OLIVEIRA; DORNFELD, 2001	AE	RMS	no	Tool mapping
VARGHESE et al., 2000	AE, F	RMS, FFT	no	Macrogeometry errors, contact recognition
PATHARE; GAO; VARGHESE, 1998	AE, F	RMS, FFT	no	Tool wear, circularity errors
AKBARI et al., 1996	AE	Statistical parameters, FFT	no	Ground surface, quality control
QI; ROWE; MILLS, 1997	AE	RMS	no	Contact recognition
LIAO, 2010	AE	Wavelet, Autoregressive	ACO	Tool optimization
LIAO, 2007	AE	Wavelet	GA	Tool monitoring
LEE et al., 2005	AE	RMS	no	Tool mapping
LIU;CHEN;GINDY, 2005	AE	Wavelet	FL	Pattern recognition
JU;KIM;HONG, 2001	W	Statistical techniques	no	Tool circularity and wear measurements
KWAK; HA, 2003	AE	RMS and FFT analysis	NN	Chatter control
GOMES, 2001	AE	RMS	no	Tool wear identification

Note 1: AE= Acoustic Emission; F= Force; P= Power; T= Temperature; V= Vibration; W= Wear
Note 2: CI= Computational Intelligence; FFT= Fast Fourier Transform; NN= Neural Network; RMS= Root Mean Square
Source: (Developed by the author).

2.7.1 Technical Properties of Piezoelectric Transducers

The effective choice of transducers relies on the knowledge of their basic technical properties which can be divided into two principal groups: a) Static properties, and b) Dynamic properties. The static properties of piezoelectric transducers are related to the response of transducers independently of the measurand variations over time. On the other hand, the dynamic properties refer to the characteristics which are associated with the response of transducers to variations of the measurand over time (AMBROSIUS; FELLOWS; BRICKMANN, 2009; FIGLIOLA; BEASLEY, 2000; GAUTSCHI, 2001; KISTLER, 2010). This section briefly describes the main technical properties of piezoelectric transducers.

2.7.1.1 Static properties of piezoelectric transducers

The main static properties of piezoelectric transducers are: a) properties related to the measurand (e.g., range, span, and overload); b) properties concerning the correlation between measurand and the output (e.g., threshold, sensitivity, hysteresis, and linearity); c) properties connected with the effects of temperature on the correlation between measurand and output (e.g., operating temperature range, and room conditions). In addition, further important static properties of transducers are: d) drift, e) stability, and f) repeatability. These properties are described in the upcoming sections.

2.7.1.1.1 Range, span and overload

The Range, Span, and Overload are measurand-related properties. The property "Range" of a transducer refers to the values of the measurand (i.e., measured physical quantity, state or characteristic) over which the transducer is intended to measure. The values of the measurand are defined by its upper and lower limits. The algebraic difference amid the upper and lower limits of the "Range" is labeled as the "Span" of the transducer. In addition, the property "Overload" characterizes the maximum measurand magnitude which is allowed to be applied to the transducer, without producing changes in its performance beyond the specified tolerances (GAUTSCHI, 2001; KISTLER, 2010).

2.7.1.1.2 Threshold, sensitivity, hysteresis, and linearity

Threshold, sensitivity, hysteresis and linearity are static properties of transducers associated with the relationship between the measurand and the transducer´s output. The property "threshold" is defined as being the smallest change in the measurand which yields a measurable variation in the signal of the transducer. "Sensitivity" refers to the change in the indicated output of the transducer with a given change in the value of the measurand. The "hysteresis" of a transducer denotes the maximum difference in its output (at any measurand value inside the analyzed range), when the value is approached first with increasing and then with decreasing measurand. The closeness of a calibration curve to a definite straight line defines the property "Linearity". It is expressed as the maximum deviance of any calibration point from a specified straight line and expressed in percentage of the FSO (Full Scale Output), (FIGLIOLA; BEASLEY, 2000; GAUTSCHI, 2001; KISTLER, 2010).

2.7.1.1.3 Operating temperature range, room conditions

The range of extreme ambient temperatures, within which the transducer is designed to operate, is defined as the property "Operating temperature range". Within this range, all tolerances specified for temperature error are applicable. The ambient environmental conditions under which piezoelectric transducers must usually operate refer to the property "room conditions". Such conditions are normally stablished for the temperature of 25 ± 10 °C, and the relative humidity of 90 % or less (GAUTSCHI, 2001; KISTLER, 2010).

2.7.1.1.4 Drift, stability and repeatability

"Drift" is considered a spurious trend in the output signal of piezoelectric transducers, which is independent of the measurand as a function of time. Such spurious trend generates unwanted changes in the offset (or d.c level) of the signal, often represented by the segmented average of the signal (e.g., $\bar{x}_1$ and $\bar{x}_2$, Figure 11). Therefore, "drift" characterizes the existence of a varying mean, non-stationary output signal (GAUTSCHI, 2001; KISTLER, 2010; SHIN; HAMMOND, 2008).

Figure 11 – Drifting.
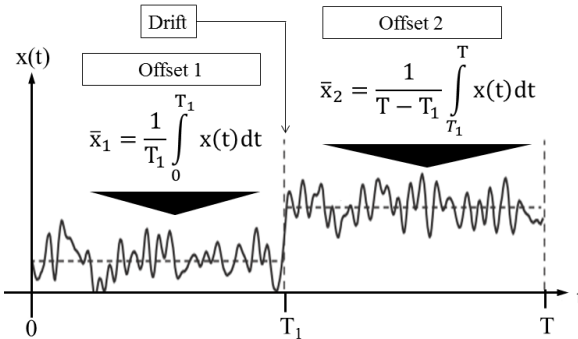
Source: Adapted and based on (SHIN; HAMMOND, 2008).

The characteristic "stability" of a piezoelectric transducer defines its capability to maintain performance for a relatively long period of time. It is commonly expressed as a percentage value of the full scale output (FSO) for a period of time. The "stability" depends greatly on the type of piezoelectric material used (e.g., quartz or ceramic) and also on the design and the employed materials for the construction of the transducer (GAUTSCHI, 2001).

The capability of a piezoelectric transducer to replicate readings (under the same conditions, and in the same direction) when an identical measurand value is successively applied to it, is inferred by the property "repeatability". Piezoelectric transducers usually exhibit extremely good repeatability, especially when employing quartz materials (GAUTSCHI, 2001).

2.7.1.2 Dynamic properties of piezoelectric transducers

The principal dynamic properties of piezoelectric transducers are: a) frequency response, and b) natural frequency. The "frequency response" defines the change with frequency of the output/measurand amplitude ratio (and their related phase difference), by applying a sinusoidal varying measurand to the transducer within a specified range of measurand frequencies. It is typically specified as a ± percentage value or ± dB (in Hz) and must be sufficiently wide to comprise all the frequencies which occur in the considered measurand. For piezoelectric transducers, the lower limit of the "frequency response" is always determined by the electronic circuit which is utilized to process the transducer´s output. The upper limit is normally defined by the

transducer, unless an electronic circuit with a lower upper frequency limit is used (GAUTSCHI, 2001; KISTLER, 2010).

The property "natural frequency" represents the frequency of not forced (free) oscillations of the entire transducer. In a practical sense, usually the lower natural frequency of the entire mounting structure controls the frequency behaviour (KISTLER, 2010). Piezoelectric transducers intrinsically possess very high natural frequencies, hence, the assessment of their natural frequencies it is very difficult and sometimes even impossible (GAUTSCHI, 2001).

2.7.2 Transducers for Measuring Process Characteristics in Grinding

In industrial and research activities, the most common process characteristics of the grinding process that have been often evaluated are: grinding cutting force, grinding AE and the grinding power. For evaluating such process characteristics, the acquisition and installation of specific transducers are normally required, Figure 12.

Figure 12 – Possible alternatives for mounting force, AE, and power transducers.
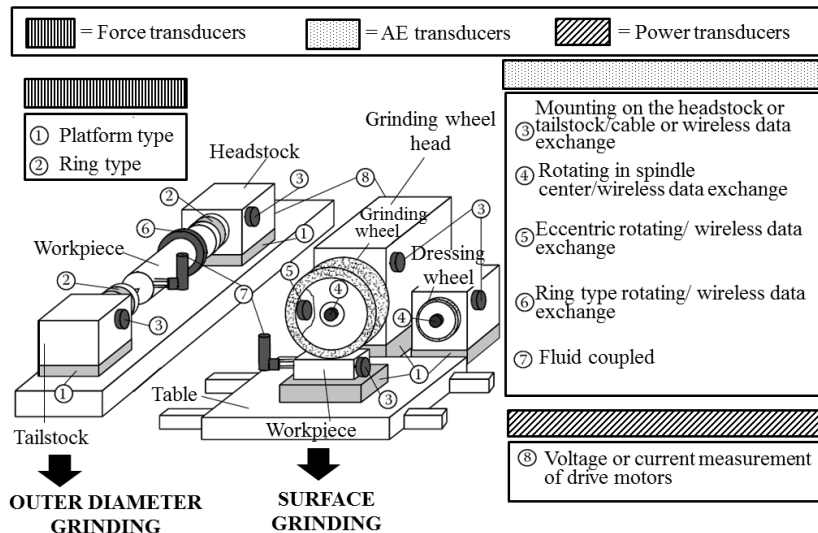
Source: Adapted and based on (KARPUSCHEWSKI, 2001; MARINESCU et al., 2007).

2.7.2.1 Transducers for measuring power/current in grinding

Transducers for measuring effective power or current of main spindle or feed drives consist in a simple alternative with regard to technical terms and are also reasonably easy to retrofit. Modern NC grinding machines present feed drives in which either current or power can be properly read and evaluated (BYRNE et al., 1995). In grinding, power monitoring is a widespread method due to its easy installation (without influencing the working space of the grinding machine) and the relatively low costs (MARINESCU et al., 2007). Such monitoring method is commonly used in grinding to avoid thermal damage of the workpiece. Nevertheless, this approach has some drawbacks. While measuring the current or power of the feed drives some problems may occur due to the friction component in the machine guideways which is found in the measuring signal. This component is often considerably higher than the signal components which are of significance to the grinding process and might vary intensely according to both the traversing rate and the lubrication state (BYRNE et al., 1995).

Owing to the inert masses, the output signal presents a kind of low-pass filter behaviour. Hence, both burst and brief signals are not detected in real time and the power monitoring system reacts only after the measured signal achieves its maximum limits. Measurements of the main spindle power regularly fail to yield proper outcomes if the cutting process consumes just a fraction of the measured power. Despite these limitations, such measurements can be used to detect collision, tool wear and tool breakage if sufficiently large cross-sectional cutting areas are employed (BYRNE et al., 1995).

2.7.2.2 Transducers for measuring force in grinding

Force measurements essentially rely on the evaluation of a displacement which takes place due to the limited stiffness of a particular system. The measurement of a displacement can be carried out by several distinct transducers, as for example, strain gauges. These transducers have been used since the early fifties primarily to analyzing forces in surface grinding (TÖNSHOFF; FRIEMUTH; BECKER, 2002).

Even though such measurements performed well to accomplishing significant data in grinding, their most important drawbacks consist in the substantial drop of the total system´s stiffness. The strain gauge must be adapted on the system components which are directly subjected to the force load. With the introduction of

piezoelectric quartz force transducers, an adequate solution has been achieved (TÖNSHOFF; FRIEMUTH; BECKER, 2002). The piezoelectric quartz presents sufficient stiffness and can therefore be mounted directly into the flux of force. Due to the anisotropic behavior (i.e., the material properties change depending on the direction in which the material is cut) of the piezoelectric quartz materials, it is possible to arrange them in order to form a three-component force measuring transducer (TÖNSHOFF; FRIEMUTH; BECKER, 2002). The piezo-based systems need additional charge amplifiers in order to convert the charges derived from the piezoelectric effect into a voltage for further analysis. Different force measuring platforms are ready for use in a variety of types and sizes and are well protected against the environmental conditions commonly found in industrial production (TÖNSHOFF; FRIEMUTH; BECKER, 2002).

2.7.2.3 Transducers for measuring acoustic emission (AE) in grinding

Grinding processes are characterized by the simultaneous and randomly distributed contact of several diverse cutting edges with the workpiece. During grinding, each single contact between the cutting edges and the workpiece causes stress waves which spread through the workpiece, the grinding wheel, and the machine tool´s structure. These waves (also known as acoustic emission or AE, see Section 2.3) are commonly exposed to various noise sources from the environment and inside the machine tool like, for example, motor, bearings, lubricant, etc. In order to diminish the influence of the noise sources on the AE signal and also to achieve a good transducer output, the mounting position of the AE transducer and the transmission path of the AE signal are essential issues in grinding monitoring (TÖNSHOFF; FRIEMUTH; BECKER, 2002).

This can customarily be accomplished only through field tests, by experimentally seeking the clearest and most significant AE signal. AE transducers are usually of the piezoelectric type and also similar to the acceleration transducers, except that they do not require a seismic mass, but rather a particular damping material directly applied to the sensing element, Figure 13 (GAUTSCHI, 2001).

Figure 13 – AE transducer.
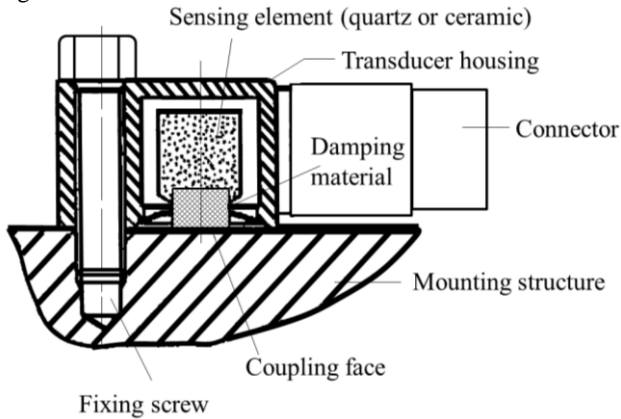
Source: Adapted and based on (GAUTSCHI, 2001).

AE piezoelectric transducers are very often employed for monitoring the grinding process. When submitted to a periodically load (force), the piezoelectric material of such AE transducers (usually quartz or a piezoelectric ceramic) converts the acceleration produced on the sensing element into proportional electrical charge (KÖNIG; MEYEN, 1990).

For in-process monitoring in grinding, AE transducers must fulfill some requirements and characteristics, as for example: a) wide-ranging and flat frequency response; b) high sensitivity; c) stable coupling to the mounting face; d) intrinsic high-pass characteristic (insensitive to low-frequency noise); e) insensitive to electrical and magnetic fields; f) low mass and reduced dimensions; g) rugged (at least protection class IP65, IP67); and allow easy mounting (GAUTSCHI, 2001; KISTLER, 2010).

The monitoring of the grinding process based on the AE technology can find different applications, as for example, the detection of grinding wheel wear, grinding wheel loading, chatter analysis, the detection of grinding burn and cracks, and gap elimination (WEBSTER; DONG; LINDSAY, 1996). Additionally, it is also possible to detect collision (KLUFT, 1989) and to monitor the dressing process (LEME, 1999).

2.7.3 Analog to Digital Conversion (Sampling, Aliasing)

The output signals derived from the piezoelectric transducers mentioned in the previous sections are analog signals, i.e., signals whose

values are continuous and are defined at each and every single instant of time (NATIONAL, 1997). In order to analyze the analog signal by means of digital signal processing techniques, one must firstly convert the analog signal into its digital representation. This is normally implemented by using an analog-to-digital (A/D) converter, which is usually an integral part of the data acquisition boards (NATIONAL, 1997; SHIN; HAMMOND, 2008).

An A/D is a device that receives an analog time signal as an input and yields a sequence of numbers (i.e., digital signal) as an output that consists in sampled values of the input. Such process is normally called as sampling (SHIN; HAMMOND, 2008).

The sampling rate (f_s) defines how frequently an analog-to-digital conversation occurs. In practice, high values of f_s lead to more acquired points in a specified time interval and permit to better represent the original signal. On the other hand, small values of f_s may conduct to a poor or insufficient representation of the original analog signal. The effect of undersampling an analog signal conducts to the misrepresentation of the original signal, Figure 14 (NATIONAL, 1997; PACKARD, 1994; SHIN; HAMMOND, 2008).

Figure 14 – Insufficient signal representation due to undersampling.
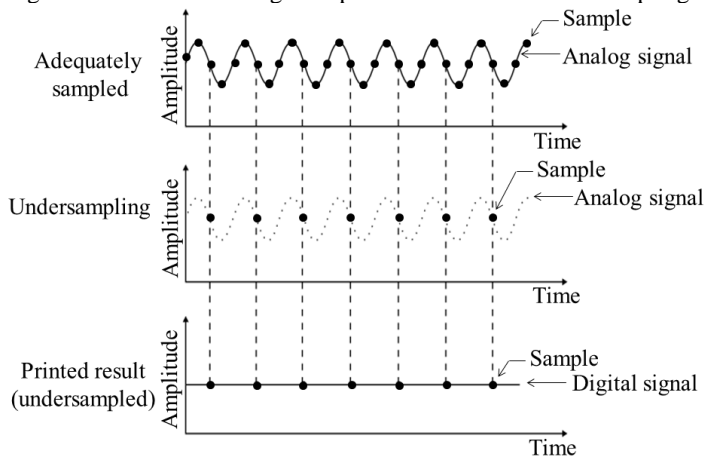
Source: Adapted and based on (NATIONAL, 1997; PACKARD, 1994; SHIN; HAMMOND, 2008).

In the frequency domain, undersampled signals are often subjected to aliasing errors, also known as spectral distortions. To avoid aliasing one must sample at f_s greater than at least twice the maximum

frequency content in the signal (f_{MAX}) which is being acquired, Equation 3. The maximum frequency that can be represented accurately without aliasing (for a specified value of f_s) is known as the Nyquist frequency (BENDAT; PIERSOL, 1971; GERGES, 2006; NATIONAL, 1997; PACKARD, 1994; SHIN; HAMMOND, 2008).

$$f_s \geq 2 \; x \; f_{MAX} \tag{3}$$

2.7.3.1 Analog low-pass filters (anti-aliasing filters)

The problems related to the aliasing effect cannot be avoided by simply choosing indefinitely high values of f_s. In addition, high f_s values over long periods of time lead to further problems, as for example, not enough computing memory and insufficient hard disk space to save the acquired data (NATIONAL, 1997). In practice, the most suitable alternative to overcome the aliasing effect consists in filtering the analog signal, before sampling it, by using an analog low-pass filter, also known as anti-aliasing filter. This affords a band-limited analog signal with defined frequency content (NATIONAL, 1997; PACKARD, 1994; SHIN; HAMMOND, 2008). Anti-aliasing filters are characterized by their frequency response functions $|H(f)|$, Figure 15.

Figure 15 – Low-pass analog filters (anti-aliasing filters).
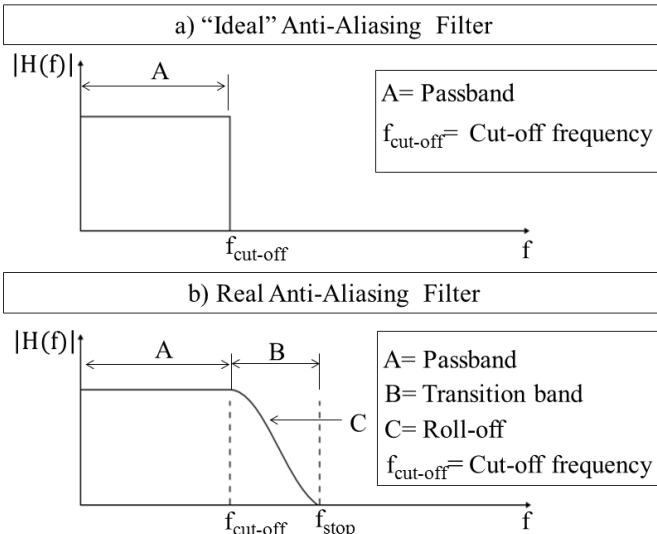
Source: Adapted and based on (PACKARD, 1994; SHIN; HAMMOND, 2008).

An ideal anti-aliasing filter passes all the desired input frequencies below $f_{cut-off}$ (cut-off frequency) and cuts off all the undesired frequencies above $f_{cut-off}$, Figure 15-a. However, such a filter is not realizable in a physical sense. In practice, an anti-aliasing filter passes all the frequencies bellow $f_{cut-off}$ and cuts off all the frequencies above f_{stop}. The region between $f_{cut-off}$ and f_{stop} is labelled as transition band, which is characterized by an attenuation of the input frequencies, Figure 15-b. Anti-aliasing filters must present a flat passband and also sharp cut-off characteristics. The Chebychev and Butterworth anti-aliasing filters are among the most commonly used anti-aliasing filters, (NATIONAL, 1997; PACKARD, 1994; SHIN; HAMMOND, 2008).

2.7.4 Stochastic Process

A stochastic process is characterized as being a time-dependent random variable (X). In other words, the stochastic process consists of a random function over time (t) which is usually labeled as X(t), Figure 16. Classical examples of such class of signals are measured signals which are time dependent, as for example, force, vibration, or AE signals recorded during the grinding process. Vibration signals measured on a vehicle chassis can also be considered as an example of stochastic process (PACKARD, 1994; SHIN; HAMMOND, 2008).

Due to the random character of a stochastic process, it is normally required to replicate the process (or experiments), that is, producing additional realizations of a single stochastic process. A set of such realizations is called an ensemble (whether finite or infinite) and is commonly represented as {X(t)} (SHIN; HAMMOND, 2008).

Figure 16 – Ensemble of infinite stochastic processes.
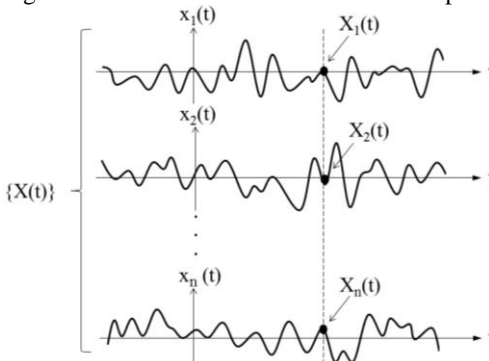
Source: Adapted and based on (SHIN; HAMMOND, 2008).

2.7.5 Stationarity

Stochastic processes are considered stationary when their statistical properties do not change over time (SHIN; HAMMOND, 2008; SMITH, 2003). In general, all practical processes are in fact non-stationary, therefore the assumption of stationarity is considered as only an approximation. Nevertheless, in several practical situations, this assumption provides a sufficiently close estimate (SHIN; HAMMOND, 2008). The assumption of stationarity is very important, especially when an ensemble (a set of stochastic signals) is not at disposal due to a lack of resources regarding available time and costs. Therefore, in many practical circumstances one has to deal with only a single record of data rather than a set of records. In this case, it is not possible to implement the average across the ensemble, but only average along time, that is, one performs a time average instead of an ensemble average. Hence, the assumption of stationarity is a necessary condition in order to allow the time average to be meaningful. The problem of determining whether a practical process is stationary or not is frequently difficult and depends on previous information, although observations and statistical investigations on time histories can be helpful (PRIESTLEY, 1981; BENDAT; PIERSOL, 2000 *apud* SHIN; HAMMOND, 2008). Figure 17 shows typical records of non-stationary and stationary data.

Figure 17 – Typical records of non-stationary and stationary data.
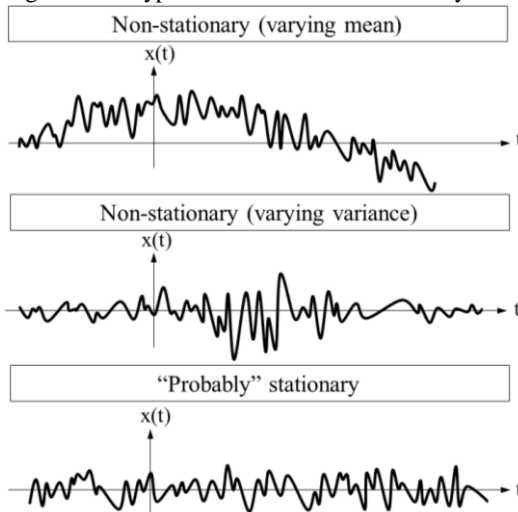
Source: Adapted and based on (SHIN; HAMMOND, 2008; SMITH, 2003).

For a stochastic signal x(t) presenting a finite length T, if x(t) is digitized using samples every Δ seconds, so that $T = N\Delta$, the estimate of the mean value $\bar{x}$ is as follows, Equation 4, (SHIN; HAMMOND, 2008).

$$\bar{x} = \frac{1}{N} \sum_{n=0}^{N-1} x(n\Delta) \tag{4}$$

Similarly, the estimate of the time-average mean square value is defined by Equation 5 (SHIN; HAMMOND, 2008).

$$\hat{\psi}_x^2 = \frac{1}{N} \sum_{n=0}^{N-1} x^2(n\Delta) \tag{5}$$

The RMS value is computed based on Equation 5, by evaluating the square root of it. Additionally, the variance of the digitized signal is estimated by Equation 6, where $\hat{\sigma}_x$ is the estimate of the standard deviation (SHIN; HAMMOND, 2008).

$$\hat{\sigma}_x^2 = \frac{1}{N-1} \sum_{n=0}^{N-1} (x(n\Delta) - \bar{x})^2 \tag{6}$$

In the frequency domain, stationary stochastic processes can be analyzed by using the Power Spectral Density function (PSD). The PSD function can be obtained by evaluating the Fourier Transform of the Autocorrelation Function, as generally presented in Equation 7 (SHIN; HAMMOND, 2008).

$$S_{xx}(f) = \int_{-\infty}^{+\infty} R_{xx}(\tau) e^{-j2\pi f\tau} d\tau \tag{7}$$

Where $S_{xx}(f)$ is the PSD function and the $R_{xx}(\tau)$ is the Autocorrelation function. The PSD function denotes the power of the signal in each of its frequency components. In other words, it represents a measure of the decomposition of the energy of the process over the frequency domain. It can be calculated by squaring the magnitude of the Fourier transform (DFT or FFT) of the signal (NATIONAL, 1997). Its unit is expressed as (amplitude)^2/Hz (SHIN; HAMMOND, 2008).

2.8 SELF-ORGANIZING MAPS NEURAL NETWORKS (SOM-NNs)

Self-Organizing Maps Neural Networks (SOM-NNs), also known as SOFM (Self-Organizing Feature Maps) have been developed in the eighties by Tuevo Kohonen, and are classified as competitive neural networks. In contrast to other existing models of neural networks, SOM-NNs present strong neurophysiologic inspiration, being thus based on the topological map of the cortex of developed animals, where specific areas feature specific functions (e.g., talk, vision, motion control, tactile sense, etc.) (BRAGA; CARVALHO; LUDERMIR, 2000).

The structures of the SOM-NNs normally consist of two different neuron layers, Figure 18. In the first layer (input layer) the neurons are connected to the input data vector (input pattern). Each neuron in this layer is also connected to all the other neurons in the second layer (competitive layer). The second layer is a bi-dimensional grid, where each neuron is connected to all neurons in its neighborhood. This layer can present distinct geometric forms, being the rectangular form the most commonly found (ROISENBERG, 2011). When an input pattern "p" is presented to the SOM-NN, the NN searches for the neuron, whose weigh vector is the most similar to the input pattern. The similarity between the input pattern and the analyzed neuron can be defined by using different metrics, being the Euclidian distance one of the most often used (BRAGA; CARVALHO; LUDERMIR, 2000; MEHROTRA; MOHAN; RANKA, 1996; ROISENBERG, 2011).

Figure 18 – Structure of Self-Organizing Maps Neural Networks (SOM-NNs).
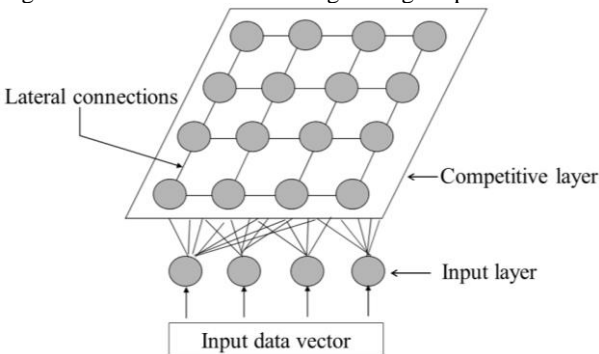
Source: Adapted and based on (BRAGA; CARVALHO; LUDERMIR, 2000).

The neuron presenting the higher similarity to the input pattern receives an auto-excite signal (positive re-alimentation). Such neuron is

often called the winner neuron. During the training process of a SOM-NN, the positive re-alimentation reaches not only the winner neuron, but also its neighbor neurons which lie in a finite distance. That means the winner neuron as well as its neighbor neurons "learn" the input pattern. Such learning feature of SOM-NNs differentiates this type of NN from the other competitive NNs, in which just the winner neuron "learns" the presented input pattern (winner-take-all). The learning process of the SOM-NNs is not supervised, that is, it is carried out without the influence of a specialist (BRAGA; CARVALHO; LUDERMIR, 2000; MEHROTRA; MOHAN; RANKA, 1996; ROISENBERG, 2011).

After the training stage, the SOM-NN allows clustering the input pattern, thus enabling data classification. Sometimes, it is also required the use of an additional type of supervised NN, in order to extract useful information (BRAGA; CARVALHO; LUDERMIR, 2000). The great advantage of using SOM-NNs consists in the fact that such NNs permit representing a multi-dimensional data input into a 2D surface. This allows a better understanding and visualization of the originally multi-dimensional input data. Such dimensional simplification also contributes to verifying important data correlation that otherwise could not be directly observed. Figure 19 shows the possibility of clustering originally multi-dimensional data (e.g., 3D dimension) by using a SOM-NN.

Figure 19 – Data clusterization by using Self-Organizing Maps Neural Networks (SOM-NNs).
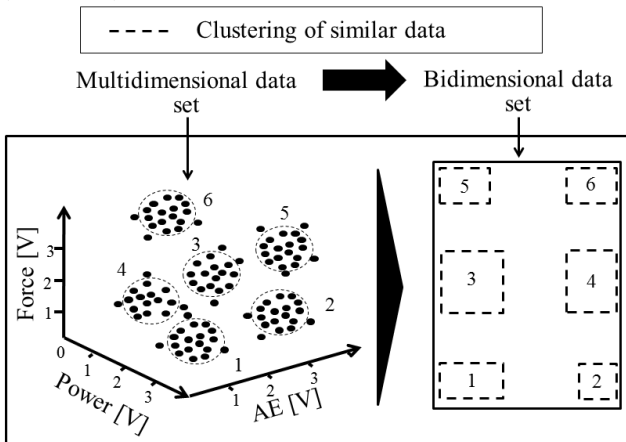
Source: Adapted and based on (BRAGA; CARVALHO; LUDERMIR, 2000; ROISENBERG, 2011).

3 PROBLEM DESCRIPTION AND MOTIVATION

In recent years the grinding process has experienced significant changes. One of the most important developments has been the tendency towards cost savings through a better knowledge of the process while still improving product quality and reduced production time.

In the conventional grinding process the machine operator observes the results on the ground workpiece and then changes the input parameters in order to achieve the desired characteristics. On the other hand, the increasing use of NC machines and the process automation have led to less interference of the machine operator during the grinding process. In this case, the operator usually does not have to change the process, and the changes on the results are identified as a post-process activity by means of the metrology process or by the engineering process. It is necessary to inform the engineering process about the need to change the process. These changes can take a considerably amount of time, and thus leading to the production standstill. Therefore, in order to afford more efficiency to the grinding process, it is necessary to understand and correctly monitor its disturbing factors.

In grinding, one of the most common sources of process disturbance consists of the inherent variation of the grinding wheel´s topography during the process. In the case of fused aluminum oxide grinding wheels, the intrinsic characteristics involving the manufacturing process of these tools (i.e, melting, cooling, crushing and sieving) lead to variations in the grinding wheels´ properties. Hence, the main properties concerning the grinding wheel (e.g., grain size, grain concentration, grinding wheel porosity, grinding wheel hardness, etc.) can only be represented as average values, which also considerably change in the course of the process. The random grain distribution over the topography of the fused aluminum oxide grinding wheels represents a further challenge for predicting the in-process behavior of these tools and to the process control.

Due to the complex structure of the fused aluminum oxide grinding wheels, it is not conceivable to make an overall correlation between the grinding wheel´s specifications (as delivered by the manufacturer of the grinding wheel) and its in-process behavior. This prevents the implementation of databases for the selection of grinding wheels for specific workpiece materials and for machining tasks. In addition, small variations in the topography of grinding wheels often have significant influences on the grinding process and on the grinding results.

Among the diverse existing methods for determining the topography of grinding wheels, three basic methods are currently used: a) static methods, b) dynamic methods, and c) kinematic methods, (BRUECHER, 1996 *apud* KÖNIG, 1989; MARINESCU et al., 2007). A summarized revision of such methods as well as their major features have been presented in Chapter 2. Fundamental concepts in signal processing techniques which are essential for extracting significant information from the acquired signals have also been described.

All the approaches mentioned for characterizing the topography of grinding wheels present certain advantages and disadvantages for the topography determination. Generally, the static methods and the post-process dynamic methods enable high defined surface topographies which lead to important applications for scientific issues. The high time-consuming procedures related to these methods represent their major drawbacks, thus preventing an application and integration in industry. The in-process dynamic methods can be integrated in the production process but the significance of the results is mostly not sufficient to describe the topography of grinding wheels.

In such a context, nowadays it is still highly required to establish a dynamic in-process characterization method, which can be used to assess the topography of conventional grinding wheels aiming at a suitable process control, independently from the manufacturing source of the grinding wheel.

Therefore, the main goal of the present research consists in defining a suitable Dynamic In-process Characterization Method (DICM), which relies on the development of an AE-based quick test method (AE Quick Test Method). By in-process characterizing the topography of conventional grinding wheels, the AE Quick Test Method has the major goal of maintaining constant quality in the course of the grinding process with regard to a predefined working result. The possibility of in-process characterizing the grinding wheel´s topography by means of the proposed AE Quick Test Method consists in the great novelty and contribution of the current research. The method is intended to extract in-process quantified information related to the grinding wheel´s topography features, without neither interrupting the grinding process nor changing the experimental setup. Besides, it also aims to achieve in-process information related to the topography of the grinding wheel, by using common and real grinding wheel velocities which are usually employed in industrial praxis (i.e., v_s= 30 m/s). This is carried out with no need to decelerate the cutting speed of the grinding wheel (v_s), thus representing a more feasible information related to the

grinding process. Further goals of the current research are to: a) conduct planned experiments in order to study the performance of the method and to determine the influencing variables on its response; b) propose and implement signal processing techniques which can help to obtain in-process information from the acquired AE_{RAW} signals through the AE Quick Test Method; c) compare the efficiency of two different scanning trajectories during the assessment of the grinding wheel´s topography; d) validate the results derived from the AE Quick Test Method; e) define an optimized condition for the AE Quick Test Method regarding the main influencing factors which play an important role on its output.

The upcoming chapters describe the devices and measuring procedures, the experimental planning and methodologies, the achieved results in the course of the current research and the validation of the proposed DICM.

4 DEVICES AND METHODS

This chapter introduces the principal devices and the developed experimental rigs which have been employed for conducting the scheduled experiments with regard to the Dynamic Post-process Characterization Method (DPCM) as well as to the Dynamic In-process Characterization Method (DICM). In addition, the measuring procedures and devices utilized to validate the results related to both methods are also mentioned.

4.1 GRINDING MACHINES

During the experiments concerning the DPCM, a universal cylindrical CNC grinding machine (Company: Zema Zselics Ltda, type: Pratika Flexa 600-L) has been used, which is equipped with a specific control system (Company: Siemens, type: Sinumerik 840D) as well as its designed drive system (Company: Siemens, type: Simodrive 611D), Figure 20.

Figure 20 – Universal cylindrical CNC grinding machine (Zema Zselics Ltda Pratika Flexa 600-L).

Source: Adapted and based on (ZEMA, 2002).

This grinding machine is designed for manufacturing small and medium size batches in industrial activities and allows grinding a vast

range of profiles. The grinding machine possesses a drive power of 5,6 kW (7,5 HP). By using the maximum available drive power of the grinding machine, it is possible to use cutting speeds up to 100 m/s when employing a 400 mm diameter grinding wheel. The displacement of the grinding wheel´s head on both the longitudinal direction (Z-axis) and the traversal direction (X-axis) occurs by means of hydrostatic guideways and servomotors. The grinding machine permits to grind components which present up to 600 mm in length and up to 275 mm in diameter (ZEMA, 2002). Figure 21 displays the working chamber of the grinding machine and its main components and moving axis.

Figure 21 – Working chamber of the universal cylindrical CNC grinding machine (Zema Zselics Ltda, Pratika Flexa 600-L).
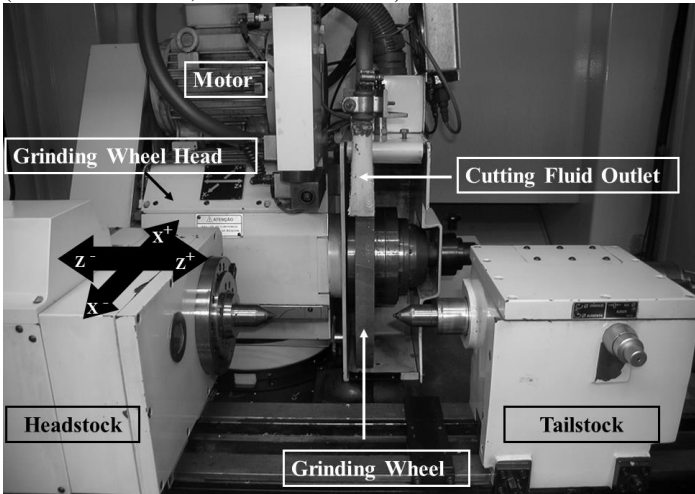
Source: Adapted and based on (ZEMA, 2002).

        The center assemblies mounted on both the headstock and on the tailstock are fixed, so that the rotation of the workpiece is carried out by using an eccentric pin (i.e., driving dog) attached to the headstock´s spindle. The positioning and clamping of the tailstock is adjusted manually and its moving center can be activated by means of a pedal on the external bottom side of the grinding machine. For clamping the workpiece between centers, a compression spring is available.
        In the course of the experiments valid for the DICM, an universal cylindrical CNC grinding machine (Company: Schaudt Mikrosa BWF GmbH, type: PF 51) was employed. This grinding machine is equipped with both a specific control system (Company: Siemens, type:

Sinumerik 840D) and its appropriate drive system (Company: Siemens, type: Simodrive 611D), Figure 22.

Figure 22 – Universal cylindrical CNC grinding machine (Schaudt Mikrosa BWF, PF 51).

Source: Adapted and based on (SCHAUDT, 2010).

Due to its modular design, the universal cylindrical grinding machine is suitable for the manufacture of small and medium batch sizes in industrial praxis. Even complete machining in one clamping, with a whole range of different materials (such as special steel, ceramics, silicate and rubber) is possible. This allows a variety of applications to be considered (SCHAUDT, 2010).

The grinding machine is designed for grinding workpieces presenting up to 250 kg weight, up to 1000 mm length, and up to 445 mm in diameter. It also enables diverse grinding operations such as external cylindrical plunge grinding, internal cylindrical grinding, and out of round grinding operations (SCHAUDT, 2010). The drive power of the wheel head corresponds to 25 kW which allows achieving cutting speeds up to 200 m/s when using a 500 mm diameter grinding wheel. Besides the possibility of using oil as cutting fluid, the grinding machine also presents the potential for high-performance grinding operations with CBN grinding wheels, which are highly required in industrial praxis (KIRCHGATTER, 2010). Figure 23 displays the working chamber of the grinding machine and its main components and moving axis.

Figure 23 – Working chamber of the universal cylindrical CNC grinding machine Schaudt Mikrosa BWF, PF 51.
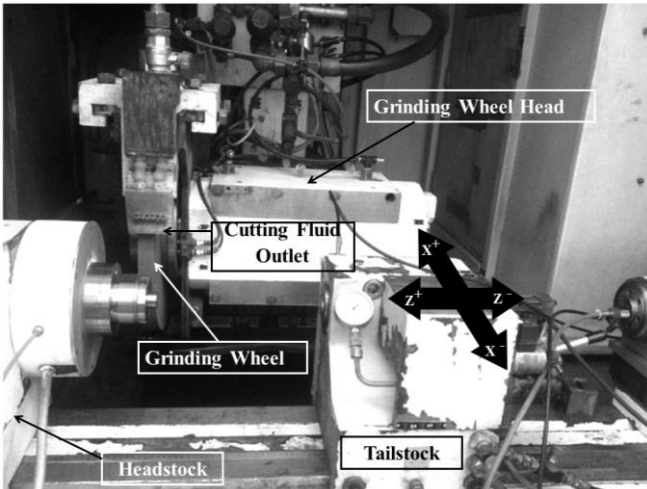
Source: Adapted and based on (SCHAUDT, 2010).

4.2 WORKPIECES

For conducting the planned experiments in the scope of the actual research, it was necessary to design and to manufacture appropriate workpieces. Figure 24 schematically illustrates the geometric and technical specifications for the manufactured workpieces (material: nodular casting iron, mean hardness: 236 HV, quantity= 2), aiming at the DPCM´s experiments.

Figure 24 – Workpieces for the experiments regarding the Dynamic Post-process Characterization Method (DPCM).
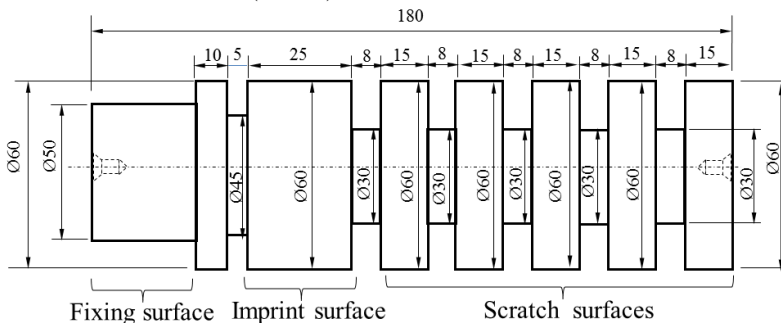
Source: (Developed by the author), dimensions in mm.

Each workpiece presents five cylindrical surfaces (Ø= 60 mm, width= 15 mm) which were machined and prepared for the Scratch Experiments (see Section 5.3.1). The width of such cylindrical surfaces was designed as being smaller than the grinding wheel´s width, in order to assure a constant contact area between the grinding wheel and the ground surface during the Scratch Experiments. Besides, the workpieces also present a cylindrical surface (Ø= 60 mm, width= 25 mm) in which the grinding wheel is imprinted (after the Scratch Experiments), aiming at the estimation of the radial wear of the grinding wheel over predefined stages of the experiment series. The clamping of each workpiece in the grinding machine occurs between centers (tailstock and headstock), by using the centering hole machined on the right side of the workpiece as well as the fixing surface of the workpiece.

The workpieces for the DICM´s experiments were delivered by the company Nose Seiko Co., Ltd., Osaka, Japan. These workpieces consist of inner rings commonly employed for manufacturing needle roller bearings in the same company. Figure 25 illustrates the geometric and technical specifications for the manufactured workpieces (material: hardened steel alloy 100Cr6, mean hardness: 860 HV, quantity= 12), which have been used during the DICM´s experiments.

Figure 25 – Workpieces for the experiments regarding the Dynamic In-process Characterization Method (DICM).
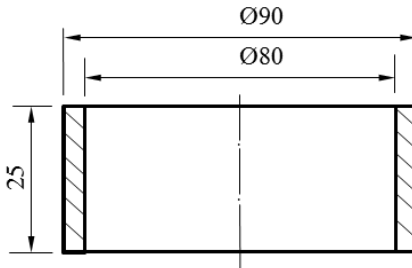
Source: (Developed by the author), dimensions in mm.

The width of each workpiece is smaller than the grinding wheel´s width, thus allowing constant contact between the grinding wheel and the workpiece during the Scratch Experiments (see Section 5.3.1). Due to the small width of the workpiece, it is clamped directly in the headstock of the grinding machine by previously mounting it on a specific support, (see Appendix A).

4.3 GRINDING WHEELS

The grinding wheels employed in this research were fused aluminium oxide grinding wheels, which have been manufactured and delivered by the company Lapport Schleiftechnik GmbH.

Two similar fused aluminium oxide grinding wheels were utilized for the experiments regarding both the DPCM and the DICM. Table 2 detaches the main technical specifications of the conventional grinding wheels.

Table 2 – Grinding wheels´ technical specifications.

Technical Data	DPCM experiments	DICM experiments
Complete specification	400x30x127A80J6V580	500x30x203,2A80J6V580
External aspect	Ruby (dark-red)	Ruby (dark-red)
External profile	Flat	Flat
Grain type	Fused aluminium oxide	Fused aluminium oxide
Grain size	F80 (185 μm average)	F80 (185 μm average)
Wheel hardness	Medium (J)	Medium (J)
Porosity	Medium (6)	Medium (6)
Bond	Ceramic (V)	Ceramic (V)
Outer diameter	400 mm	500 mm
Inner diameter	127 mm	203,2 mm
Width	30 mm	30 mm
Max. rotation	1528 min^{-1}	1910 min^{-1}
Max. cutting speed	40 m/s	50 m/s

Source: Adapted and based on (LAPPORT, 2010).

4.4 ACOUSTIC EMISSION MONITORING DEVICES (AE/MD)

AE measurements in the course of the present research were carried out by using two different AE monitoring devices (AE/MD). Either AE monitoring devices allow monitoring the dressing process and the AE events originated during the scheduled experiments (see Chapter 5). Next section describes the most important characteristic of both AE monitoring devices.

4.4.1 Acoustic Emission Monitoring Device (AE/MD-1)

During the DPCM´s experiments, an AE monitoring device (AE/MD-1) delivered by the company Sensis Ltda, was employed. The AE/MD-1 is composed of an AE monitoring system, AE-MS (type: MSM) and an AE transducer, Figure 26. The AE/MD-1 can be used for process monitoring both in industrial and in academia-related activities. The mounting of the AE transducer in the grinding machine is carried out by using an M6 screw. In order to get a reliable signal, the mounting surface needs to be smooth and free of debris.

Figure 26 – Acoustic emission monitoring device (AE/MD-1).
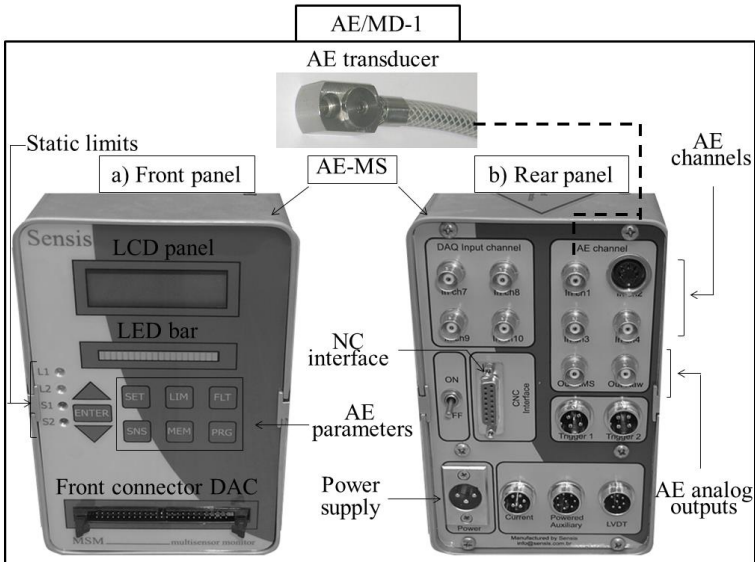
Source: Adapted and based on (SENSIS, 2002).

The small size of the AE transducer permits to mount it near to the source of AE events in the grinding machine, thus contributing to obtain an AE signal with less influence from other sources. After recognizing the AE events from the process and convert them into a proportional electrical signal, the AE transducer´s output signal is directly transferred to the AE-MS (through the BNC input connection "In ch1", rear panel, Figure 26-b), by means of an appropriate cable. Up to 13 AE transducers can be connected to the AE-MS´s rear panel, but only one-at-a-time is available for use. Additional connections for the

power supply, machine communication (DB 15-pin), and AE analog output signals (AE_{RAW} and AE_{RMS}) are available in the rear panel of the AE-MS.

The AE-MS accomplishes the conditioning of the AE_{RAW} signal delivered from the AE transducer. As the AE_{RAW} signal presents a high frequency content (10 kHz up to 900 kHz), signal conditioning is carried out by appropriately selecting the values of gain, noise reduction, and analog filters in the front panel´s menu box, Figure 26-a. Additionally, it is also possible to select the value of the integration time constant (ΔT) for the evaluation of the root mean square level (AE_{RMS}) of the AE_{RAW} signal. The front panel also presents a DAC connector which allows transferring the input signals to a data acquisition device. Additional LEDs (L1, L2, S1, S2 and LED bar) enable the observation of the AE intensity during the monitoring procedure.

4.4.1.1 Set up of the acoustic emission monitoring system (AE-MS)

When employing the AE/MD-1 during the DPCM´s experiments, some principal AE parameters were selected by means of the AE-MS. Both the AE parameters and their set values are described in this section. The AE parameters which have been set are mainly related to the AE signal gain, AE signal sensitivity, and the analyzed bandwidth of the AE_{RAW} analog signal. Table 3 summarizes the main AE parameters selected during the Scratch Experiments and the AE Tactile Scanning Experiments (see Chapter 5) with regard to the DPCM.

Table 3 – Set of the AE parameters in the AE monitoring system (AE-MS).

AE Parameters	Scratch Experiments	AE Tactile Scanning Experiments
AE transducer channel	Channel-1	Channel-1
Signal gain	7 %	30 %
Noise reduction	99 %	99 %
Static thresholds 1 and 2	6 %	6 %
Low-pass analog filter	50 kHz	100 kHz
High-pass analog filter	0 Hz	5 kHz

Source: Adapted and based on (SENSIS, 2002).

The parameter "AE transducer channel" ("*Canal de Entrada*", button "SET", selecting menu in the front panel) activates the AE transducer for the experiments. Among the four available input channels

for the AE transducers, channel 1 ("In ch1") was used during both the Scratch Experiments and the AE Tactile Scanning Experiments.

The gain adjustment of the AE signal is set by means of the parameter "Signal gain" ("*Ganho de sinal*", button "SET", selecting menu in the front panel), and consists in a relative percentage value which ranges from 0 % up to 100 %. The higher value of the parameter "Signal gain" for the AE Tactile Scanning Experiments (in comparison with the value used during the Scratch Experiments) is due to the shallow interferences between the grinding wheel and the diamond tip in the elastic deformation range.

The reduction of the signal ground noise is possible by using the parameter "Noise reduction" ("*Redução de ruído*", button "SET", selecting menu in the front panel) (SENSIS, 2002). The higher the value of this parameter, the smaller is the influence of the ground noise on the AE signal. This parameter was set at its highest possible value during the experiments.

The parameter "Static threshold" ("*Limite*", button "LIM", selecting menu in the front panel) permits selecting two static thresholds which act as comparative levels related to the signal ground noise. Such parameter has only been used previously to the AE Tactile Scanning Experiments (see Section 5.3.2), in order to define a reference position on the grinding wheels´ periphery.

Regarding the AE analog filters, two different frequency bandwidths (B) have been employed, by appropriately setting the values of both the analog high-pass filter (HP) and the analog low-pass filter (LP). The bottom frequencies of both bandwidths (B1 and B2) are based on the AE transducer´s characteristics as well as on the filtering values available by the AE-MS. On the other hand, the upper frequency limits of both bandwidths are highly dependent on the hardware capability (computer and also acquisition device) and at the same time, on the characteristics of the AE transducer.

4.4.2 Acoustic Emission Monitoring Device (AE/MD-2)

In the course of the experiments regarding the DICM, an AE monitoring device (AE/MD-2) manufactured by the company Kistler Instrument AG, has been used, Figure 27. The AE/MD-2 is composed of an AE coupler (type: AE Piezotron 5125) and an AE transducer (type: AE Piezotron 8152B111). The AE/MD-2 is particularly suitable for the monitoring of machine tools and processes in industrial production (KISTLER, 2006). The AE transducer is simply mounted in the grinding

machine by using either an M6-1/4 screw or a magnetic clamp. A minimum tightening torque is sufficient for a constant coupling. The smoother the mounting surface, the better is the achieved result. Additionally, the use of a highly viscous grease (e.g., silicone grease) between the coupling surfaces is also recommended (KISTLER, 2007).

Figure 27 – Acoustic emission monitoring device (AE/MD-2).
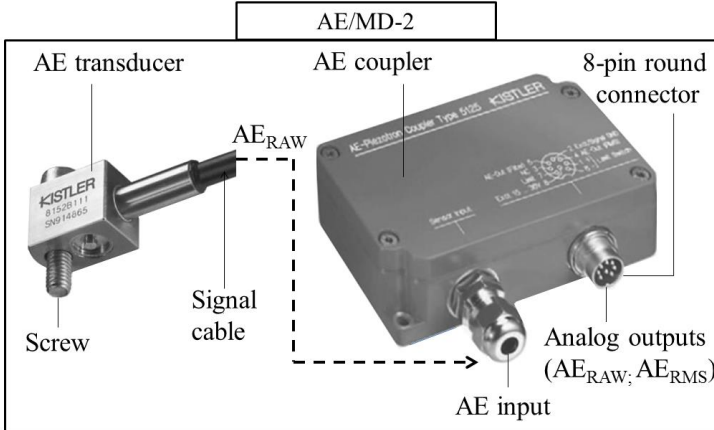
Source: Adapted and based on (KISTLER, 2006, 2007).

The AE coupler supplies power to the AE transducer and processes its high frequency output signals. Gain, filters and integration time constant of the built-in RMS converter are designed as plug-in modules. This allows suitable adaptation to the particular monitoring issue (KISTLER, 2006).

By means of a jumper, the gain can be set to (1x), (10x), or (100x). The amplifier has two series-connected second order filters, designed as plug-in elements. The type of the filter (high-pass or low-pass) and its frequency limits are freely selectable. A band-pass filter is obtained by the series connection of one high-pass and one low-pass filter. The integration time constant of the RMS converter can be freely selected. The following output signals are available in the 8-pin round connector: a) Two analog output signals AE-Out (Raw and RMS), and b) a digital output signal (Limit Switch). Figure 28 shows the block diagram of the AE/MD-2, illustrating its signal conditioning chain.

The AE transducer presents a high sensitivity and a broad frequency response (from 0 Hz up to 1000 kHz) being especially well-suited for measuring wide frequency AE events in the range from 50

kHz up to 400 kHz (flat frequency response) (KISTLER, 2007). Such AE events can be originated, for example, from plastic deformation of materials, crack formation and growth, fracturing or friction. Application examples commonly found are: a) monitoring of metal cutting and forming processes, and b) monitoring of tools and machines. Both the rugged construction and the firmly welded housing of the AE transducer allow it to operate under harsh environmental conditions (KISTLER, 2007).

Figure 28 – Block diagram and signal conditioning chain of the AE monitoring device (AE/MD-2).
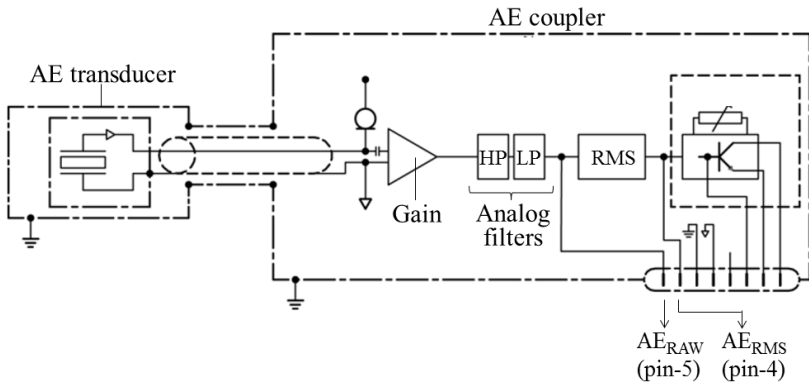
Source: Adapted and based on (KISTLER, 2007).

Due to its small size, it mounts close to the source of AE emission in order to adequately capture the signal. A miniature impedance converter is built into the AE transducer, giving an output low-impedance voltage signal (KISTLER, 2007).

After acquiring the AE events from the process and converting them into a voltage signal, the transducer´s analog voltage raw signal (AE_{RAW}) is directly transferred to the AE coupler by means of an appropriate cable. Next, the AE coupler firstly amplifies the original analogue AE_{RAW} signal, and then band-pass filters it, according to the previous selected values of both the high-pass filter (HP) and the low-pass filter (LP). At this stage, the filtered analogue AE_{RAW} signal is available in the 8-pin round connector´s output (pin-5). Additionally, it is also possible to evaluate the root mean square value (i.e., RMS, labelled as AE_{RMS}) of the analog AE_{RAW} signal, which is in turn also available as an analog signal in the 8-pin connector´s output (pin-4).

4.4.2.1 Set up of the acoustic emission coupler (AE coupler)

      This section describes the main AE parameters and their adjusted values when using the AE coupler throughout the planned experiments related to the DICM. Those parameters are basically associated with the gain (amplification) and the analyzed bandwidths of the AE_{RAW} analog signal as well as the integration time constant (ΔT) for evaluating the AE_{RMS} value of the AE_{RAW} analog signal. Table 4 summarizes the main AE parameters which were selected during the AE Tactile Scanning Experiments.

Table 4 – Set of the adjusted AE parameters in the AE coupler.

AE parameters	AE Tactile Scanning Experiments
Signal gain	10 x (V)
Frequency bandwidth 1 (B1)	HP= 5 kHz; LP= 100 kHz
Frequency bandwidth 2 (B2)	HP= 5 kHz; LP= 200 kHz
Integration time constant (ΔT)	1,2 ms

Source: Adapted and based on (KISTLER, 2006).

      The gain adjustment of the AE_{RAW} analog signal occurs by means of a specific jumper, in order to enable reliable signal to noise ratio and proper signal sensitivity, Figure 29.

      Regarding the filtering adjustment, two different bandwidths (B) have been investigated, by setting appropriately values of both analog high-pass filter (HP) and the analog low-pass filter (LP). The bottom frequencies of either bandwidths (i.e., B1 and B2) are based on the AE transducer´s characteristics as well as on the electrical circuit of the AE coupler. In order to by-pass the lower frequency content of the AE transducer, a filter-bridge (without analog filtering, that is, HP= 0 Hz) is required and needed to be installed in the interior of the AE coupler, Figure 29.

      On the other side, the upper frequency limits of both bandwidths B1 and B2 are highly dependent on the hardware capability (computer and also acquisition device) and at the same time, on the characteristics of the AE transducer. The upper values of B1 and B2 were band-limited based on the cut-off frequency ($f_{cut-off}$) of the analog LP filter being employed. During the experiments these values were set to $f_{cut-off,1}$= 100 kHz and $f_{cut-off,2}$= 200 kHz, respectively, Figure 29.

Figure 29 – Schematic representation of the AE coupler and its main AE parameters.
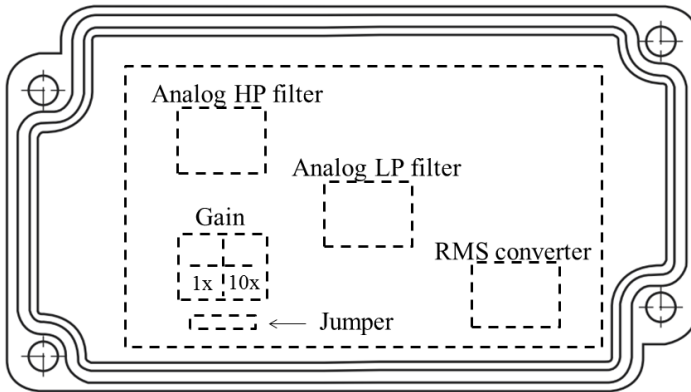
Source: (KISTLER, 2006).

For evaluating the analog AE_{RMS} value from the original analog AE_{RAW} signal, the selection of an integration time constant (ΔT) is required. This value was set to $\Delta T = 1,2$ ms and installed in the "RMS converter" of the AE coupler, Figure 29.

4.5 CUTTING FORCE MONITORING DEVICE (FORCE/MD)

The assessment of the grinding cutting force components and torque during the experiments with respect to the DICM were carried out by using a specific cutting force monitoring device (Force/MD) manufactured by the company KISTLER INSTRUMENTE AG, Figure 30.

The Force/MD comprises a rotating dynamometer (type: 9124B1111), a stator (type: 5221B) and a multichannel signal conditioner, Force-MSC, (type: 5223B2). The rotating dynamometer consists of a four component transducer fitted under high preload between a baseplate and a top plate. The transducer is mounted ground-insulated, hence ground loop problems are largely eliminated. For each component, a 2-range miniature charge amplifier is integrated into the dynamometer. The dynamometer is rust-proof and water-resistant so that splash water and cooling effects do not damage the system (KISTLER, 2008).

The output voltage signal of the dynamometer´s charge amplifier is digitized and transmitted by telemetry to the stator which demultiplexes the signal and converts it into an analog signal.

Figure 30 – Cutting force monitoring device (Force/MD).
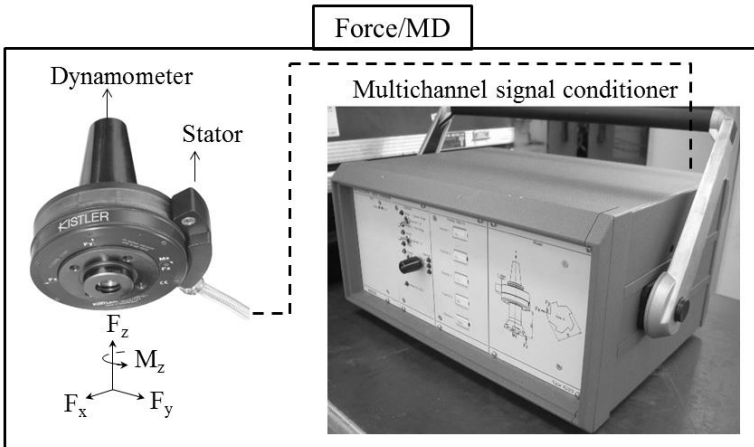
Source: Adapted and based on (KISTLER, 2008).

The stator also operates as a sending unit (by means of an antenna), thus transmitting by telemetry the power supply for the electronics incorporated into the rotating dynamometer. Furthermore, it controls the signals for the range selection (range 1 and range 2), and to operate/reset the device. The stator must be mounting concentric with the dynamometer, by maintaining a gap in a range of 1 mm up to 2 mm (KISTLER, 2008).

By means of an appropriate cable, the analog-converted signal in the stator is sent to the multichannel signal conditioner (Force-MSC) which low-pass filters the analog signal. The cut-off frequency of the low-pass filter is 1 kHz. After the low-pass filtering stage, the analog signal is available on the output connection of the Force-MSC. The Force-MSC is both the signal output and the supply/control unit for the rotating dynamometer (KISTLER, 2008).

4.5.1 Set up of the Multichannel Signal Conditioner (Force-MSC)

This section describes the main connections and parameters when using the Force-MSC (Figure 31) throughout the planned experiments related to the DICM. The set parameters are basically associated with the selected measuring range and the signal gain (amplification). There are two measuring ranges which are available by the Force-MSC. The measuring ranges can be chosen by means of the switch "Measuring ranges" Figure 31-a.

Figure 31 – Multichannel signal conditioner (Force-MSC).

a) Front panel
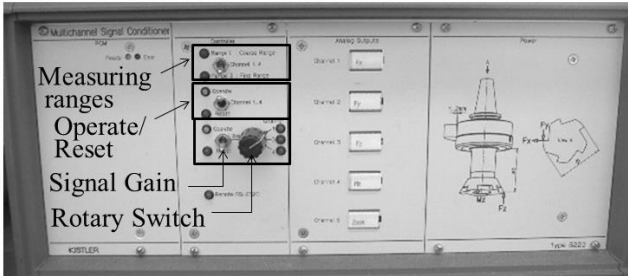
b) Rear panel
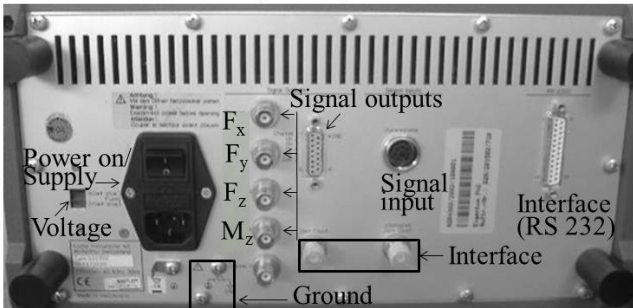
Source: Adapted and based on (KISTLER, 2008).

Measuring range 1 is a coarse range which allows measuring at maximum loading of the dynamometer (-20 kN < F_x < 20 kN; -20 kN < F_y < 20 kN; -30 kN < F_z < 30 kN and -1100 N.m < M_z < 1100 N.m). Measuring range 2 is required for measuring small force components in a finest range (-2 kN < F_x < 2 kN; -2 kN < F_y < 2 kN; -3 kN < F_z < 3 kN and -110 N.m < M_z < 110 N.m). The ratio between the Range 1 and the Range 2 is 10 (KISTLER, 2008).

During the experiments with respect to the DICM, the range 2 was selected, then enabling the evaluation of the grinding cutting force components F_x, F_y, F_z, and M_z. After switching from one range to the other it is recommended to actuate the "Operate/Reset" switch, Figure 31-a. The reason for this is that the action of switching can yield a very small signal offset. Switching in the course of measurements is not appropriate, since the sensitivity at the data acquisition system must also be changed (KISTLER, 2010). On the front panel of the Force-MSC it is also possible to select the signal gain in order to obtain a better signal to

noise ratio. The signal gain is activated by firstly turning on the switch "Signal Gain" Figure 31-a.

For selecting the channel which should be amplified one needs to use the "Rotary Switch". The signal gain can be switched in at any time, then enabling a signal amplification of 10x (KISTLER, 2010). Throughout the DICM´s experiments, no signal gain was set in the Force-MSC, as the signal to noise ratio during the grinding process was significantly high in comparison with the ground noise of the signal.

The main input and output connections are available on the rear panel of the Force-MSC, Figure 31-b. The connection "Signal input" receives the analog signal sent from the stator. After conditioning the analog signal, the Force-MSC permits further use of the conditioned cutting force signal components (i.e., F_x, F_y, F_z, and M_z) by using its signal outputs "channel 1", "channel 2", "channel 3" and "channel 4", respectively. Figure 31-b also detaches additional buttons and connections for power supply, voltage selection, signal ground, and the connections for interfacing the device with the CLP of the grinding machine (KISTLER, 2008).

4.6 DATA ACQUISITION DEVICES (DAD)

This section describes the data acquisition devices (DAD) that have been used for acquiring and digitizing both AE and the grinding cutting force signals during the scheduled experiments in the scope of the current research. The experiments in connection with the DPCM aim at measuring only the AE signals derived from both the Scratch Experiments and the AE Tactile Scanning Experiments (see Section 5.1). On the other hand, the experiments related to the DICM employ a transducer-fusion technique in which the AE signals are measured during the AE Tactile Scanning Experiments, whereas the grinding cutting force signals are used for monitoring the Scratch Experiments (see Section 5.2).

4.6.1 Data Acquisition Device (DAD-1) for Experiments regarding the Dynamic Post-process Characterization Method (DPCM)

The acquisition and digitization of the AE_{RAW} analog signals derived from the AE/MD-1´s outputs have been implemented by means of a data acquisition device (DAD-1) from National Instruments (type: NI USB-6218, 32 analog inputs channels, 16-Bit), Figure 32.

Figure 32 – Data acquisition device (DAD-1) for the Dynamic Post-process Characterization Method (DPCM)´s experiments.
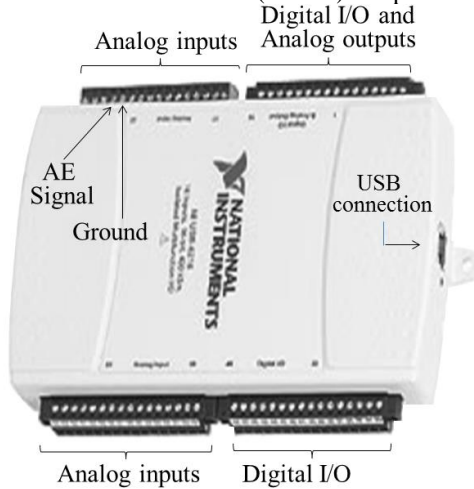
Source: Adapted and based on (NATIONAL, 2012).

For transmitting the analog AE_{RAW} signals, a coaxial cable was used and connected to both the channel "Ground" (channel 28) and to the input channel "AE Signal" (channel 29) in the DAD-1. The DAD-1 is specifically intended to test, control, and design applications including field experiments. Signal digitization is achieved by using sampling rates of up to 250 kS/s (single channel mode).

When acquiring signals in multiple channels, the maximum sampling rate per channel corresponds to the ratio between the maximum available sampling rate (250 kS/s) and the total number of active channels being used (NATIONAL, 2012). The sampled signals are then transmitted per USB cable to a personal computer, aiming at the signal processing and data storage.

4.6.1.1 Set up of the data acquisition device (DAD-1)

For measuring the AE analog signals during the experiments regarding the DPCM, some specific connections and settings were selected in the DAD-1. The acquisition of the AE_{RAW} analog signals (derived from the AE/MD-1´s AE_{RAW} analog output) has been implemented by firstly connecting the AE_{RAW} analog signal to the input channel of the DAD-1 (channel 29, analog input 6, AI 6). For this task, a coaxial cable was employed, thus avoiding external disturbances in the

acquired AE_{RAW} signals. Over the course of the experiments, the main settings for acquiring and digitizing the AE_{RAW} analog signals have been set by using a particular computational algorithm (Algorithm-1, Labview programming language) developed in the current research. Algorithm-1 provides an interface between the DAD-1 and the used computer aiming at visualizing and storing the acquired AE_{RAW} signals. Figure 33 shows the Algorithm-1´s user interface and its main AE acquisition parameters, tabs and output graphs. Programming functions are available in the Algorithm-1´s block diagram.

Figure 33 – Algorithm-1´s user interface.
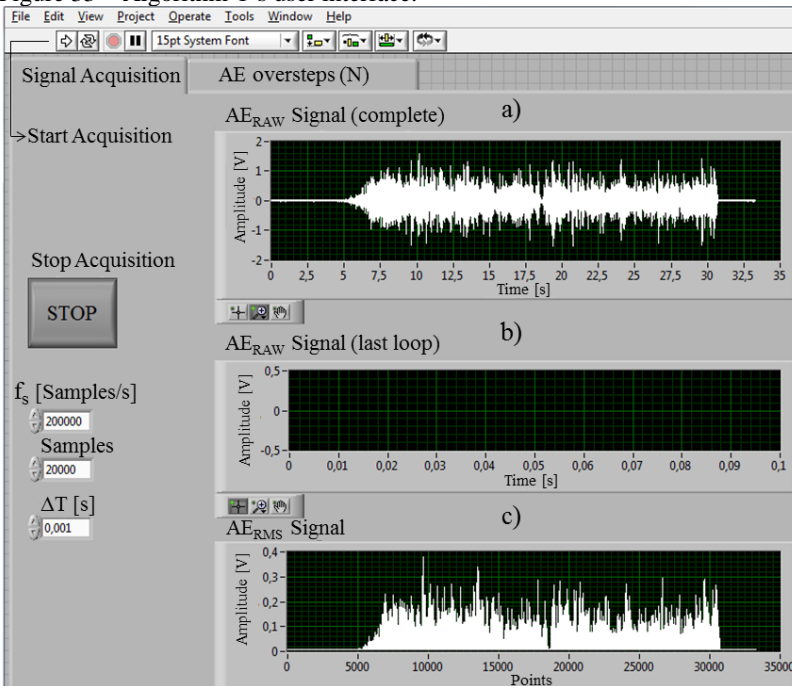
Source: (Developed by the author).

The user interface of the Algorithm-1 consists of two tabs. In the first tab "Signal Acquisition" one can choose the main parameters for signal acquisition and signal digitization. The second tab "AE oversteps (N)" is employed for characterizing the topography of the grinding wheel after the experiments have been finished (i.e., post-process analysis). Signal acquisition starts by firstly selecting the main acquisition parameters (i.e., sampling rate f_s, samples to read, input

terminal configuration and the input limits) and afterwards by pushing the "start" button (white arrow on the left upper side of the figure).

The parameter "sampling rate" (f_s) determines the sampling frequency (in samples per second, S/s) aiming at digitizing the acquired AE_{RAW} analog signals. During the AE Tactile Scanning Experiments and the Scratch Experiments such parameter was set to $f_{s,scan}$= 200 kS/s and $f_{s,scratch}$= 125 kS/s, respectively. Both sampling rates were based on the selected values of the cut-off frequencies ($f_{cut-off,scan=}$ 100 kHz and $f_{cut-off,scratch=}$ 50 kHz) of the analog LP filters available by the AE/MD-1. These values comply with the Nyquist´s theorem, thus avoiding the aliasing effect. After acquiring the AE_{RAW} signal, it is possible to plot the entire time history of the AE_{RAW} signals related to the AE Tactile Scanning Experiments (i.e., post-process analysis), Figure 33-a.

The parameter "Samples" specifies de number of samples to read and its selected value is plotted in a specific graph during the AE_{RAW} signal acquisition, Figure 33-b. This parameter was set as a tenth of f_s in order to save computer memory, therefore only 0,1 s is plotted during each loop of the acquisition program. Based on the acquired AE_{RAW} signal, it is also possible to evaluate its RMS value (i.e., $AE_{RMS,}$ root mean square), Figure 33-c. The evaluation of the AE_{RMS} value depends on the parameter "integration time constant" (ΔT) which was set to 1 ms.

The channel´s configuration regarding the source of signal being measured is set in the block diagram of the Algorithm-1 through the parameter "input terminal configuration". During the experiments the parameter "input terminal configuration" was set to "referenced single-ended" (RSE), as the reference for the AE_{RAW} signal consists of pin "AI GROUND" located in the data acquisition device (DAD-1). For adjusting the input limits of the AE_{RAW} signal (i.e., signal range) the parameter "input limit" was set in the block diagram to +/- 5 V. Such range was based on the output range of the AE_{RAW} analog signal derived from the AE/MD-1´s output. For the given values of minimum and maximum limits, the smallest detectable change (i.e., "code width") which can be recognized in the digitized AE_{RAW} signal is determined by Equation 8 (NATIONAL, 2008).

$$CD = \frac{SR}{2^R} \qquad (8)$$

Where "CD" refers to the code width, "SR" means the signal range and "R" is the resolution of the DAD-1. Hence, as R= 16 bits and

SR= 10 V, the code width of the digitized AE_{RAW} signals is CD= 0,00015 V (NATIONAL, 2010). On the left part of the user interface, the button "Stop" halts the signal acquisition and saves the measured AE_{RAW} signal aiming at signal post-analysis in both the time and frequency domains.

4.6.2 Data Acquisition Device (DAD-2) for Experiments regarding the Dynamic In-process Characterization Method (DICM)

For acquiring and digitizing the analog signals sent from the outputs of both the AE/MD-2 and the Force/MD, it was necessary to use an appropriate data acquisition device, DAD-2 (company: National Instruments), Figure 34. The data acquisition device comprises a BNC-Adapter (type: BNC-2110), Figure 34-a, and a multifunctional data acquisition module (type: NI USB-6251 M Series, 16-Bit), Figure 34-b.

Figure 34 – Data acquisition device (DAD-2) for the Dynamic In-process Characterization Method (DICM)´s experiments.
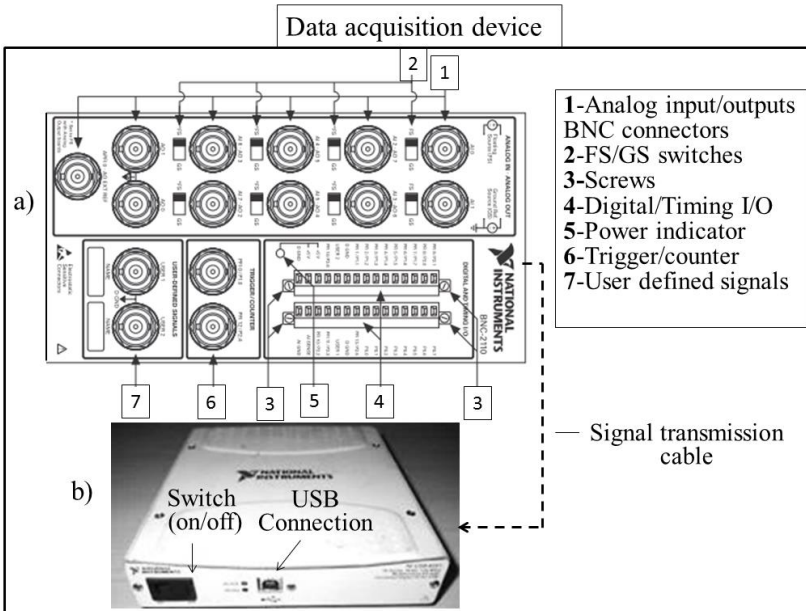
Source: Adapted and based on (NATIONAL, 2007, 2008).

The BNC-Adapter is ideal for simplifying connections between the measurement apparatus and the data acquisition module in

laboratory, test, and production environment. Throughout the experiments, it receives the analog output signals either from AE/MD-2 or from the Force/MD by means of the analog input BNC connectors (a total of 8 are available). In addition, the BNC-Adapter also has 3 BNC connectors for analog output signals, 2 BNC connectors for trigger/count functions, 2 BNC connectors for user-defined signals as well as a spring terminal block with 30 pins for digital and timing I/O signal connections (NATIONAL, 2007).

After being acquired by the BNC-Adapter, the analog signals are sent via appropriate cable to the multifunctional data acquisition module (Figure 34-b) in order to perform signal digitization with a 16-bit resolution. The multifunctional data acquisition module is specially designed for mobile and space-constrained applications. Furthermore, this device is optimized for superior accuracy at fast sampling rates (1,25 MS/s, single channel) thus allowing the digitization of the acquired analog signals. When acquiring signals in multiple channels, the aggregate sampling rate decreases to 1 MS/s, being also divided by the total number of active channels (NATIONAL, 2008). The sampled signals are then transmitted per USB cable to a personal computer, aiming at signal processing.

4.6.2.1 Set up of the data acquisition device (DAD-2)

Depending on the measurements being carried out (either AE or grinding cutting force), particular settings and connections have been selected in the DAD-2. The next sections describe the particularities that have been adopted when measuring both AE and the grinding cutting force signals during the experiments regarding the DICM.

4.6.2.1.1 Connections and settings for acoustic emission measurements

The acquisition of the AE analog signals from the AE/MD-2´s analog outputs has been implemented by firstly connecting both the AE_{RAW} analog signal and the AE_{RMS} analog signal to the BNC-channel 0 (analog input 0, AI0) and to the BNC-channel 1 (analog input 1, AI1), respectively, in the BNC-Adapter. As the signal source (i.e., AE transducer´s signals) of the AE/MD-2 is ground isolated, the FG/FS switches located bellow the AI0 and the AI1 channels were set to FS (floating signal) during the AE Tactile Scanning Experiments (KISTLER, 2007; NATIONAL, 2008).

        The main settings for acquiring and digitizing the AE signals
during the experiments were adjusted by means of a specific
computational algorithm (i.e., Algorithm-2, Labview programming
language), which was developed in the scope of the current research.
Algorithm-2 serves as an interface between the DAD-2 and the used
computer, thus permitting to visualize and to store the acquired signals.
Figure 35 shows the Algorithm-2´s user interface, its main acquisition
parameters, and output graphs. Programming functions are available in
the Algorithm-2´s block diagram.

Figure 35 – Algorithm-2´s user interface.
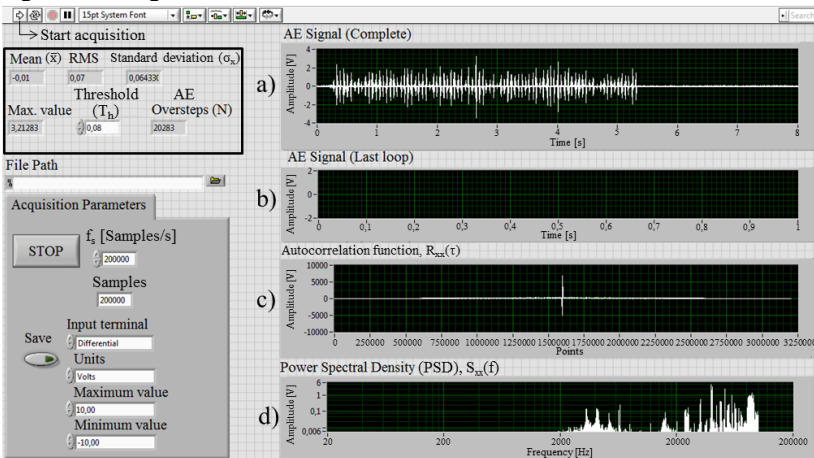
Source: (Developed by the author).

        Signal acquisition can be carried out by firstly inserting the main
acquisition parameters (i.e., sampling rate f_s, samples to read, input
terminal configuration and the input limits) and afterwards pushing the
"start" button (white arrow on the left upper side of the figure).
        The parameter "sampling rate" (f_s) specifies the sampling
frequency (in samples per second, S/s) in order to digitize the acquired
AE analog signals. This parameter was set at two distinct values, being
configured as either $f_{s,1}$= 200 kS/s or $f_{s,2}$= 400 kS/s. Both values were
based on the selected cut-off frequency values ($f_{cut-off,1}$ and $f_{cut-off,2}$) of
the analog LP filters which have been adopted during the AE Tactile
Scanning Experiments (see Section 5.3.2). When using the analog LP
filter with $f_{cut-off,1}$= 100 kHz, the parameter f_s was set to $f_{s,1}$= 200 kS/s,
then complying with the Nyquist theorem and also avoiding aliasing

effect. The same procedure has been utilized when using the analog LP filter presenting $f_{cut-off,2}$= 200 kHz ($f_{s,2}$= 400 kS/s). After acquiring the AE signals, it is possible to plot the entire time history of the AE_{RAW} signals and the AE_{RMS} signals, Figure 35-a.

The parameter "Samples" specifies de number of samples to read and plot them in the following graph (Figure 35-b) during the on-line AE signal acquisition. This parameter was set as a tenth of f_s in order to save computer memory. Another important parameter that needed to be set was the parameter "Input terminal". This parameter permits to choose the channel´s configuration regarding the source of the AE signal being measured. During the AE Tactile Scanning Experiments the parameter "Input terminal" was set to "Differential" due to the electrical characteristics of the signal source (i.e., AE transducer´s signal) which is actually a floating signal. Finally, the parameters associated with the input limits of the AE signals (i.e., "Minimum" and "Maximum" values of the AE signal) were adjusted based on the output range of both the AE_{RMS} and the AE_{RAW} analog signals from the AE/MD-2. As the output of both signals was situated within the range of +/- 5 V, the minimum and maximum values of the input limits were set to -10 V and +10 V, respectively. Such input range affords the highest sensitivity in the DAD-2, and was therefore used in the course of the experiments (NATIONAL, 2004). The selected input limits of the AE signal play an important role on the accuracy of the digitized AE signals. For the given values of minimum and maximum limits, the smallest detectable change (i.e., "code width") which can be recognized in the digitized AE signals is determined by Equation 8. Therefore, the code width of the digitized AE signals was equal to 0,0003 V, which has presented itself as a suitable value to be adopted during the experiments (NATIONAL, 2010).

After acquiring and digitizing the AE signals, Algorithm-2 affords both a time domain as well as a frequency domain analysis in order to in-process characterizing the topography of the grinding wheel. Both analyses are carried out automatically and in-process, after pressing the "stop" button located on the left side of the Algorithm-2´s user interface. By pressing the button "stop" the signal acquisition is halted and the measured AE signals are saved in the computer.

The time domain analysis is based on the in-process evaluation of specific statistical parameters (i.e., RMS value, mean value $\bar{x}$, maximum value, autocorrelation function $R_{xx}(\tau)$, and standard deviation σ_x) as well as on the counting of the AE signal oversteps (N) related to a fixed predefined threshold (T_h). The level of the threshold is defined above the ground noise of the AE signal (previously to the AE

Tactile Scanning Experiments) and inserted in the field "Threshold" (T_h). Algorithm-2 automatically shows the total number of oversteps (N) in relation to the given value in the field "Threshold" (T_h). Besides, the calculation of the autocorrelation function of the AE signals, i.e., $R_{xx}(\tau)$, also occurs automatically and is plotted in the user interface, Figure 35-c. On the other hand, the frequency domain analysis is based on the in-process evaluation of the Power Spectral Density function (PSD) of the AE_{RAW} signal, i.e., $S_{xx}(f)$, Figure 35-d. Settings of the main parameters which exert influence on the PSD´s output, are carried out directly in the block diagram of the Algorithm-2. For evaluating the PSD, the basic parameters and settings that have been used are listed as follows: d.1) "window": Hanning; d.2) "amplitude": dB; d.3) "averaging mode": RMS averaging; and d.4) "number of averages": 100.

4.6.2.1.2 Connections and settings for cutting force measurements

The acquisition of the grinding cutting force signals derived from the Force-MSC´s analog outputs has been implemented by initially connecting the main cutting forces components (F_x, F_y, F_z, and M_z) to the specific channels in the BNC-Adapter (analog input 0, AI0; analog input 1, AI1; analog input 2, AI2, and analog input 3, AI3, respectively). The connection was carried out by means of appropriate coaxial cables between the Force-MSC´s analog outputs and the input channels in the DAD-2. As the signal source (i.e., dynamometer´s signal) from the Force/MD is ground isolated, the FG/FS switches located under the channels AI0, AI1, AI2, and AI3 were set to FS (floating signal) during the experiments (KISTLER, 2008; NATIONAL, 2008).

The main settings for acquiring and digitizing the cutting force signals throughout the DICM´s experiments were set by means of a previously existing computational algorithm. When acquiring the grinding cutting force signals the most important parameters which have been selected were: a) sampling rate, (f_s); b) samples to read; and c) input limits.

The parameter "sampling rate" (f_s) defines the sampling frequency (in samples per second, S/s) in order to digitize the acquired grinding cutting force analog signals. As the cut-off frequency per channel ($f_{cut-off}$) of the LP analog filters in the output of the Force-MSC is $f_{cut-off}$= 1 kHz, the parameter f_s was set to a constant value of f_s= 15600 kS/s, then avoiding aliasing in the acquired signals. In addition, the parameters "samples to read" and "input limits" have also been set to constant values of 100 samples, and +/- 10 V, respectively.

4.7 ROUGHNESS/PROFILE MEASURING SYSTEM

For the evaluation of roughness and profile measurements in the scope of the current research, a specific measuring system (type: Nanoscan 855) from the company Hommel-Etamic (Jenoptik AG group) was employed. This measuring system allows measuring roughness and contour characteristics on either curved or inclined surfaces with a resolution of 0,6 nm and a measuring stroke of 24 mm. Additionally, fast and NC-controlled measuring axes enable automatic measuring runs, with the help of a measuring software which accompanies the roughness measuring system, Figure 36 (JENOPTIK; HOMMEL, 2008, 2009).

Figure 36 – Roughness/profile measuring system (Nanoscan 855).
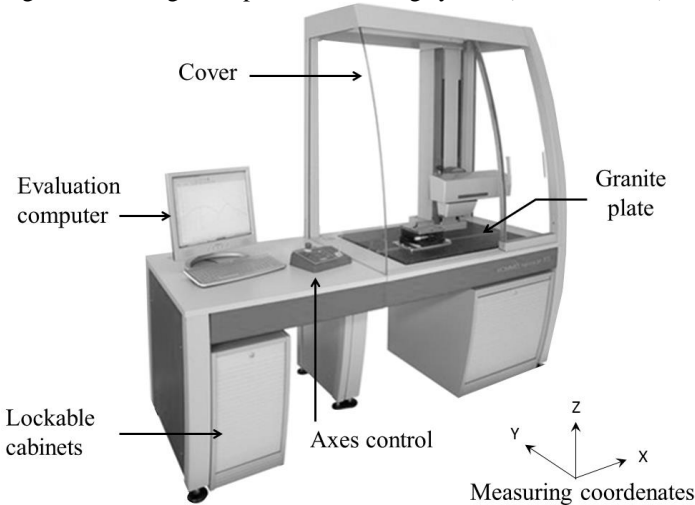
Source: Adapted and based on (JENOPTIK; HOMMEL, 2009).

The overall design of the Nanoscan 855 features two distinct areas: a) working table; and b) measuring table. The measuring table contains an integrated granite plate, an active level regulation and a vibration dampening that guarantee reliable measurement results. The working table contains the evaluation computer and a printer. The most important functions are performed directly on the control panel, by completely observing the measuring process (JENOPTIK; HOMMEL, 2009). For reducing external disturbances during measurements, a cover is also available with the Nanoscan 855.

4.7.1 Roughness/Profile Measurements on Ground Workpieces regarding the Dynamic Post-process Characterization Method (DPCM)´s Validation

Roughness and profile measurements on workpieces ground throughout the DPCM´s experiments have been carried out by using the Roughness/profile measuring system (Nanoscan 855). In order to effectively accomplish the roughness and profile measurements of the workpieces, a common NC clamping head was mounted on the left side of the Nanoscan 855, Figure 37. Besides the possibility of clamping the cylindrical workpiece aiming at maintaining it fixed during the measurements, the NC clamping head also allows to rotate the workpiece in previous defined angular displacements, with the help of a rotary chuck. The angular displacements are NC-commanded by means of the integrated software which accompanies the roughness measuring system.

Figure 37 – Nanoscan 855´s measuring chamber.
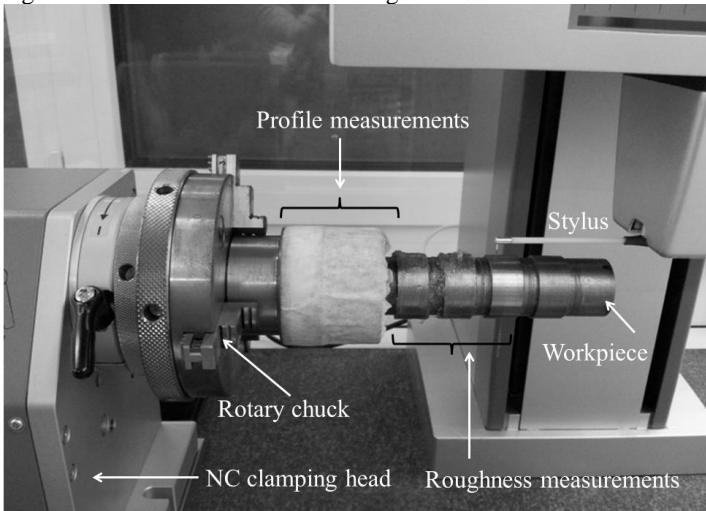
Source: Adapted and based on (JENOPTIK; HOMMEL, 2009).

Roughness measurements on the specified workpieces´ surfaces were evaluated by using both a predefined procedure and a stylus (Figure 37), based on the roughness standards (DIN EN ISO 4288; DIN EN ISO 3274 *apud* JENOPTIK; HOMMEL, 2008). These standards define the main measuring conditions which needed to be adopted concerning

the stylus´ tip radius and additional measuring parameters, in order to correctly evaluate the surface roughness. According to such roughness standards, the definition of the measuring conditions depends firstly on the appropriate selection of the parameter "cut-off" (λ_c), which is directly associated with a previous knowledge of the workpiece´s roughness to be measured. The lack of such previous information has conducted to the selection of the parameter λ_c to the standardized value of λ_c= 0,8 mm. Based on the value of λ_c, the stylus´ tip radius was also defined as r_{stylus}= 5 µm. In order to verify whether the values of both λ_c and r_{stylus} were reasonable to be used, an initial measurement was carried out and the obtained measuring result (R_z parameter) was compared with the threshold value of R_z= 2 µm. As the roughness measurement result was higher than R_z= 2 µm, the values of both λ_c and r_{stylus} were considered suitable for the roughness measurements (DIN 4768, 1990; JENOPTIK; HOMMEL, 2008). The same procedure was carried out for all the workpieces´ surfaces to be measured. Table 5 detaches the main roughness settings and their respective selected values during the roughness measurements on nodular casting iron workpieces.

Table 5 – Settings for roughness measurements on workpieces ground during the Dynamic Post-process Characterization Method (DPCM)´s experiments.

Measuring parameters	**Selected values**
Cut-off (λ_c)	0,8 mm
Traverse length (l_t)	4,8 mm
Traverse velocity (v_t)	0,5 mm/s
Evaluation length (l_n)	4 mm
Shortwave profile filter (λ_s)	2,5 µm
Stylus´ tip radius (r_{stylus})	5 µm
Stylus´ cone angle	90°

Source: Adapted and based on (JENOPTIK; HOMMEL, 2008).

Based on such measuring settings, it was possible to evaluate the surface roughness by conducting 12 equidistant measurements along the periphery of the measuring surface. Hence, each roughness measurement occurs at angular increments of 20° on the workpiece´s surface. With the help of the integrated measuring software, the result of each roughness measurement comprehends a set of specific roughness parameters which are selected before initializing the roughness measurements. The significant roughness parameters which have been evaluated during these measurements were: R_t, R_a, R_{sk}, R_z, R_{max}, R_{pk}, R_k, and R_{vk}. The representative value of the surface roughness corresponds

to the mean value of all 12 measurements for each specific roughness parameter.

Profile measurements on the specified workpiece´s surface were evaluated by using a predefined procedure. This procedure has consisted in linear moving a stylus (tip radius, r_{stylus}= 20 µm) in contact with the workpiece´s surface (i.e., profile measurement surface, Figure 37), by using a constant velocity (v_p= 1 mm/s) across a fixed length (L_p= 20 mm). The result of such measuring procedure consists in a graph which shows de linear distance between both the highest point of the profile and its lowest point. This graph is plotted with the help of the integrated measuring software and represents an estimation of the radial grinding wheel wear (i.e., macrotopography). In order to obtain a representative mean value of the profile deviation, this measuring procedure is carried out three times in different positions over the periphery of the workpiece´s surface.

4.7.2 Roughness Measurements on Ground Workpieces regarding the Dynamic In-process Characterization Method (DICM)´s Validation

Roughness measurements of workpieces ground during the DICM´s experiments have been implemented by using the same measuring system (Nanoscan 855, and its NC clamping head) as previously described in Section 4.7. For correctly selecting the stylus dimensions as well as the main measuring roughness parameters, both standards DIN EN ISO 4288 and DIN EN ISO 3274 have been used (JENOPTIK; HOMMEL, 2008). As the roughness measuring results depend highly on the appropriately selection of both the cut-off (λ_c) and the stylus´ tip radius (r_{stylus}), the selection and inspection of such roughness parameters was conducted based on the same procedure previously mentioned (see Section 4.7.1), thus leading to the following roughness parameters, Table 6.

Table 6 – Settings for roughness measurements on workpieces ground during the Dynamic In-process Characterization Method (DICM)´s experiments.

Measuring parameters	Selected values
Cut-off (λ_c)	2,5 mm
Traverse length (l_t)	15 mm
Traverse velocity (v_t)	0,5 mm/s
Evaluation length (l_n)	12,5 mm
Shortwave profile filter (λ_s)	8 µm
Stylus´ tip radius (r_{stylus})	5 µm
Stylus´ cone angle	90°

Source: Adapted and based on (JENOPTIK; HOMMEL, 2008).

Based on such measuring settings, it was possible to evaluate the surface roughness by conducting 15 equidistant measurements along the periphery of the workpiece. Thus, each roughness measurement occurs at angular increments of 24° on the workpiece´s surface. By using the integrated software of the Nanoscan 855 the result of each roughness measurement comprehends a data set of specific roughness parameters which are selected before initializing the roughness measurements. In this way, the significant roughness parameters which have been evaluated during these measurements were: R_t, R_a, R_{sk}, R_z, R_{max}, R_{pk}, R_k, and R_{vk}. The representative value of the surface roughness corresponds to the mean value of all 15 measurements for each specific roughness parameter.

4.8 OPTICAL MEASURING SYSTEM FOR 3D SURFACE MEASUREMENTS

Measurements of the grinding wheel´s replicas (produced during the experiments related to the DPCM, Appendix B) have been carried out by using an optical measuring system for 3D surface measurements (company: Alicona, type: Infinite Focus IFM G4), Figure 38.

Its operating principle combines the small depth of focus of an optical system with vertical scanning to provide topographic and colourful information from the variation of focus. Specific developed algorithms combine this into a single 3D data set with accurate topographic information. Vertical resolutions can be as low as 10 nm making the measuring system ideal for surface study of both homogeneous and compound materials.

Figure 38 – Optical measuring system for 3D surface measurements.
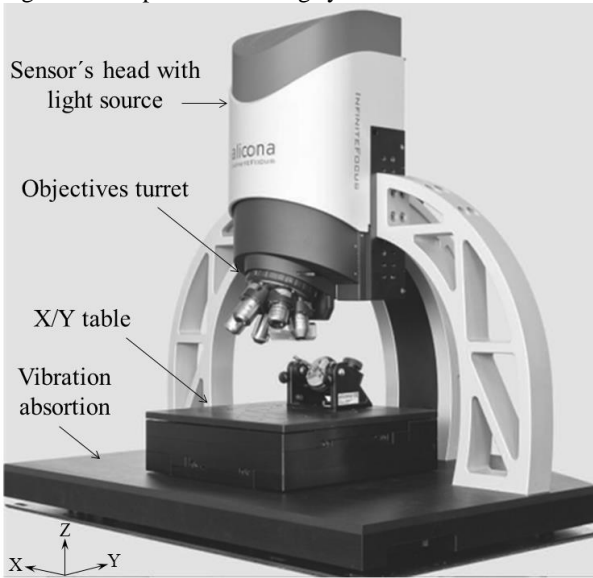
Source: Adapted and based on (ALICONA, 2009).

The range of measurable surfaces is almost unlimited, enabled by a LED ring light. The instrument can be used in both the laboratory and near production environment. Six objectives (2,5 x, 5 x, 10 x, 20 x, 50 x, and 100 x) allow magnifying the analyzed region on the specimen´s surface. The higher the magnification, the slower is the scanning vertical speed, which in turn can vary from 3000 μm/s (objective of 2,5 x) up to 1000 μm/s (objective of 100 x) (ALICONA, 2009, 2010).

4.8.1 Setup of the Optical Measuring System for 3D Surface Measurements on Grinding Wheel´s Replicas

Measurements of the positive replica of the grinding wheel´s topography have been characterized as 3D surface measurements. Each specimen was measured individually by placing and illuminating it onto the X/Y table with a modulated white light. The coaxial white light is provided by a light source on the sensor´s head and delivered through a beam splitter to the selectable objective (objective 5 x magnification), in the six-place turret of the optical measuring system. The specimen´s reflected light is projected through the beam splitter onto a color digital sensor. The selection of both the vertical and lateral resolution during

the measurements can be realized through a simple change of objectives and by means of the measuring software which accompanies the optical measuring system.

The resulting image is similar to conventional light microscopy in a manner that it shows limited depth of focus. As the distance between the specimen and the objective is varied, images are continuously captured. Each position in depth is differently imaged depending on the 3D structure of the specimen. The harmonized interaction between the modulated illumination, the vertical scanning and the sensor is decisive for this measuring process. This coordinated interaction is enabled by the optical measuring system. As a measuring result, a dense 3D surface representation of the specimen is obtained.

The operating principle of focus-variation has been added to the latest ISO standard for classifying surface texture methods. The new draft of ISO norm 25178 for the first time comprises standardized parameters to classify optically area-based measurements (ALICONA, 2009, 2010).

By using the mentioned objective (magnification of 5 x) it is possible to measure an area of 2,5 mm x 2 mm on the specimen´s surface. In order to get an average value related to the surface of the specimen, 4 distinct adjacent measurements in the central region of the specimen have been performed, so that for each specimen a total area of 5 mm x 4 mm (measuring area, $A_{rep}= 20$ mm^2) is evaluated. The result for each surface measurement is obtained by means of the surface parameter Smr(c) which characterizes the behaviour of the replica´s surface for a predefined height (c), also known as threshold, based on the analyzed surface (DIN EN ISO 25178-2, 2008). The parameter Smr(c) can be easily measured through the measuring software of the optical measuring system. Such surface parameter corresponds to a standardized parameter (according to the norm DIN EN ISO 25158) and permits to compute the percentage of points of the measured surface which lie above the predefined threshold (c). For all the imprint measurements, the predefined value of the threshold was set down to 2 µm in relation to the highest peak of the specimen´s surface. The definition of the highest peak of the specimen´s surface is detected by analyzing the Abbot-curve of the 3D measured data set with the help of the measuring software of the optical measuring system. Table 7 summarizes the main set parameters for measuring the grinding wheel´s replicas.

Table 7 – Settings for 3D surface measurements on grinding wheel´s replicas.

Measuring parameters	Selected values
Vertical resolution (V.R)	500 nm
Lateral resolution (L.R)	10 μm
Objective´s magnification	5 x
Measurements per specimen	4
Cut-off (λ_c)	570,2
Measuring region	central
Evaluation parameter	Smr (2 μm)

Source: Adapted and based on (ALICONA, 2010).

4.9 EXPERIMENTAL RIGS

In the scope of the present research, two experimental rigs have been designed and developed in order to allow conducting the scheduled experiments for both the DPCM and the DICM. This section describes the main characteristics of both experimental rigs.

4.9.1 Experimental Rig for Experiments concerning the Dynamic Post-process Characterization Method (DPCM)

The planned experiments with respect to the DPCM have been accomplished by means of a particular developed experimental rig composed of: a) one cylindrical CNC grinding machine (Company: Zema Zselics Ltda, type: Pratika Flexa 600-L, Section 4.1), b) one AE monitoring device, AE/MD-1 (Company: Sensis Ltda, Section 4.4.1); c) one data acquisition device, DAD-1; (Company: National Instruments, type: NI USB-6218, Section 4.6.1); and d) one laptop. The arrangement of the experimental rig and its principal devices as well as the working chamber of the grinding machine are schematically represented in Figure 39. Additionally, the signal chain/flow related to the Scratch Experiments (Figure 39, dashed lines) and to the AE Tactile Scanning Experiments (Figure 39, continuous lines) are also shown.

Figure 39 – Experimental rig designed for the experiments regarding the Dynamic Post-process Characterization Method (DPCM).
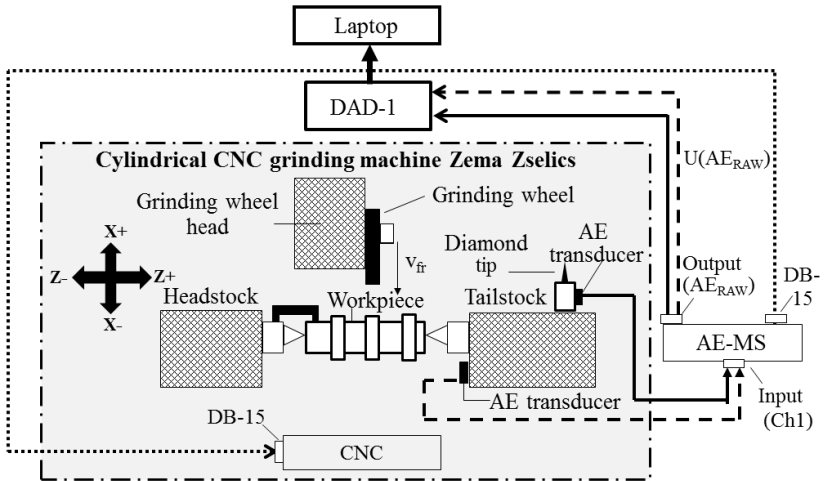
Source: (Developed by the author).

This experimental rig was employed for running both the Scratch Experiments and the AE Tactile Scanning Experiments in connection with the DPCM, (see Chapter 5). During the Scratch Experiments, the AE/MD-1 was used and its AE transducer has been mounted on the tailstock of the grinding machine for monitoring the grinding process. This position has presented the best signal to noise ratio for AE measurements during grinding. The AE events measured by the AE transducer are converted into the voltage domain and sent via coaxial cable to the AE-MS of the AE/MD-1, aiming at conditioning the analog voltage signal. Signal conditioning involves some important steps, as for example, signal amplification, noise reduction, signal band-pass filtering, and signal low-pass filtering. Next, the analog voltage signal is sent to the DAD-1 via a coaxial cable for signal digitization. The AE_{RAW} digitized signal is then transferred to a laptop (via USB cable) for on-line monitoring, data storage, and signal post-processing. The on-line monitoring and the post-processing of the digitized AE_{RAW} signal are carried out with the support of a computational algorithm (i.e., Algorithm-1) developed in Labview programming language (see Section 4.6.1.1).

In the course of the AE Tactile Scanning Experiments the AE/MD-1 has also been used for determining a precise reference position on the grinding wheel´s surface (BOARON, 2009). The

determination of such reference position is carried out through a specific developed contact recognition procedure (see Section 5.3.2.1) by integrating the AE-MS into the NC command of the grinding machine, (BOARON; WEINGAERTNER, 2012a). For such machine interfacing, the connection DB-15 in the rear panel of the AE-MS is used (Figure 39, dotted line). Throughout the AE Tactile Scanning Experiments, the AE transducer was mounted on the diamond tip´s support attached to the tailstock, Appendix C. This mounting position was the most suitable regarding the close proximity to the AE sources (interferences between the rotating grinding wheel and the diamond tip) as well as due to the good sensitivity of the AE signal. The acquired AE signals are sent to the AE-MS of the AE/MD-1 (via coaxial cable) and next to the DAD-1 (via coaxial cable) aiming at signal conditioning and digitization, respectively. The digitized AE_{RAW} signals are afterwards transferred to the laptop (via USB cable) for on-line monitoring, data storage, and signal post-processing. Both the on-line monitoring and the post-processing of the digitized AE_{RAW} signals are carried out by means of Algorithm-1 which is developed in Labview programming language (see Section 4.6.1.1).

4.9.2 Experimental Rig for Experiments concerning the Dynamic In-process Characterization Method (DICM)

The developed experimental rig for conducting the scheduled experiments regarding the DICM was composed of: a) one cylindrical CNC grinding machine (Company: Schaudt Mikrosa BWF GmbH, type: PF 51, Section 4.1), b) one AE monitoring device, AE/MD-2 (Company: Kistler Instrumente AG, Section 4.4.2), c) one cutting force monitoring device, Force/MD (Company: Kistler Instrumente AG, Section 4.5), d) one data acquisition device, DAD-2 (Company: National Instruments, Section 4.6.2), and e) one laptop. Figure 40 schematically shows the arrangement of this experimental rig, detaching its main devices, the grinding machine´s working chamber, and the connections between the used devices. The signal chain/flow related to the Scratch Experiments (Figure 40, dashed lines) and to the AE Tactile Scanning Experiments (Figure 40, continuous lines) are also shown.

Such experimental rig has been used during both the Scratch Experiments and the AE Tactile Scanning Experiments in the course of the DICM´s experiments, (see Chapter 5). When conducting the Scratch Experiments, the acquisition of the grinding cutting force signals was applied for monitoring the grinding process, by using the Force/MD.

Hence, it was necessary to install the Force/MD´s dynamometer in the spindle of the grinding machine´s headstock in advance to the experiments.

During the Scratch Experiments, the main components of the grinding cutting force (F_x, F_y, F_z, and M_z) are on-line measured by the dynamometer and then converted into the voltage domain and simultaneously sent via cable to the Force-MSC, in order to proceed the signal conditioning of the analog voltage signal.

Figure 40 – Experimental rig designed for the experiments regarding the Dynamic In-process Characterization Method (DICM).
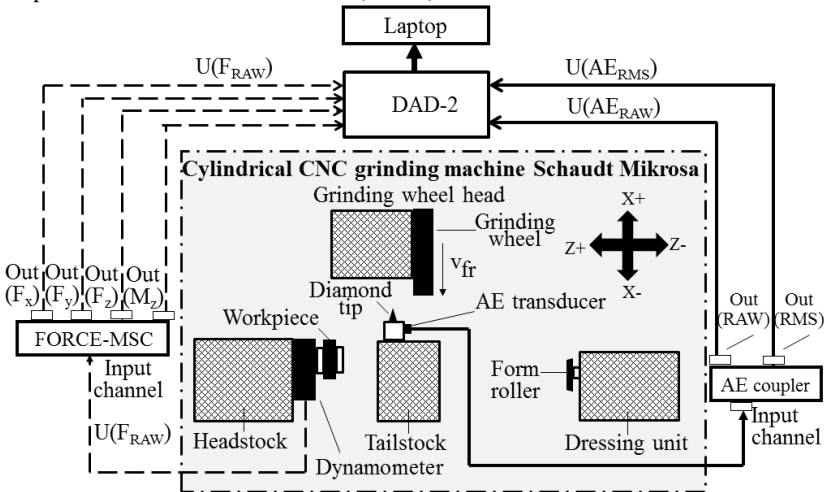
Source: (Developed by the author).

After conditioning the analog signal (through signal amplification and signal low-pass filtering), the output analog voltage signal is connected to the data acquisition device DAD-2, aiming at signal digitization. The digitized signals are transferred to a laptop via USB cable in order to storage and post-process the acquired signal by means of a developed computational algorithm (Labview programming language). By post-processing the digitized signals it is possible to evaluate both the normal cutting force (F_n) as well as the tangential cutting force (F_t) related to the grinding process (see Appendix D).

For the AE Tactile Scanning Experiments, the AE signals are acquired by means of an AE transducer which is mounted on the diamond tip´s support attached to the tailstock of the grinding machine, Appendix C. The AE_{RAW} signals are captured by the AE transducer and

sent to the AE coupler of the AE/MD-2 through appropriate cable for signal conditioning (i.e., amplification, band-pass filtering, low-pass filtering and RMS conversion). After signal conditioning, both the analog AE_{RAW} signal and the analog AE_{RMS} signal are transferred to the DAD-2 for signal sampling and digitization. The selection of the suitable sampling rates is carried out by means of Algorithm-2 (developed in Labview programming language, see Section 4.6.2.1.1) which is installed in the same laptop. Besides the on-line signal digitization, Algorithm-2 also allows additional signal processing analysis for the in-process characterization of the grinding wheel´s topography. The digitized signals are then sent to the laptop (via USB cable) aiming at signal monitoring, data storage and signal in-process evaluation.

4.10 GRINDING WHEEL DRESSING

The dressing process aims to define a pre-established topographic characteristic on the periphery of the investigated grinding wheels. This section describes the main dressing parameters which have been adopted for dressing the investigated grinding wheels during the experiments related to both the Dynamic Post-process Characterization Method (DPCM) and the Dynamic In-process Characterization Method (DICM).

4.10.1 Grinding Wheel Dressing during Experiments Related to the Dynamic Post-process Characterization Method (DPCM)

The dressing of the grinding wheel during the DPCM´s experiments has been carried out by employing a rotary dressing tool (form roller coated with diamond, company: Diamantwerkeuge Hameln), Table 8. Taking aim at avoiding dressing influences on the working results (e.g., workpiece roughness and form deviation), the dressing process is conducted inside the working chamber of the grinding machine by maintaining the grinding wheel mounted on its hub. One of the main purposes in dressing the grinding wheel was to afford a flat profile on the grinding wheels´ periphery. Table 8 shows the main technical specifications of the rotary form roller used for dressing the grinding wheel.

Table 8 – Specifications of the dressing tool used throughout the Dynamic Post-process Characterization Method (DPCM)´s experiments.

Technical Specifications of the dressing tool	
Manufacture specification	R140 IN2515 1100,8 6 40 10 TK D251 C150
Grain material	Diamond
Average grain size	251 µm
Coating width	6 mm
Profile	Flat
External diameter, d_r	110 mm
Active width, b_d	0,8 mm
Bond material	Ceramic-vitrified (sintered)
Base structure	Steel

Source: (Developed by the author).

The required flat profile on the grinding wheel´s surface has been achieved by defining the main dressing parameters. Hence, the dressing roller circumferential speed (v_R) was set to v_R= 17 m/s and its axial dressing feed rate (v_{fad}) evaluated as v_{fad}= 298 mm/min (v_{fad}= 5 mm/s). The grinding wheel circumferential speed during dressing (v_{sd}) has been set to v_{sd}= 30 m/s, (n_{sd}= 1488 rpm) which corresponded to the same value of the grinding wheel´s cutting velocity during grinding (v_s= 30 m/s). This led to a dressing speed ratio of q_d= -0,6 (up dressing), Equation 9.

$$q_d = \pm \frac{v_R}{v_{sd}} \tag{9}$$

The overlap ratio (U_d) was previously specified as U_d= 4, then conducting to an axial dressing feed per grinding wheel revolution (f_{ad}) equal to f_{ad}= 0,2 mm , Equation 10.

$$U_d = \frac{b_d}{f_{ad}} \tag{10}$$

The depth of dressing cut (a_{ed}) was constant and equal to a_{ed}= 10 µm for all the 5 required dressing passes. During the dressing process the AE signals are on-line monitored, thus permitting to infer the flatness of the grinding wheel´s surface.

4.10.2 Grinding Wheel Dressing during Experiments Related to the Dynamic In-process Characterization Method (DICM)

For dressing the grinding wheel a rotary dressing tool (form roller coated with diamond, company: Dr. Kaiser Diamantwerkzeuge GmbH) has been utilized over the DICM´s experiments. The dressing process took place inside the grinding machine in order to avoid dressing influences on the working results. Additionally, the dressing process of the grinding wheel has aimed at producing a flat profile on the grinding wheel´s periphery. Table 9 shows the main technical specifications of the rotary form roller used for dressing the grinding wheel.

Table 9 – Specifications of the dressing tool used throughout the Dynamic In-process Characterization Method (DICM)´s experiments.

Technical Specifications of the dressing tool	
Manufacture specification	RIG40-G60-120-0,6-6-50,8-12-TK
Grain material	Diamond
Profile	Flat
External diameter, d_r	120 mm
Active width, b_d	0,6 mm
Bond material	Nickel-based
Base structure	Steel

Source: (Developed by the author).

For dressing the grinding wheel, the dressing roller circumferential speed (v_R) was set to $v_R = 17$ m/s and its axial dressing feed rate (v_{fad}) was $v_{fad} = 720$ mm/min (12 mm/s). The grinding wheel circumferential speed during dressing (v_{sd}) was adjusted to the same value of its cutting velocity used during grinding (v_s), so that, $v_{sd} = v_s = 30$ m/s, thus resulting in a dressing speed ratio $q_d = -0,6$ (Equation 9) where the negative value refers to up dressing. By using an axial dressing feed per grinding wheel revolution (f_{ad}) equal to $f_{ad} = 0,6$ mm, and as $b_d = 0,6$ mm (active width of the dressing tool), the resulting overlap ratio is $U_d = 1$ (Equation 10). The depth of dressing cut (a_{ed}) was set to $a_{ed} = 20$ µm. Aiming at eliminating unwanted disturbances on the grinding wheel´s surface due to its utilization before the experiments, the dressing process is repeated 5 times (5 dressing passes). For each dressing pass, the on-line monitoring of the AE signals takes place, thus enabling to monitor the reached flatness of the grinding wheel.

5 METHODOLOGY AND EXPERIMENTAL PLANNING

This chapter presents the main methodological approaches and the experimental planning which have been adopted for accomplishing the previously described objectives related to this research. Additionally, a contribution is intended to improve the existing procedures for the characterization of conventional grinding wheels, by adding relevant information to that already available in the current related literature.

The implemented methodology comprises two complementarily experimental methods: a) Dynamic Post-process Characterization Method (DPCM); and b) Dynamic In-process Characterization Method (DICM). On the one hand, the DPCM aims at defining and validating a reliable AE-based procedure for characterizing the topography of a conventional grinding wheel after stopping the grinding process (i.e., post-process analysis).

On the other hand, the DICM has the main goal to define and validate a suitable AE-based quick test method (AE Quick Test Method) for the in-process characterization of the topography of a similar conventional grinding wheel. The in-process characterization of the grinding wheel´s topography by means of the proposed AE Quick Test Method consists in the great novelty and contribution of the current research. This is achieved by using appropriately signal processing techniques (based on those proposed and validated by the DPCM), which allow to obtain quantified in-process information related to the grinding wheel´s topography. The following sections explain both characterization methods and their particularities.

5.1 DYNAMIC POST-PROCESS CHARACTERIZATION METHOD (DPCM)

The DPCM relies on the existing methods for characterizing the topography of grinding wheels, Figure 41-a. Specific experiments are carried out (i.e., Scratch Experiments, Section 5.3.1, and AE Tactile Scanning Experiments, Section 5.3.2) in order to characterize the topography of the investigated grinding wheel, Figure 41-b. Both experiments involve the utilization of commonly employed grinding wheel velocities (v_s= 30 m/s), hence, the acquired AE_{RAW} signals in the course of the experiments contain useful information related to the grinding process kinematics and to the grinding wheel´s topography as well. The experiments are based on the on-line measurement of AE_{RAW}

signals (Figure 41-c). To characterize the grinding wheel´s topography, the acquired AE_{RAW} signals (from both the AE Tactile Scanning Experiments and the Scratch Experiments) are analyzed out of the grinding process (i.e., post-process analysis, Figure 41-d).

Figure 41 – Dynamic Post-process Characterization Method (DPCM).
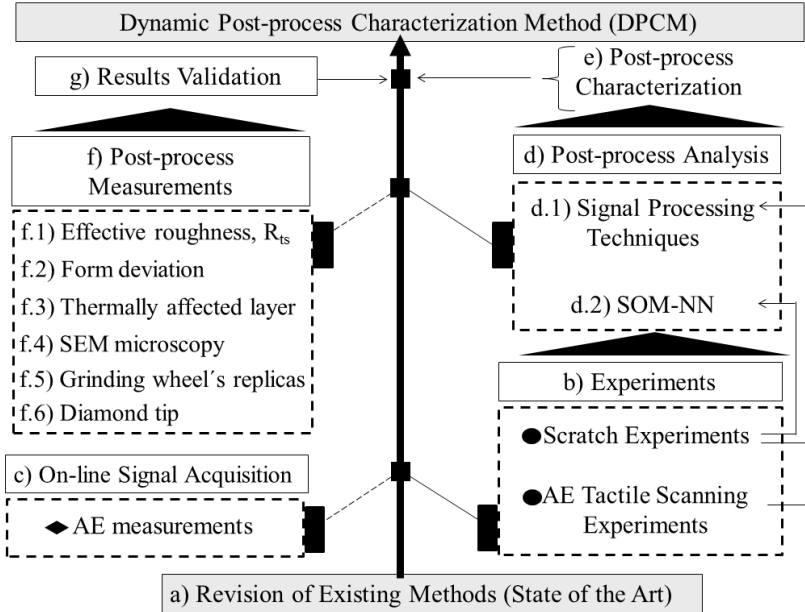
Source: (Developed by the author).

For the sake of extracting quantitative information from the grinding wheel´s topography, specific signal processing techniques are utilized in both the time and frequency domains (Figure 41-d.1). Aiming to gain additional information about the changes occurring on the topography of the grinding wheel, a further SOM-NN analysis is performed based on the AE_{RAW} signals derived from the Scratch Experiments (Figure 41-d.2). Such technique permits to cluster different states of the topography for a post-classification (BRAGA; CARVALHO; LUDERMIR, 2000; MEHROTRA; MOHAN; RANKA, 1996). The results derived from the signal processing techniques and the SOM-NN allow obtaining a post-process information which is directly associated with the grinding wheel´s topography, Figure 41-e. Additionally, the mentioned techniques permit to model the topography variation behavior of the conventional grinding wheel. The changes in the

grinding wheel´s topography are due to the inherent wear of the grinding wheel, which is purposely induced during the Scratch Experiments.

The DPCM is validated by measuring the grinding process results (Figure 41-f), both on the workpiece (Figure 41-f.1: surface roughness parameter R_{ts}; Figure 41-f.2: form deviation, Figure 41-f.3: thermally affected layer, and Figure 41-f.4: SEM microscopy) as well as on the grinding wheel´s replicas (Figure 41-f.5). In addition, the measurement of the diamond tip (used during the AE Tactile Scanning Experiments) is also evaluated, in order to infer occasional wear (Figure 41-f.6). These measuring results are afterwards correlated with the post-process information obtained from both the signal processing techniques and the SOM-NN in order to validate the results (Figure 41-g).

5.2 DYNAMIC IN-PROCESS CHARACTERIZATION METHOD (DICM)

The DICM relies on the signal processing techniques validated in the DPCM, Figure 42-a.

Figure 42 – Dynamic In-process Characterization Method (DICM).
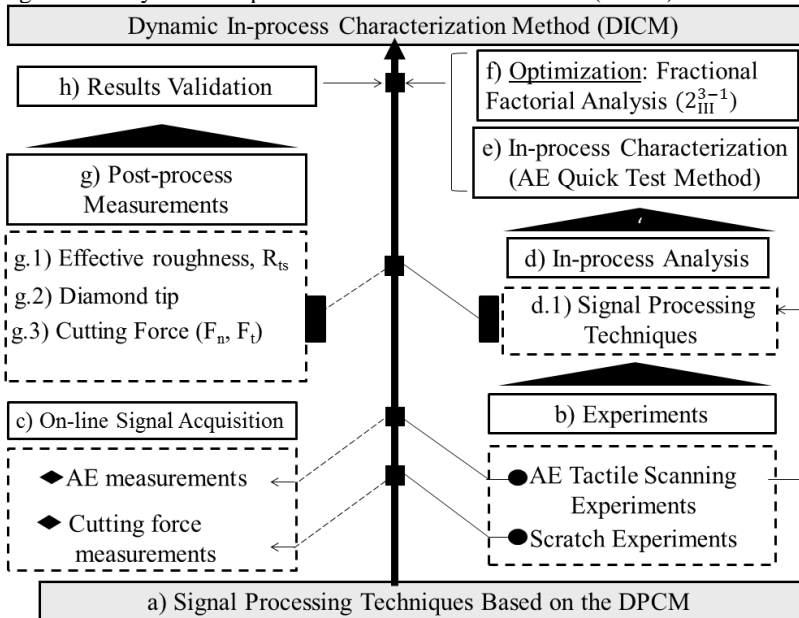
Source: (Developed by the author).

Similar planned experiments are carried out, Figure 42-b (i.e., Scratch Experiments, Section 5.3.1, and AE Tactile Scanning Experiments, Section 5.3.2), which involve the utilization of commonly used grinding cutting speeds (v_s= 30 m/s), thus representing a feasible information related to the grinding process. The experiments are based on a transducer-fusion technique. This technique employs the on-line acquisition of both AE signals (during the AE Tactile Scanning Experiments) and the grinding cutting force signals (during the Scratch Experiments) in order to obtain reliable information about the grinding wheel´s topography (Figure 42-c). The evaluation of the AE signals related to the AE Tactile Scanning Experiments is performed in-process (Figure 42-d) by employing the proposed signal processing techniques validated earlier (Figure 42-d.1). This allows obtaining in-process quantified information regarding the topography of the grinding wheel, thus consisting in the AE Quick Test Method proposed in this research (Figure 42-e).

In order to optimize the quantified information obtained through the AE Quick Test Method, a further 2_{III}^{3-1} Fractional Factorial Analysis is carried out, by using the time domain outputs derived from the AE Quick Test Method (i.e., in-process quantified information). Such analysis allows achieving an empirical model which takes into account the main influencing factors that present significant effect on the time domain response of the AE Quick Test Method (Figure 42-f).

The DICM is validated by conducting specific post-process measurements (Figure 42-g), on the ground workpieces (i.e., surface roughness, parameter R_{ts}, Figure 42-g.1), and on the diamond tip (Figure 42-g.2). Additionally, the post-process analysis of the grinding cutting force components (F_n and F_t) is also implemented (Figure 42-g.3). The measuring results and the post-process analysis of the grinding cutting force components are correlated with the in-process quantitative information associated with the topography of the grinding wheel in order to validate the results (Figure 42-h).

5.3 EXPERIMENTAL PROCEDURES TO CHARACTERIZE THE TOPOGRAPHY OF CONVENTIONAL GRINDING WHEELS

The experiments to characterize the topography of conventional grinding wheels are based on two distinct experimental procedures: a) Scratch Experiments; and b) AE Tactile Scanning Experiments. Both experimental procedures provide complementary information about the

topography of the grinding wheel and are detailed in the following sections (see Section 5.3.1 and Section 5.3.2).

5.3.1 Scratch Experiments

In the Scratch Experiments, the topography of the grinding wheel is imprinted onto the surface of a workpiece. These experiments aim at to obtain information about the topography of the grinding wheel by measuring the effective roughness of the grinding wheel, R_{ts}. During the Scratch Experiments, the workpiece is plunged ground until it reaches a predefined diameter. After reaching the predefined diameter, the grinding wheel reverses its infeed movement without spark-out time. Therefore, the ground surface presents a roughness related to the specific material removal rate (Q'_w) used during the experiment. Simultaneously to plunge grinding, the grinding process characteristics are on-line measured. When conducting the Scratch Experiments regarding the DPCM, the AE signals derived from the grinding process are on-line measured by means of the experimental rig 1 (Section 4.9.1). During the Scratch Experiments valid for the DICM, only the grinding cutting force signals are on-line acquired and monitored by using the experimental rig 2 (see Section 4.9.2).

The evaluation of the grinding wheel´s effective roughness R_{ts} is determined by measuring the roughness of the workpiece derived from the plunge grinding process with a rotational ratio (q) between the grinding wheel and the workpiece (KÖNIG, 1989). During the Scratch Experiments related to both characterization methods (i.e., DPCM and the DICM), two similar rotational ratios have been used, Table 10. For the proposed rotational ratio of q= 1:5 (one complete rotation of the grinding wheel for each 1/5 rotation of the workpiece) the grinding wheel´s periphery is represented five times over the periphery of the workpiece. By measuring the workpiece´s roughness in different angular positions incremented by 24°, it is possible to achieve average information about the topographic characteristic of the grinding wheel. Table 10 summarizes the main parameters which were employed during the Scratch Experiments for both characterization methods (i.e., DPCM and the DICM).

Table 10 – Parameters employed during the Scratch Experiments.

Parameters	Characterizaton Methods	
	DPCM	DICM
Q'_w	$6 \text{ mm}^3/\text{mm.s}$	$6 \text{ mm}^3/\text{mm.s}$; $12 \text{ mm}^3/\text{mm.s}$
$d_{w,initial}$	60 mm	88,5 mm
$d_{w,final}$	32 mm	87 mm
v_s	30 m/s	30 m/s
q	1:6	1:5
L_{eff}	15 mm	25 mm
V'_w	$50 \text{ mm}^3/\text{mm}$	$40 \text{ mm}^3/\text{mm}$
$V'_{w, total}$	$2000 \text{ mm}^3/\text{mm}$	$200 \text{ mm}^3/\text{mm}$
Direction	(-) up grinding	(-) up grinding
Workpiece material	Nodular cast iron	Steel alloy (100Cr6)
Workpiece hardness	237 HV	860 HV
On-line Measurement	AE (800 Hz up to 50 kHz)	Force

Source: (Developed by the author).

5.3.2 Acoustic Emission (AE) Tactile Scanning Experiments

The AE Tactile Scanning Experiments consist in contact scanning the topography of the grinding wheel by using a diamond tip (i.e., single-point diamond tip). The interferences between the grinding wheel´s kinematic cutting edges and the diamond tip proceed in the realm of a few micrometers (elastic deformation range) and are on-line recognized by means of an AE transducer.

The AE Tactile Scanning Experiments comprehend two main stages: Stage-A) Determination of the reference position on the grinding wheel´s periphery (Figure 43-a), (see also Section 5.3.2.1 and Section 5.3.2.2), which serves as reference for the following stage; Stage-B) Acquisition and evaluation of the AE_{RAW} signals derived from the interferences between the grinding wheel´s kinematic cutting edges and the diamond tip in the elastic deformation range (Figure 43-b.1 and Figure 43-b.2), (see also Section 5.3.2.3). Two distinct scanning trajectories between the grinding wheel and the diamond tip are investigated aiming at characterizing the topography of the grinding wheel: b.1) Tangential AE Tactile Scanning, (Figure 43-b.1), and; b.2) Axial AE Tactile Scanning, (Figure 43-b.2). The following sections

describe in more details the particularities of both Stage-A and Stage-B during the AE Tactile Scanning Experiments valid for the DPCM and the DICM.

Figure 43 – AE Tactile Scanning Experiments.

Stage-A: Determination of the Reference Position

a) AE Contact Recognition:

Stage-B: Acquisition and Evaluation of the AE_{RAW} Signals

b.1) Tangential AE Tactile Scanning   b.2) Axial AE Tactile Scanning
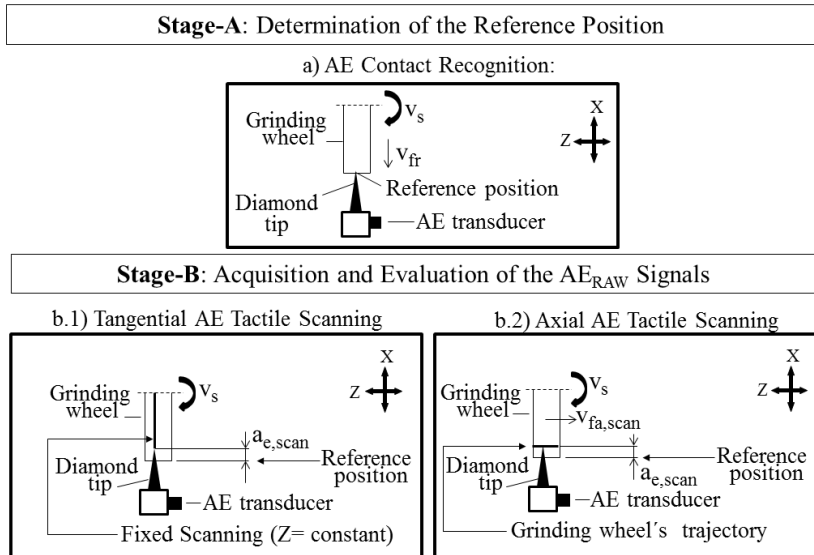
Source: (Developed by the author).

5.3.2.1 Determination of the reference position on the grinding wheel´s surface (during experiments regarding the dynamic post-process characterization method - DPCM)

During the AE Tactile Scanning Experiments regarding the DPCM, the reference position on the grinding wheel´s periphery is determined by means of an automatized contact recognition procedure. This procedure is carried out by firstly integrating the AE/MD-1 into the NC command of the grinding machine (see Section 4.9.1) (BOARON, 2009; BOARON; WEINGAERTNER, 2012a).

At the beginning of the contact recognition procedure the grinding wheel is positioned 250 mm from the diamond tip ($X^+ = 250$), Figure 44. Next, the grinding wheel is set to $v_s = 30$ m/s and guided towards the diamond tip by using an infeed velocity $v_{fr1} = 6000$ mm/min until a specific position situated at 0,5 mm away from the diamond tip (Figure 44, point 1). After reaching this position, the infeed velocity is changed

to an approximation value v_{fr2}, until the first contact can be recognized by the AE/MD-1 (Figure 44, point 2).

Figure 44 – Contact recognition procedure during experiments regarding the Dynamic Post-process Characterization Method (DPCM).
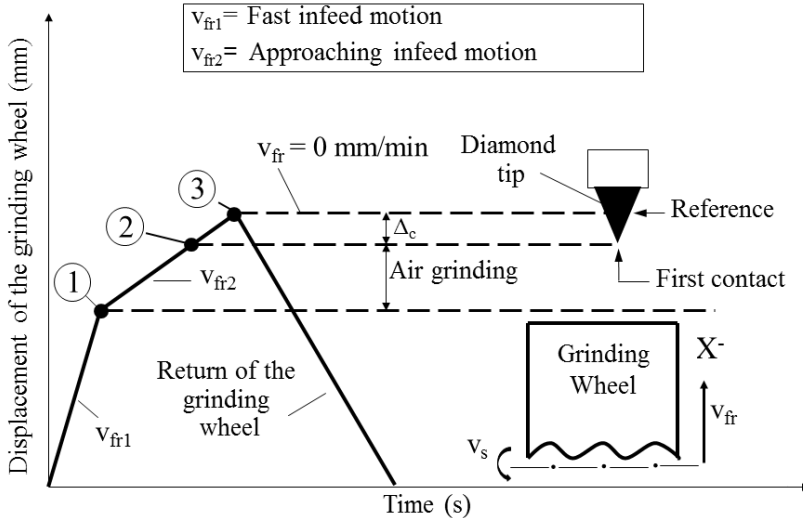
Source: (Developed by the author).

The first contact recognition by the AE/MD-1 (which is integrated into the NC command of the grinding machine) simultaneously stops the infeed movement of the grinding wheel´s head. This action additionally leads to a minimum displacement (interference depth, Δ_c) towards the diamond tip and is a direct function of the infeed motion of the grinding wheel v_{fr2}, the time-response by the installed AE/MD-1 as well as the elastic behavior of the mechanical system composed of the grinding machine, the diamond tip, and the grinding wheel. Therefore, the real contact recognition position occurs when $v_{fr}= 0$ mm/min (Figure 44, point 3). The coordinates (X and Z) associated with the contact recognition position are then stored in the NC command of the grinding machine and used as reference for the next stage (Stage-B). After the contact recognition and the stoppage of the infeed motion, the grinding wheel is moved away until it reaches a secure distance.

Previous studies in the same grinding machine have shown that interferences down to $\Delta_c= 1$ µm (during the contact recognition procedure) can be achieved when using infeed velocities in the range of $v_{fr2}= 0{,}1$ mm/min up to $v_{fr2}= 0{,}5$ mm/min, (BOARON, 2009; BOARON;

WEINGAERTNER, 2012a). Therefore, it is possible to conduct the evaluation of the topography of the grinding wheel by using interferences down to 1 μm and within the elastic deformation range of the grinding wheel and the diamond tip, without removing grains from the grinding wheel´s surface nor wearing the diamond tip. Besides the possibility of assuring the integrity of both the grinding wheel and the diamond tip, the contact recognition procedure is not time-consuming when compared with the commonly used manual methods and affords good precision. Such procedure has been already applied in industry for the optimization of the setup time in a grinding machine (BOARON, 2009; BOARON; WEINGAERTNER; MARTINENGUI, 2011; BOARON; WEINGAERTNER, 2012a).

5.3.2.2 Determination of the reference position on the grinding wheel´s surface (during experiments regarding the dynamic in-process characterization method - DICM)

During the AE Tactile Scanning Experiments concerning the DICM, the reference position on the grinding wheel´s periphery involves two distinct steps: The first step consists in finding the initial contact between the grinding wheel and the diamond tip by manually rotating the grinding wheel ($v_s \approx$ 5 m/s) and, at the same time, by slowly infeed moving it ($v_{fr} \approx$ 2 mm/min) against the diamond tip. The infeed movement of the grinding wheel is also manually controlled. During the movement of the grinding wheel against the diamond tip, the AE_{RAW} signals are on-line monitored. When the first contact occurs, a burst-like AE_{RAW} signal is visualized on the laptop´s screen, and the infeed movement is manually stopped. The X coordinate (i.e., X_1) is saved for the second step.

In the second step, the grinding wheel is set to rotate with the same cutting speed used for grinding the workpiece (v_s= 30 m/s). The grinding wheel moves against the diamond tip down to X_2= X_1 + 0,06 mm (allowance distance). After reaching X_2, the first contact is found by infeed moving the grinding wheel with stepwise increments of 1 μm and by simultaneously observing the AE_{RAW} signals in the laptop´s screen. The increments are commanded manually by the operator until the first contact (AE_{RAW} burst-like signal) is found (coordinate X_3) which is stored in the NC command of the grinding machine and serves as reference for the increments used at Stage-B.

5.3.2.3 Acquisition and evaluation of the AE_{RAW} signals (during experiments regarding both the DPCM and the DICM)

All the relative movements between the grinding wheel and the diamond tip at Stage-B are NC controlled. After defining the reference position on the grinding wheel´s periphery (as proposed at Stage-A, see Section 5.3.2.1 and Section 5.3.2.2), the grinding wheel is set to $v_s = 30$ m/s.

Next, the grinding wheel is positioned in the same Z coordinate which has been previously adopted for determining the reference position on the grinding wheel´s periphery. The grinding wheel is then guided towards the allowance distance from the diamond tip (i.e., point 1, Section 5.3.2.1; coordinate X_2, Section 5.3.2.2) with a fast infeed movement in the X^- direction while maintaining the same Z coordinate during this movement (Z= constant).

Next, the infeed velocity is decreased to the approach velocity ($v_{fr,approach}$) and the grinding wheel moves slowly against the diamond tip down to a predefined scanning depth ($a_{e,scan}$). The $a_{e,scan}$ is based on the reference position which was found at Stage-A. Such interference situates in the elastic deformation range of the grinding wheel and therefore does not alter the topography of the grinding wheel during the experiments.

After reaching $a_{e,scan}$, the grinding wheel stops its infeed movement and depending on the scanning trajectory being evaluated, it moves either parallel to the grinding wheel´s axis (i.e., axial scanning trajectory) or stays fixed in a constant Z coordinate (i.e., tangential scanning trajectory).

When employing the axial scanning trajectory, the grinding wheel moves linearly along a predefined scanning length (L_{scan}) through a constant axial scanning velocity ($v_{fa,scan}$) and constant scanning depth ($a_{e,scan}$). The AE_{RAW} signals originated in such interference conditions present the duration of t_{scan} and are recognized by the AE transducer.

On the other hand, when using the tangential scanning trajectory, the grinding wheel remains static in a constant Z coordinate while scanning the grinding wheel´s topography with a constant scanning depth ($a_{e,scan}$) during t_{scan} (WEINGAERTNER; BOARON, 2012b; WEINGAERTNER; BOARON, 2011). Table 11 and Table 12 summarize the main parameters which have been adopted during the AE Tactile Scanning Experiments regarding the DPCM and the DICM, respectively.

Table 11 – Parameters employed during the AE Tactile Scanning Experiments regarding the Dynamic Post-process Characterization Method (DPCM).

Parameters	Scanning Trajectories	
	Tangential	Axial
L_{scan}	0 mm	10 mm
$v_{fa,scan}$	0 mm/min	25 mm/min
$v_{fr,approach}$	0,25 mm/min	0,25 mm/min
v_s	30 m/s	30 m/s
$a_{e,scan}$	2 µm	1 µm
t_{scan}	10 s	24 s
R_{tip}	400 µm	400 µm

Source: (Developed by the author).

Table 12 – Parameters employed during the AE Tactile Scanning Experiments regarding the Dynamic In-process Characterization Method (DICM).

Parameters	Scanning Trajectories	
	Tangential	Axial
L_{scan}	0 mm	10 mm
$v_{fa,scan}$	0 mm/min	120 mm/min
$v_{fr,approach}$	0,5 mm/min	0,5 mm/min
v_s	30 m/s	30 m/s
$a_{e,scan}$	2 µm	1 µm
t_{scan}	5 s	5 s
R_{tip}	330 µm	330 µm

Source: (Developed by the author).

      Subsequently to the AE_{RAW} acquisition, the grinding wheel moves backwards to the safe distance from the diamond tip. Then, based on the AE_{RAW} signal which is acquired during t_{scan}, the developed computational algorithms evaluate a signal processing analysis for characterizing the grinding wheel´s topography. This is carried out by using specific signal processing techniques in both the time and frequency domains. The outputs from both the time and frequency domain analyses allow obtaining quantitative information directly related to the grinding wheel´s topography.

      In the DPCM, the computational algorithm´s output is evaluated out of the grinding process (i.e., post-process analysis) and is based on both a time and frequency domain analysis.

      In the time domain analysis, two different signal conditioning parameters are considered: a) AE_{RAW} oversteps (N), and b) Standard Deviation (σ_x), Figure 45. Figure 45-a displays a typical AE_{RAW} signal

obtained during the AE Tactile Scanning Experiments by employing the tangential trajectory. Figure 45-b shows a common AE_{RAW} signal derived from the axial scanning trajectory. Both figures graphically exemplify the parameters N and σ_x which are defined in the time domain.

Figure 45 – AE_{RAW} signals and time domain parameters regarding the Dynamic Post-process Characterization Method (DPCM).
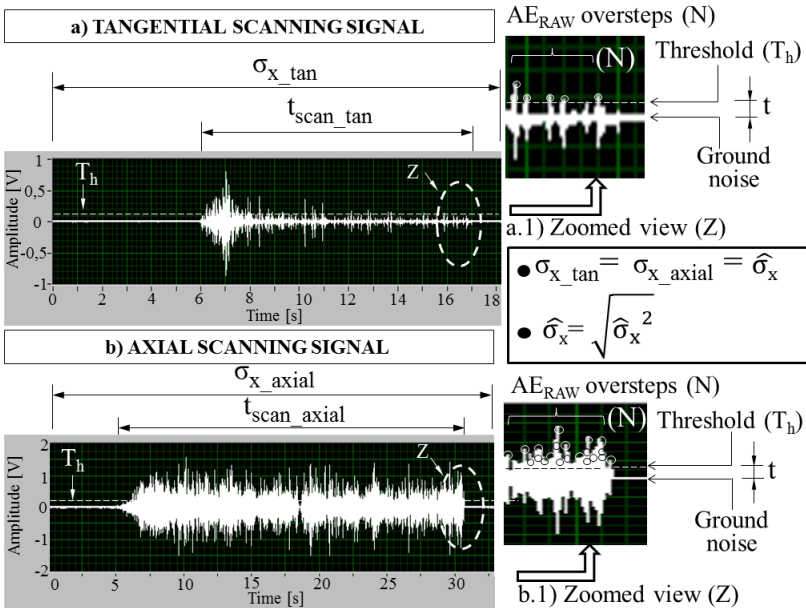
Source: (Developed by the author).

The first time domain parameter features the total amount of points (N) in the digitized AE_{RAW} signal which overstep a fixed predefined threshold (T_h) during t_{scan}. The predefined T_h lies above the maximum value of the AE_{RAW}´s ground noise signal, (gap distance t= 0,03 V) in order to not be influenced by occasional disturbances in the AE_{RAW} signal, and also to allow expressing useful information about the grinding wheel´s topography (Figure 45-a.1 and Figure 45-b.1). The time-domain parameter σ_x represents the standard deviation of the entire time history of the AE_{RAW} signal, and expresses the spread of the digitized AE_{RAW} signal during t_{scan}. Additionally, for a "zero" mean AE_{RAW} signal, σ_x also denotes the RMS level (root mean square) related

to the full time history of the signal, during t_{scan} (SHIN; HAMMOND, 2008).

On the other hand, the output from the frequency domain analysis consists in a chart which shows the evaluation of the AE Power Spectrum Density (PSD) based on the digitized AE_{RAW} signal. This chart allows obtaining complementary information about the changes on the grinding wheel´s topography by means of the AE_{RAW} spectrum´s distribution and the AE_{RAW} spectrum´s magnitude (i.e., RMS level). The assessment of the AE_{RAW} Power Spectrum Density (PSD) is evaluated in the range from 800 Hz up to 100 kHz.

In the DICM, the computational algorithm´s output is evaluated and obtained in-process, and instantaneously visualized on the laptop´s screen (when pushing the "stop" button of the signal acquisition program) immediately after finishing the AE Tactile Scanning Experiment. This is achieved with the same grinding setup and without the need to decelerate the grinding wheel´s velocity (v_s= 30 m/s). The computational algorithm´s output is derived from both a time and frequency domain analysis (BOARON; WEINGAERTNER; UHLMANN, 2014).

In the time domain analysis, the computational algorithm´s output is represented by the parameters N (AE oversteps) and the parameter σ_x (Standard Deviation), Figure 46. Figure 46-a shows a characteristic AE_{RAW} signal acquired during the AE Tactile Scanning Experiments when employing the tangential trajectory. Figure 46-b displays a representative AE_{RAW} signal derived from the axial scanning trajectory. Both figures graphically illustrate the parameters N and σ_x which are defined in the time domain.

Figure 46 – AE$_{RAW}$ signals and time domain parameters regarding the Dynamic In-process Characterization Method (DICM).
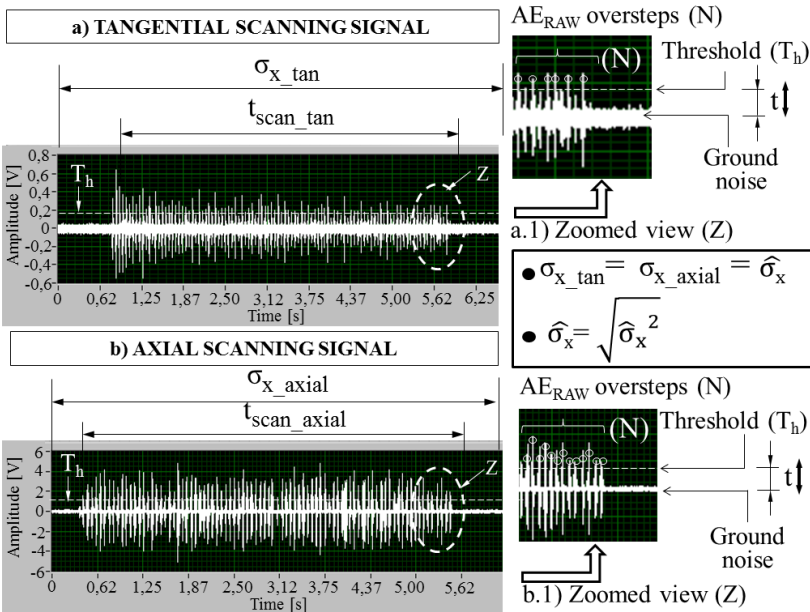
Source: (Developed by the author).

The parameter AE$_{RAW}$ oversteps (N) represents the total amount of points in the digitized AE$_{RAW}$ signal which overstep a predefined threshold (T$_h$) during t$_{scan}$, (e.g., Figure 46-a.1 and Figure 46-b.1). The predefined T$_h$ is set above the AE$_{RAW}$´s ground noise signal (gap distance "t"), and it varies in the course of the experiments as described in Section 5.5.1. The time-domain parameter σ$_x$ represents the standard deviation of the entire time history of the AE$_{RAW}$ signal, as previously defined by the DPCM.

The output derived from the frequency domain analysis comprises the assessment of the AE$_{RAW}$ Power Spectral Density (PSD) for the bandwidths under investigation B1 (5 kHz up to 100 kHz) and B2 (5 kHz up to 200 kHz), (see Section 4.4.2.1). This is achieved by investigating both the dispersion of the AE$_{RAW}$ spectrum and its evaluated magnitude (i.e., RMS level), which expresses a measure of the power (or energy) contained in the AE$_{RAW}$ signal.

5.4 EXPERIMENTAL PLANNING FOR EXPERIMENTS REGARDING THE DYNAMIC POST-PROCESS CHARACTERIZATION METHOD (DPCM)

The experiments related to the DPCM have been planned as represented in Figure 47. The arrows illustrate the progress of the experiment series over time. The experiments are divided into two main experiment series: a) first experiment series (Figure 47, white arrow) and second experiment series (Figure 47, black arrows).

In order to provide a flat initial topography on the grinding wheel´s surface, the first experiment series begins by initially dressing the grinding wheel (Figure 47, D1) as described in Section 4.10.1. After dressing the grinding wheel (A.D), the evaluation of the initial condition of the grinding wheel´s topography is estimated by means of the AE Tactile Scanning Experiments, (Figure 47, AE-Scan, A.D).

Figure 47 – Experimental planning for the Dynamic Post-process Characterization Method (DPCM).
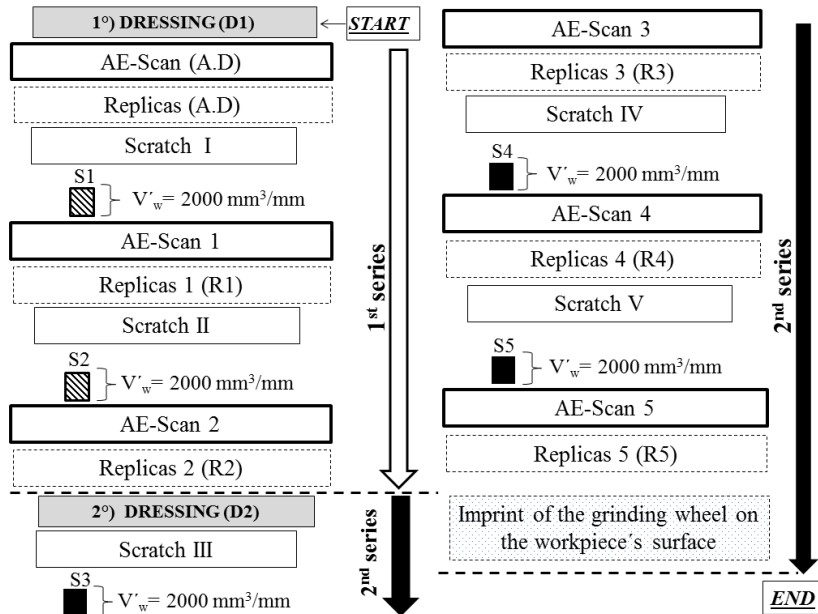
Source: (Developed by the author).

Next, the grinding wheel is kept static and two replicas are extracted from two opposite diametric positions in the grinding wheel´s

surface (Figure 47, Replicas A.D). The extraction of the grinding wheel´s replicas aims to obtain additional information related to the grinding wheel´s topography, (see Section 4.8.1 and Appendix B).

In order to purposely wear the grinding wheel, the Scratch Experiments begin (Figure 47, Scratch I) by plunge cylindrical grinding the first surface of the workpiece (S1), in which a total specific material removal of $V´_w= 2000$ mm^3/mm is machined. Aiming to evaluate the changes in the grinding wheel´s topography, both the AE Tactile Scanning Experiments (Figure 47, AE-Scan 1) and the extraction of the grinding wheel´s replicas (Figure 47, R1) are carried out. In order to considerably change the grinding wheel´s topography, the second surface of the workpiece (S2) is ground by means of the Scratch Experiment (Figure 47, Scratch II) without intermediary dressing of the grinding wheel. Next, the AE Tactile Scanning Experiments (Figure 47, AE-Scan 2) and the extraction of the grinding wheel´s replicas (Figure 47, R2) are conducted in this sequence for the sake of getting information about the changes taking effect in the topography of the grinding wheel. Such changes are associated with a total specific material removal of $V´_w= 4000$ mm^3/mm at the end of the first experiment series.

The second experiment series begins by dressing the grinding wheel with the same dressing parameters used in the first experiment series (Figure 47, D2). Over time, the amount of material ground in the workpiece is purposely increased aiming at wearing the grinding wheel. This is carried out by conducting sequential Scratch Experiments (Figure 47, Scratch III, IV, and V) on the surfaces S3, S4, and S5, respectively, thus leading to the total specific material removal $V´_w= 6000$ mm^3/mm at the end of the second experiment series. In the same way as in the first experiment series, the AE Tactile Scanning Experiments (Figure 47, AE-Scan 3, AE-Scan 4, and AE-Scan 5) and the extraction of the grinding wheel´s replicas (Figure 47, R3, R4, and R5) are carried out both between the Scratch Experiments and at the end of the second experiment series in order to characterize the induced wear on the grinding wheel´s topography. The second experiment series finishes by imprinting the grinding wheel onto the workpiece´s surface, aiming at estimating the radial wear of the grinding wheel. Such measurements are implemented out of the grinding process as mentioned in Section 4.7.1. In the course of imprinting, the grinding wheel is set to rotate ($v_s= 30$ m/s) and slowly plunges into the rotating workpiece until it reaches the imprinting depth $a_{e,imprint}= 0,8$ mm, by using a radial infeed $v_{fr}= 5$ mm/min. The impression generates a form

deviation on the workpiece´s surface which reflects the radial wear of the grinding wheel.

5.5 EXPERIMENTAL PLANNING FOR EXPERIMENTS REGARDING THE DYNAMIC IN-PROCESS CHARACTERIZATION METHOD (DICM)

The experiments related to the DICM have been planned as detached in Figure 48. The arrows illustrate the progress of the experiment series over time.

Figure 48 – Experimental planning for the Dynamic In-process Characterization Method (DICM).
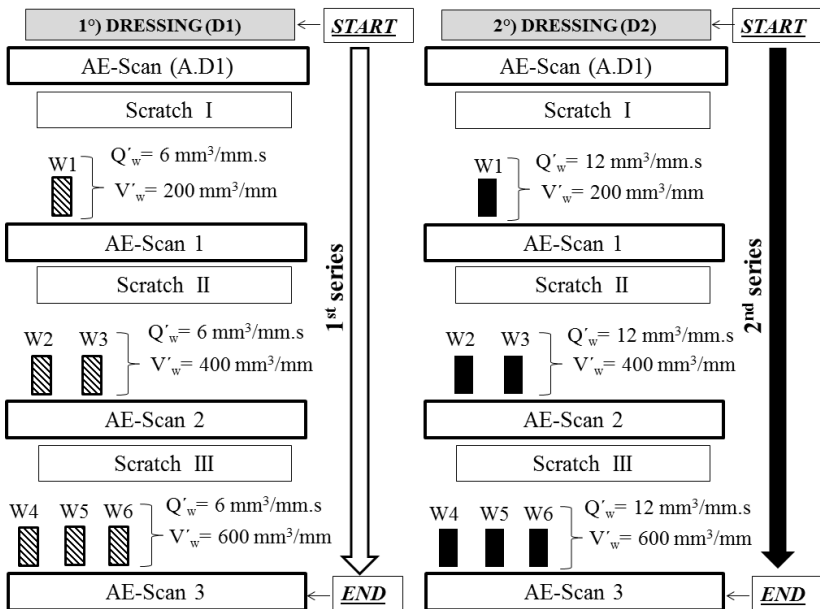
Source: (Developed by the author).

The experiments are divided into two main experiment series: a) first experiment series (Figure 48, white arrow) and second experiment series (Figure 48, black arrow). The first experiment series begins by dressing the grinding wheel (Figure 48, D1) aiming at affording a flat initial topography on the grinding wheel´s surface, as described in Section 4.10.2.

After dressing the grinding wheel (A.D), the AE Tactile Scanning Experiments are carried out in order to assess the initial condition of the grinding wheel´s topography (Figure 48, AE-Scan, A.D1). Next, the Scratch Experiments take place (Figure 48, Scratch I, $Q´_w$= 6 mm^3/mm.s) by plunge cylindrical grinding the first workpiece (W1), in which a total specific material removal of $V´_w$= 200 mm^3/mm is ground.

Over time, the total specific material removal ($V´_w$) progressively increases aiming to wear the grinding wheel. This is achieved by progressively increasing the amount of workpieces which are ground in the following Scratch Experiments (Figure 48, Scratch II, and Scratch III) while maintaining the same constant specific material removal ground per workpiece ($V´_w$= 200 mm^3/mm) and the same specific material removal rate ($Q´_w$= 6 mm^3/mm.s). This leads to the overall specific material removal $V´_w$= 1200 mm^3/mm at the end of the first experiment series. For the sake of characterizing in-process the changes in the grinding wheel´s topography, the AE Tactile Scanning Experiments are carried out both between the Scratch Experiments and at the end of the first experiment series (Figure 48, AE-Scan 1, AE-Scan 2, and AE-Scan 3)

In the second experiment series, the wear behaviour of the grinding wheel´s topography is investigated for the specific material removal rate of $Q´_w$= 12 mm^3/mm.s. The other grinding input parameters are kept equal to the previously described experiments. Next, the grinding wheel is dressed with the same dressing parameters used previously (Figure 48, D2). In the same way as in the first experiment series, from the very beginning of the experiment series until the end, the amount of $V´_w$ gradually increases in order to intentionally wear the grinding wheel and to change its topography. This is achieved by means of the Scratch Experiments (Figure 48, Scratch I, II, and III). The AE Tactile Scanning Experiments are carried out both between the Scratch Experiments and at the end of the second experiment series, in order to in-process characterizing the induced wear on the grinding wheel´s topography (Figure 48, AE-Scan 1, AE-Scan 2, and AE-Scan 3).

5.5.1 Experimental Planning for the AE Tactile Scanning Experiments regarding the Dynamic In-process Characterization Method (DICM)

The experimental planning for the AE Tactile Scanning Experiments regarding the DICM has been based on a 2^{k-1} Fractional Factorial Design. In comparison with a full Factorial Design (2^k), this experimental design requires that only half of the experimental runs be

investigated during the experiments (MONTGOMERY, 2001). Therefore, the 2^{k-1} Fractional Factorial Design was considered suitable to be implemented in the scope of the present research in terms of the available resources for conducting the experiments, as for example, machine available time and personal support. The definition of the experimental runs for the AE Tactile Scanning Experiments relies primarily on the influencing factors which directly affect the time-domain response of the AE Quick Test Method. The considered response in this case consists in the AE oversteps (i.e., parameter N).

   Among the influencing factors that exert direct impact on N, the value of the threshold (T_h), the type of the AE signal (T.S), and the sampling rate (f_s), are considered the most significant factors. These 3 factors were varied into 2 levels (high ↑, and low ↓) thus leading to a 2^{3-1}_{III} Fractional Factorial Design. The combinations of the factors and their levels of variation afford 4 distinct experimental runs, which have been investigated during the AE Tactile Scanning Experiments, for either scanning trajectories (i.e., tangential and axial scanning trajectories), Table 13.

   The first row of Table 13 illustrates the experimental run "a" in which the factor "Type of Signal" (T.S) is set to its high level (i.e., AE_{RAW} signal) whereas both the factor "Sampling rate" (f_s) and the factor "Threshold" (T_h), are set to their lower levels (i.e., 200 kS/s, and minimal voltage threshold, respectively). Each experimental run shown in Table 13 has been repeated 3 times in order to get an average representative value along the experiments, so that, for each scanning trajectory, a total of 12 replicates of N are obtained during the AE Tactile Scanning Experiments.

Table 13 – Experimental runs for AE Tactile Scanning Experiments regarding the Dynamic In-process Characterization Method (DICM).

Experimental runs	Type of Signal (T.S)	Sampling rate (f_s)	Threshold (T_h)
	↑= AE_{RAW} ↓= AE_{RMS}	↑= 400 kS/s ↓= 200 kS/s	↑= high (V) ↓= low (V)
a	↑	↓	↓
b	↓	↑	↓
c	↓	↓	↑
abc	↑	↑	↑

Source: (Developed by the author).

Consequently, a total of 48 replicates of N are obtained at the end of the scheduled AE Tactile Scanning Experiments (bottom line in Figure 48, i.e., AE-Scan 3), for each individual scanning trajectory. The set levels of the factor "Threshold" (T_h) depend heavily on the type of the AE signal (either AE_{RAW} or AE_{RMS}) as well as on the ground noise of the AE signals. In order to avoid that occasional disturbances in the AE signal erroneously overstep the selected T_h value, both the low ($\downarrow$) and the high ($\uparrow$) levels of T_h lie above the maximum value of the AE signal´s ground noise. Therefore, casual drifts in the AE signal due to signal disturbances do not affect the proposed procedure over the experiment series.

Either levels of the factor T_h are evaluated based on the prior calculation of both the RMS value of the AE signal´s ground noise, $(AE_{RMS})_{ground\ noise}$, and the standard deviation of the AE signal´s ground noise, $(\sigma_{ground\ noise})$. Equation 11 and Equation 12 show the evaluation of the low ($\downarrow$) and the high ($\uparrow$) levels of the factor T_h, respectively, when running the AE Tactile Scanning Experiments by means of the tangential scanning trajectory.

$$T_h(\downarrow)_{tangential} = (AE_{RMS})_{ground\ noise} + 5(\sigma_{ground\ noise}) \qquad (11)$$

$$T_h(\uparrow)_{tangential} = (AE_{RMS})_{ground\ noise} + 10(\sigma_{ground\ noise}) \qquad (12)$$

The utilization of the axial scanning trajectory during the AE Tactile Scanning Experiments leads to higher amplitudes in the AE signals. Therefore, the levels of the factor T_h are set at higher values in order to cover a representative region in the AE signals. Equation 13 and Equation 14 show the evaluation of the low ($\downarrow$) and the high ($\uparrow$) levels of the factor T_h, respectively, when running the axial scanning trajectory during the AE Tactile Scanning Experiments.

$$T_h(\downarrow)_{axial} = (AE_{RMS})_{ground\ noise} + 20(\sigma_{ground\ noise}) \qquad (13)$$

$$T_h(\uparrow)_{axial} = (AE_{RMS})_{ground\ noise} + 40(\sigma_{ground\ noise}) \qquad (14)$$

In the course of the AE Tactile Scanning Experiments, the evaluation of both the $(AE_{RMS})_{ground\ noise}$ and the $\sigma_{ground\ noise}$ has been carried out previously to each experimental replicate. This procedure was necessary for both scanning trajectories (i.e., tangential and axial

scanning trajectories) in order to maintain experimental repeatability and great accuracy in the values of N.

Before calculating the $(AE_{RMS})_{ground\ noise}$ and the $\sigma_{ground\ noise}$, the grinding wheel is set to rotate with the same cutting velocity used during the AE Tactile Scanning Experiments (i.e., v_s= 30 m/s). Next, the grinding wheel is positioned close to the diamond tip, in a gap distance of 0,5 mm. The ground noise of the AE signal is measured during 3 s and both the $(AE_{RMS})_{ground\ noise}$ and the $\sigma_{ground\ noise}$ are calculated in-process. Such experimental procedure was necessary to estimate the ground noise due to the moving components in the grinding machine (and also regarding external noise sources) which are emitting noise during the AE Tactile Scanning Experiments.

6 RESULTS

This chapter exhibits and discusses the achieved outcomes in the scope of the current research. Firstly, the results regarding the Dynamic Post-process Characterization Method (DPCM) and their validations are presented. In the second part of this chapter, the results obtained by employing the Dynamic In-process Characterization Method (DICM) are shown, and both the validation and the optimization of the method are remarked.

6.1 DYNAMIC POST-PROCESS CHARACTERIZATION METHOD (DPCM)´S RESULTS (AE TACTILE SCANNING EXPERIMENTS)

The results regarding the DPCM are initially related to the analysis of the digitized AE_{RAW} signals derived from the AE Tactile Scanning Experiments. This is carried out by means of: a) parameter N (AE_{RAW} oversteps); and b) parameter σ_x (standard deviation of the AE_{RAW} signal), (see Section 5.3.2.3). Figure 49 shows the time domain results after running the AE Tactile Scanning Experiments.

Figure 49 – Post-process time domain analysis (AE Tactile Scanning Experiments).
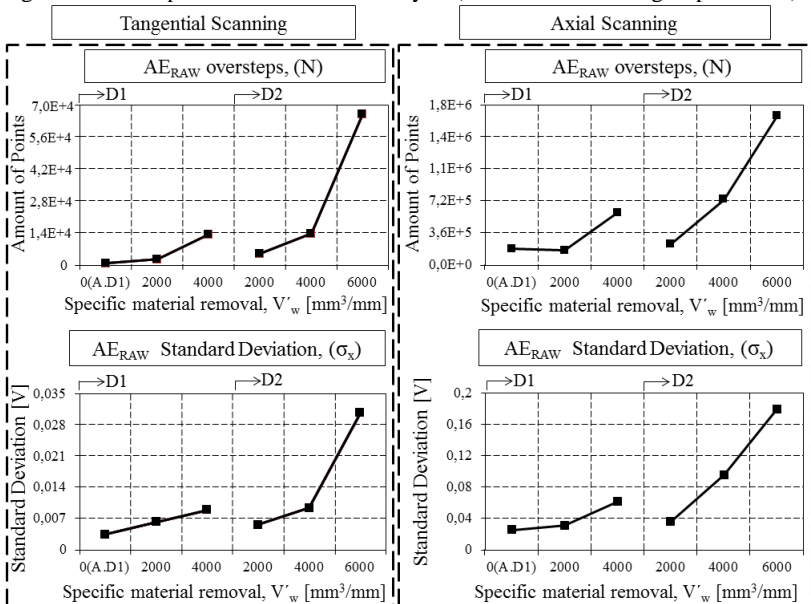
Source: (Developed by the author).

The graphs on the top part of Figure 49 show the time domain outputs resulted from the post-process analysis based on the parameter N. On the left-hand graph of the figure, the outputs achieved when employing the tangential scanning trajectory are highlighted, while the outputs obtained with the axial scanning trajectory are represented on the right-hand graph of the figure. The points plotted on the left portion of both graphs show the initial condition of the grinding wheel after dressing it for the first time in the experiment series (i.e., A.D1), and before grinding the workpiece ($V'_w = 0$ mm^3/mm).

The graphs show a similar trend for both the tangential and the axial scanning trajectories. Either scanning trajectories show a remarkable growth of N over increasing values of V'_w ground in the specimens along the experiment series. In the first experiment series (i.e., from $V'_w = 0$ mm^3/mm up to $V'_w = 4000$ mm^3/mm) the obtained results with both scanning trajectories show that no significant change occurs in the grinding wheel´s topography between $V'_w = 0$ mm^3/mm up to $V'_w = 2000$ mm^3/mm, while at $V'_w = 4000$ mm^3/mm the grinding wheel has a different topography. Before starting the second experiment series, the grinding wheel is dressed for the second time (D2) in order to reestablish its initial condition. The higher amount of material ground in the workpiece leads to pronounced N outputs at $V'_w = 6000$ mm^3/mm, which is considerably higher than the N outputs at $V'_w = 4000$ mm^3/mm. Such increasing trend is obtained by using both scanning trajectories and points out that there exists a substantial difference in the grinding wheel´s topography in this range.

The graphs on the bottom part of Figure 49 display the time domain outputs derived from the post-process analysis based on the parameter σ_x. Such analysis takes into consideration the assumption that the digitized AE_{RAW} signals are stationary (see Section 2.7.5). Therefore, the evaluation of σ_x is based on only one representative sample (experimental repetition) which characterizes the grinding wheel´s topography.

When comparing the outputs from both scanning trajectories, the graphs show a similar increasing trend over higher values of V'_w, which also matches the previous results shown for the parameter N. In the first experiment series, the obtained results with both scanning trajectories indicate that no significant change occurs in the grinding wheel´s topography between $V'_w = 0$ mm^3/mm up to $V'_w = 2000$ mm^3/mm, while at $V'_w = 4000$ mm^3/mm the grinding wheel has a different topography.

In the second experiment series (after D2), the higher amount of material ground in the workpiece conducts to a rise in the σ_x outputs at

V'_w= 6000 mm^3/mm, which is considerably higher than the outputs found at V'_w= 4000 mm^3/mm. Such increasing trend in the σ_x outputs occurs for both scanning trajectories and indicates that the grinding wheel´s topography significantly changes. As the computed time-domain mean value ($\bar{x}$) from all the digitized AE_{RAW} signals results in $\bar{x}$= 0 V, hence the values of σ_x also denote a measure of the energy of the AE_{RAW} signals (i.e., RMS level) over time (SHIN; HAMMOND, 2008). Therefore, it is possible to affirm that the changes in the topography of the grinding wheel are associated with a rise on the energy (power) of the AE_{RAW} signals over increased values of V'_w.

The combined evaluation of the parameters N and σ_x indicates that the topography of the grinding wheel significantly changes during the experiment series. These changes can be detected by using both the tangential and the axial scanning trajectories. Additionally, as the values of N and σ_x are based on the digitized AE_{RAW} signals on-line acquired during the experiments, these parameters reflect the actual topography of the grinding wheel by taking into account the kinematics of the grinding process. Hence, the changes verified in those time-domain parameters are proportional and attributed to the number of kinematic cutting edges per surface area (N_{kin}) of the grinding wheel. In the current research, the increasing trend of both N and σ_x over higher values of V'_w are assigned to a rise of N_{kin}. Such assumption is validated in Section 6.4.

In order to obtain complementary information about the changes occurring in the grinding wheel´s topography along the experiments, the frequency domain analysis is also carried out. This analysis is conducted by evaluating the Power Spectral Density (PSD) of the digitized AE_{RAW} signals (see Section 5.3.2.3). Figure 50 shows the achieved frequency domain results after running the AE Tactile Scanning Experiments.

The graphs denoted as "0 (A.D1)" express the initial condition of the grinding wheel, right after the first dressing process (D1) and before grinding the workpiece (V'_w= 0 mm^3/mm). The following graphs represent the PSD results related to the second experiment series, in which the highest amount of material is ground on the workpiece (A.D2; from V'_w= 2000 mm^3/mm up to V'_w= 6000 mm^3/mm).

The resulting graphs from both scanning trajectories show that the maximum frequency content is f_{max}= 100 kHz, as the AE_{RAW} signals are digitized by using the sampling rate f_s= 200 kHz. This value is twice as high as the selected cut-off frequency of the analog low-pass filter (i.e., $f_{cut-off}$= 100 kHz) in the AE-MS.

For both the tangential scanning trajectory and the axial scanning trajectory, the frequency domain signals present an analogous tendency as V´$_w$ assumes higher values.

Figure 50 – Post-process frequency domain analysis (AE Tactile Scanning Experiments).
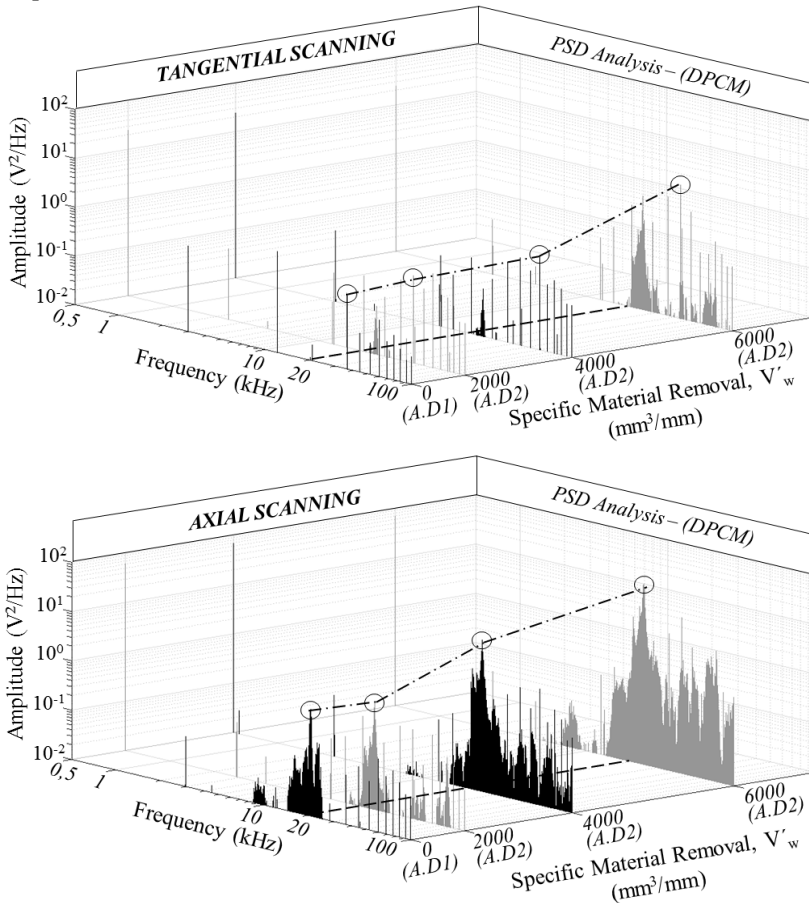
Source: (Developed by the author).

This tendency is characterized by a progressively shift in the AE$_{RAW}$ spectrum which shows a remarkable rise in the high frequency content above 20 kHz (Figure 50, dashed line), as V´$_w$ gets higher.

By only observing the distribution of the PSD in the range from V´$_w$= 2000 mm^3/mm up to V´$_w$= 4000 mm^3/mm, no significant changes

seem to occur when running the tangential scanning trajectory. The PSD results obtained by means of the axial scanning trajectory in this range show that the grinding wheel´s topography changes. The same trend is verified when observing the magnitudes of the AE_{RAW} spectrum (Figure 50, circular markers, also known as the RMS level of the AE_{RAW} signals) in this range. From $V'_w = 4000$ mm^3/mm up to $V'_w = 6000$ mm^3/mm, the RMS level of the AE_{RAW} signals considerably increases as V'_w gets higher (Figure 50, dash-dot line connecting the circular markers). Such trend is verified for both the tangential and the axial scanning trajectories.

The analysis of the PSD results obtained by means of the axial scanning trajectory shows that in the spectral range varying from 20 kHz up to 100 kHz there is a rise of the characteristic frequencies which are excited over increased values of V'_w.

The results verified in the AE_{RAW} spectrum for both scanning trajectories correlate with the previous achieved results in the corresponding time domain analyses. Such tendency noted in the AE_{RAW} spectrum can be attributed to the growth of N_{kin} taking effect on the grinding wheel´s topography as V'_w reaches higher values. This assumption is validated in Section 6.4.

6.2 DYNAMIC POST-PROCESS CHARACTERIZATION METHOD (DPCM)´S RESULTS (SCRATCH EXPERIMENTS)

In order to appraise the changes occurring on the grinding wheel´s topography along the experiment series, the AE_{RAW} signals acquired during the Scratch Experiments are investigated in the frequency domain. This analysis is conducted by evaluating the Power Spectral Density (PSD) of the digitized AE_{RAW} signals. Such evaluation occurs after finishing the Scratch Experiments, that is, it represents a post-process analysis. Figure 51 shows the achieved frequency domain results after running the Scratch Experiments.

The graphs shown on the left-hand side of Figure 51 express the PSD results related to the first experiment series (A.D1, from $V'_w = 2000$ mm^3/mm up to $V'_w = 4000$ mm^3/mm), whereas the graphs on the right-hand side exhibit the PSD results related to the second experiment series (A.D2, from $V'_w = 2000$ mm^3/mm up to $V'_w = 6000$ mm^3/mm).

Figure 51 – Post-process frequency domain analysis (Scratch Experiments).
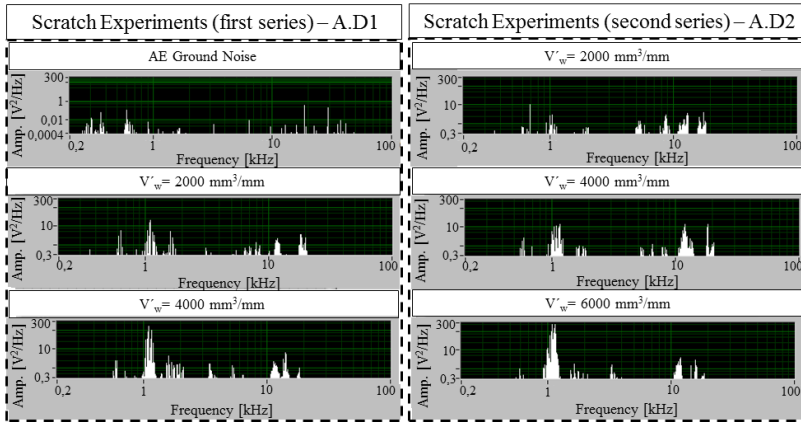
Source: (Developed by the author).

Each PSD graph expresses the AE spectrum from the last 10 s extracted from the digitized AE_{RAW} signals. As the original digitized AE_{RAW} signals are sampled with f_s= 125 kS/s and the total time duration of the AE_{RAW} signals is relatively high (i.e., $T_{scratch}$= 300 s, plunge grinding) it was not possible to implement such analysis based on the complete time-history of the signal, but rather only in fractioned parts of the digitized AE_{RAW} signal.

Therefore, in order to allow implementing the frequency domain analysis, the AE_{RAW} signals must firstly be fractionated (i.e., lesser time domain duration, $\delta T_{scratch}$= 10 s) and be resampled (by using f_s= 100 kS/s). All the PSD graphs present the same frequency content f_{max}= 50 kHz, as the AE_{RAW} signals are resampled by using f_s= 100 kHz. This value is twice as high as the selected cut-off frequency of the digital low-pass filter ($f_{cut-off, digital}$= 50 kHz) used during the analysis.

On the top left side of the Figure 51, the PSD result obtained for the AE_{RAW} ground noise level (before running the Scratch Experiments) is shown. The comparison of this graph with the other PSD results confirms that the differences in the PSD graphs are significant and are not influenced by the AE_{RAW} signal´s ground noise which is present in the AE_{RAW} signals.

For both the first and the second series of experiments the frequency domain signals present a similar trend as $V´_w$ increases. This trend is characterized by a remarkable shift in the AE_{RAW} spectrum, which changes from a highly broad spectrum at $V´_w$= 2000 mm^3/mm

(after dressing, A.D1 and A.D2) to a quite better defined spectrum content, after plunge grinding higher values of $V´_w$. The growth of $V´_w$ also excites particular frequencies in the lower content of the AE spectrum (e.g., f= 1,5 kHz) which can also be related to the grain breakage and chip removal process (MARGOT, 2005). Additionally, the RMS level of the AE_{RAW} signals (i.e., PSD´s magnitude) considerably increases as $V´_w$ gets higher.

The results verified in the AE_{RAW} spectrum for both experiment series correlate with the previous achieved results obtained by means of the AE Tactile Scanning Experiments (tangential and axial scanning trajectories). The noted patterns in the AE_{RAW} spectrums (based on the PSD´s magnitude) derived from the Scratch Experiments can also be attributed to a rise of N_{kin} as $V´_w$ assumes higher values. Such assumption is validated through specific measuring results which are described in Section 6.4.

6.3 DYNAMIC POST-PROCESS CHARACTERIZATION METHOD (DPCM)´S RESULTS (SELF-ORGANIZING MAP NEURAL NETWORK, SOM-NN)

Aiming at obtaining additional qualitative information about the changes caused to the grinding wheel´s topography through the Scratch Experiments regarding the DPCM, a SOM-NN was employed. Such NN permits to cluster different patterns related to the topography of the grinding wheel in a bi-dimensional neuron map. Figure 52 shows the SOM-NN´s results after training it by using 1500 points (i.e., peaks of the PSD function) which represent the 1500 s of plunge grinding during the Scratch Experiments.

The output of the SOM-NN consists in a neuron map composed of 400 neurons (i.e., matrix: 20 neurons x 20 neurons) connected in a hexagonal arrangement. The lines in the neuron map symbolize the connections among the neurons which are represented by the dark circles. The neuron map represents the weighted distances between the participant neurons in the map. Bright regions in the SOM-NN´s map symbolize a close proximity (or similarity) among adjacent neuron weights, whereas the dark regions characterize dissimilarities between adjacent neurons (i.e., high weight distances).

The SOM-NN´s output points out that three distinct regions do arise in the map, thus suggesting the existence of different patterns in the inputs (i.e., peaks of the AE_{RAW} signals´ PSD functions) which are evaluated by the SOM-NN in its input layer.

Figure 52 – Self-Organizing Map Neural Network (SOM-NN)´s results: SOM-NN Map.
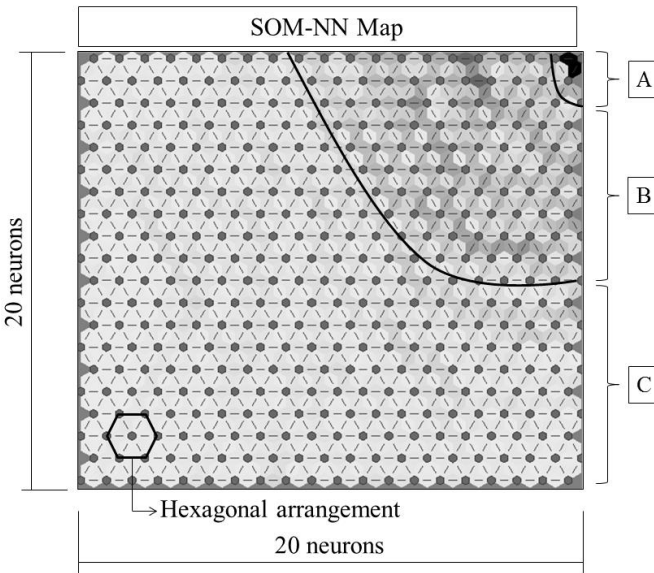
Source: (Developed by the author).

These distinct regions in the SOM-NN map possess different sizes when observing the results. In the broadest region (Figure 52-C), the neurons are normally activated by the inputs related to less wear on the grinding wheel. This is observed in the range varying from $t_1 = 0$ s up to $t_2 = 10$ s of the Scratch AE_{RAW} signals associated with both $V´_w = 2000$ mm^3/mm and $V´_w = 4000$ mm^3/mm. On the other hand, the neurons situated in the darkest regions of the map (i.e., Figure 52-A and Figure 52-B) are normally excited by the inputs associated with more pronounced wear of the grinding wheel. This is verified for the inputs related to both mid-term wear (i.e., in the range varying from $t_1 = 290$ s up to $t_2 = 300$ s in the Scratch AE_{RAW} signals associated with both $V´_w = 2000$ mm^3/mm and $V´_w = 4000$ mm^3/mm, Figure 52-B) and more pronounced wear (i.e., in the range varying from $t_1 = 290$ s up to $t_2 = 300$ s in the Scratch AE_{RAW} signal associated with $V´_w = 6000$ mm^3/mm, Figure 52-A).

6.4 DYNAMIC POST-PROCESS CHARACTERIZATION METHOD (DPCM)´S VALIDATION

The procedures and measurements which have been performed for validating the DPCM´s results are described in this section. The validation of results takes into account the assessment of the working results on the workpiece (i.e., R_{ts} roughness, profile deviation, SEM microscopy and the thermally affected layer) and on the replicas extracted from the grinding wheel´s topography. Additionally, the measurements on the single-point diamond tip used for the AE Tactile Scanning Experiments are also described.

6.4.1 Actual Grinding Wheel Surface Roughness (R_{ts})

Roughness measurements on ground components permit to obtain valuable information about the quality of the workpiece and also allow inferring the correlated grinding wheel´s topography. In the current research, the roughness parameter R_{ts} (actual grinding wheel surface roughness) was measured aiming at gaining information about the topography of the grinding wheel.

The evaluation of the roughness R_{ts} is carried out by measuring the roughness of the workpiece (i.e., parameters R_a, R_{sk}, R_t, and R_z) derived from the plunge grinding process with the rotational ratio q= 1:6. For the proposed rotational ratio q= 1:6 (i.e., one complete rotation of the grinding wheel for each 1/6 rotation of the workpiece) the grinding wheel´s periphery is represented six times over the periphery of the workpiece. By measuring the workpiece´s roughness in different angular positions incremented by 20°, average information is achieved regarding the topography of the grinding wheel (KÖNIG, 1989). Figure 53 shows the R_{ts} measurement results over increased values of $V´_w$ in the course of the Scratch Experiments.

Figure 53 – Actual grinding wheel surface roughness (R_{ts}).
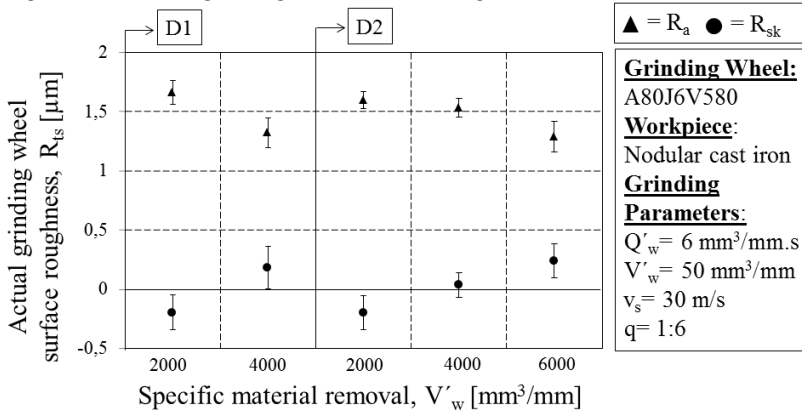
Source: (Developed by the author).

The central points plotted in Figure 53 correspond to the mean values of the roughness measurements (n= 18 measurements) in the predefined positions of the workpieces. The means´ variances are represented by the vertical lines and show the spread of the measuring results which are obtained over increased values of $V´_w$. On the top part of the figure, D1 and D2 represent the instants in which the grinding wheel was dressed, before starting the first and the second experiment series, respectively.

The R_{ts} measuring results based on the evaluation of the roughness parameter R_a (arithmetical mean deviation) are plotted on the upper part of the Figure 53. The parameter R_a denotes the arithmetic average of the absolute values of the roughness profile ordinates and is one of the most commonly adopted parameters in the engineering practice. It offers a good overall description of the height deviations in the measured surface (JENOPTICK; HOMMEL, 2009). However, such roughness parameter does not differentiate between peaks and valleys on the measured surface.

The R_{ts} analysis by means of the parameter R_a shows a decreasing trend over gradually enlarged values of $V´_w$, for both experiment series. This tendency indicates that in the course of the grinding process the quantity of kinematic cutting edges (N_{kin}) which are involved in the grinding process increases. The roughness improvement verified over higher values of $V´_w$ is also related to the fact that higher values of N_{kin} reduce h_{cu} (statistically average maximum underformed chip thickness), thus conducting to reduced R_{ts} values evaluated on the workpiece

(KLOCKE; KÖNIG, 2005). Therefore, such behavior of the grinding wheel´s topography leads to the assumption that N_{kin} increases with higher values of $V´_w$ for the specific set of grinding parameters used in the Scratch Experiments. This trend also correlates with the previous results from the AE Tactile Scanning Experiments and the Scratch Experiments, in both the time and frequency domains. When analyzing the R_{ts} results through the other roughness parameters (i.e., R_t and R_z) the same pattern was observed in the measuring results.

On the bottom part of Figure 53, the R_{ts} measurement results derived from the assessment of the roughness parameter R_{sk} (skewness) are plotted. The roughness parameter R_{sk} is a measure of the symmetry of the roughness profile in relation to an average line, and offers a suitable manner to characterize both load carrying capability, and porosity characteristics of machined surfaces (DORNFELD; LEE, 2008). Negative values of R_{sk} are associated with a flat-like surface, whereas positive values of such roughness parameter represent a common peak-like surface (JENOPTIK; HOMMEL, 2008; MAHR, 2011).

The R_{ts} analysis by means of the roughness parameter R_{sk} shows a significant rising trend as $V´_w$ assumes higher values. These results point out that over increased values of $V´_w$ there is also a substantial change in the topography of the grinding wheel, which alters from a flat-like surface (negative R_{sk}) to a peak-like dense surface (positive R_{sk}). The flat-like behaviour verified for lower values of $V´_w$ is attributed to the dressing process, whereas the positive values of R_{sk} show that the grinding wheel presents a good friability, thus exposing new and sharp cutting edges over higher values of $V´_w$. These patterns also match the previous achieved results when using the AE Tactile Scanning Experiments and the Scratch Experiments, in both the time and the frequency domains.

6.4.2 Measurements of the Grinding Wheel´s Replicas

Measurements of the grinding wheel´s replicas consist in a conceivable method to overcome technical restrictions in performing direct measurements on grinding wheels. Such technique is also used when the changes in the surface of the grinding wheel need to be monitored within a dressing cycle (ROWE et al., 2004). In the current research, replicas extracted from the grinding wheel have been measured aiming at evaluating the topography of the grinding wheel without removing it from the grinding machine.

For estimating the changes occurring in the grinding wheel´s topography during the experiments, the replicas are extracted after grinding a specific material removal V'_w on the workpiece. The measurement of the replicas is afterwards executed by means of an optical measuring system (see Section 4.8) and the obtained results are plotted in Figure 54.

The central points plotted in Figure 54 correspond to the mean values of the measurements in each replica of the grinding wheel (n= 4 measurements) and the variances are represented by the vertical lines. On the left-hand side of the figure, the measuring result from the replica extracted after the first dressing of the grinding wheel (A.D1) and without grinding the workpiece ($V'_w= 0$ mm³/mm) is represented. No replica is extracted from the grinding wheel right after dressing it for the second time (D2) in the experiments.

Figure 54 – Measurements of the grinding wheel´s replicas.
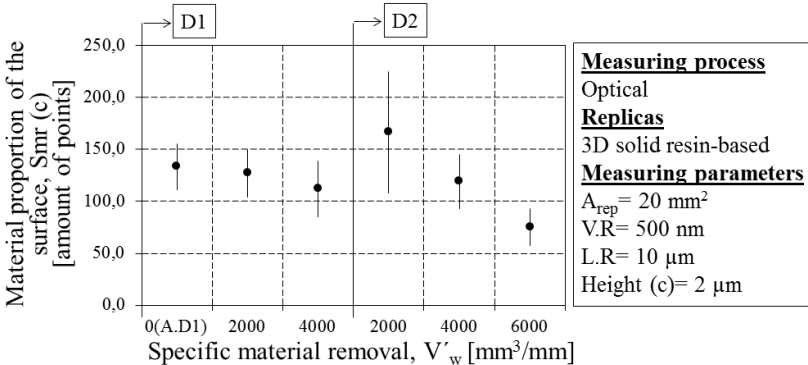
Source: (Developed by the author).

For all measurements, the height "c" was set down to 2 µm in relation to the highest peak of the replicas´ surfaces which is defined by analyzing the Abbot-curve of the 3D measured data set. This value corresponds to the same range in which the AE Tactile Scanning Experiments were investigated. Therefore, the exposed results represent the static topography of the grinding wheel in the range of 2 µm.

The analysis of the surface parameter Smr(c) (i.e., material proportion of the surface as a function of the height "c") shows a decreasing trend over gradually enlarged values of V'_w, for both experiment series. By assuming that the measuring results can be extrapolated to the whole periphery of the grinding wheel, such pattern

indicates that the topography of the grinding wheel changes considerably. These changes in the grinding wheel´s topography indicate that the static roughness of the grinding wheel drops as $V´_w$ gets higher. Such pattern also matches the R_{ts} results based on the R_a analysis, where a roughness improvement is verified in the ground workpieces over increased values of $V´_w$. Additionally, by comparing the Smr(c) results with the R_{ts} evaluation derived from the R_{sk} analysis, the peak-like behaviour of the grinding wheel can also be confirmed as $V´_w$ increases. The topographic characteristic of the grinding wheel found by means of the replicas´ measurements also correlates with both the time and frequency domain analyses derived from both the AE Tactile Scanning Experiments and the Scratch Experiments´ results.

6.4.3 Scanning Electrical Microscope (SEM) Images

Scanning Electrical Microscope (SEM) images have been used in the current research for qualitative characterizing the topography of the grinding wheel. The assessment of the grinding wheel´s topography is carried out indirectly, by analyzing the images taken from specific regions on the ground surfaces of the workpiece, Figure 55.

Figure 55 – Scanning Electrical Microscope (SEM) images from ground surfaces.
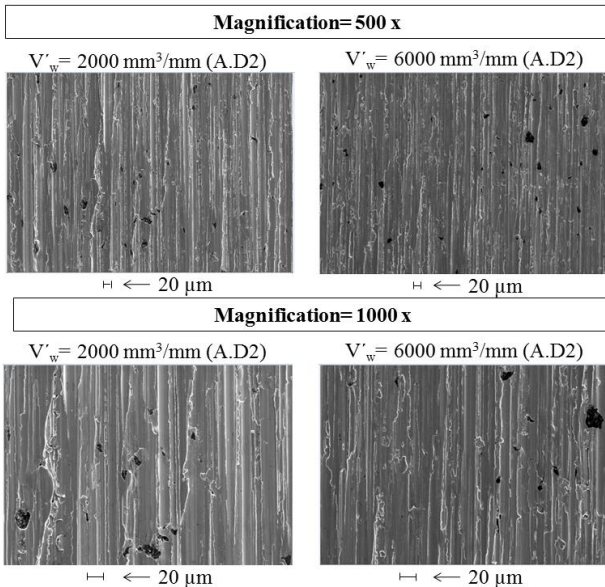
Source: (Developed by the author).

The SEM images shown in Figure 55 are taken from the workpiece´s surfaces after grinding $V´_w$= 2000 mm^3/mm and $V´_w$= 6000 mm^3/mm. These values comprehend respectively the lower and upper limits of the broader material removal range in the experiments (i.e., second series), where significant changes in the grinding wheel´s topography are expected. On the upper part of the figure, the images obtained with 500 x magnifications are illustrated, while the bottom part shows the extracted images by employing magnification 1000 x. The irregular black areas noticeable in the images represent the graphite structures which have been ground and are dispersed on the structure of the nodular casting iron.

The comparison of the SEM images taken at $V´_w$= 2000 mm^3/mm and at $V´_w$= 6000 mm^3/mm highlights a significant difference on the ground surface, thus also indicating that the topography of grinding wheel considerably changes in this experimental range. The SEM images extracted at $V´_w$= 2000 mm^3/mm present a similar pattern which shows the predominance of non-straight lines when compared with the images at $V´_w$= 6000 mm^3/mm for both magnification factors. It is also possible to observe that at $V´_w$= 2000 mm^3/mm the average distance between adjacent parallel paths is higher than at $V´_w$= 6000 mm^3/mm. Such patterns indicate that at $V´_w$= 2000 mm^3/mm the material removal process is significantly accompanied by sideway displacements (ploughing, curved lines) and not by a completely material removal from the workpiece in the cutting direction. This can be attributed to a grinding wheel topography in which N_{kin} is considerably small and the cutting edges of the grinding wheel are not sharp enough. On the contrary, the patterns verified at $V´_w$= 6000 mm^3/mm show the material removal process occurs more effectively in the cutting direction (i.e., lesser existence of curved lines), therefore indicating that more cutting edges are getting involved in the process (i.e., high N_{kin}) and that the cutting edges are sharper.

By comparing the patterns verified on the SEM images it is possible to observe that the grinding wheel´s topography changes from a flat-like to a peak-like behaviour. This trend matches the R_{ts} results as well as the results derived from the measurements of the grinding wheel´s replicas. Additionally, this tendency also correlates with the mentioned assumption drawn from the AE Tactile Scanning Experiments (in both the time and frequency domains) and from the Scratch Experiments.

6.4.4 Diamond Tip Measurements

Diamond tip measurements were carried out previously and after finishing the AE Tactile Scanning Experiments aiming at assessing occasional wear of the single-point diamond tip due to the experiments. These measurements evaluate both the profile and the radius of the single-point diamond tip (R_{tip}) in a 3D optical machine by means of a NC program. Figure 56 shows a typical measuring result of the diamond tip´s frontal profile after finishing the AE Tactile Scanning Experiments.

Figure 56 **–** Diamond tip measurements.
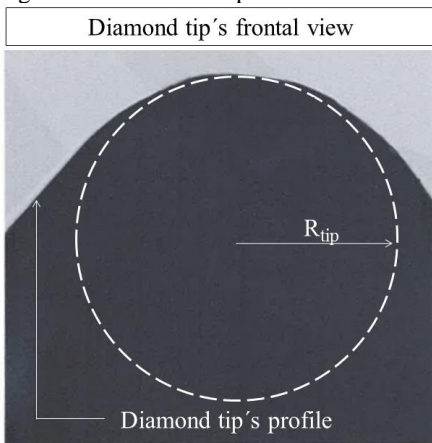
Source: Adapted and based on (CERTI, 2012).

The measuring result is derived from three repetitive measurements of the single-point diamond tip in order to get an average information regarding R_{tip}. The plotted profile confirms that no localized damage occurs on the diamond tip´s surface. By comparing the obtained values of the diamond tip´s radius before starting the experiments ($R_{tip/B}$) and after finishing the experiments ($R_{tip/A}$), practically the same values have been found (i.e., $R_{tip/A} \approx R_{tip/B} = 0,407 \pm 0,003$ mm). This indicates that the single-point diamond tip does not suffer any significant wear during the AE Tactile Scanning Experiments.

6.4.5 Profile Measurements

Profile measurements on the ground workpiece have been carried out in order to indirectly estimate the macrotopography of the grinding wheel due to the Scratch Experiments. In the Scratch Experiments, the successive plunge movement of the grinding wheel onto the workpiece leads to a progressive radial wear on the grinding wheel´s surface. After grinding $V'_w= 6000$ mm^3/mm in the second experiment series, the grinding wheel is imprinted on a particular surface of the workpiece (i.e., "imprint surface", see Section 4.2). Figure 57 shows the profile measurement results evaluated on the ground workpiece.

Figure 57 – Profile measurements on the ground workpiece.
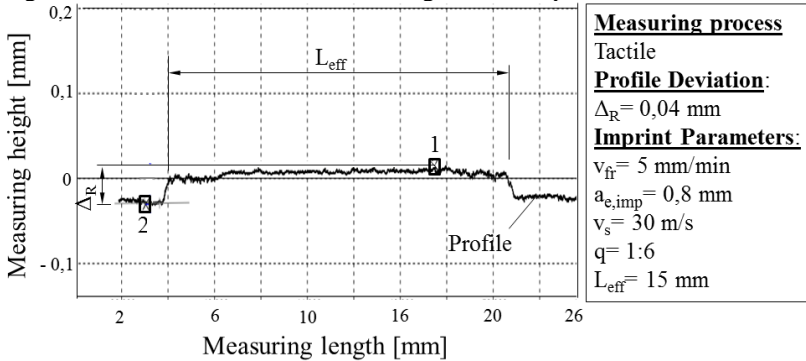
Source: (Developed by the author).

The stepped-form continuous line in Figure 57 represents a profile measurement of the workpiece which is obtained by means of the measuring system´s software. As the measured profile consists in the "negative" form of the grinding wheel´s topography, the longest length of the profile highlights the effective width of the grinding wheel (i.e., $L_{eff}= 15$ mm) which grinds the workpiece during the Scratch Experiments. The form deviation ($\Delta_R= 0,04$ mm) verified on the measured profile indicates the average radial wear of the grinding wheel after measuring the workpiece in 3 distinct cylindrical positions.

For each measurement, the integrated software firstly evaluates the best fit line at L_{eff}, which serves as a measuring reference. Next, the assessment of the Δ_R occurs by measuring the vertical distance between the steepest point on L_{eff} (point 1, Figure 57) and the mean value on the lower portion of the profile (point 2, Figure 57).

6.4.6 Thermally Affected Surface Layer of Ground Workpieces

The surface layer of the ground workpieces has been investigated in order to infer possible thermal-related events due to the Scratch Experiments. For that, ground specimens were prepared by initially polishing and etching and afterwards were analyzed through microscopy, Figure 58.

Figure 58 – Thermally affected surface layer of ground workpieces.

a) $V'_w = 2000$ mm^3/mm, (A.D2)

$\delta = 100$ μm

c) Workpiece´s microstructure

b) $V'_w = 6000$ mm^3/mm, (A.D2)

$\delta = 100$ μm

200 μm

d)

Ferrite

Graphite

Perlite
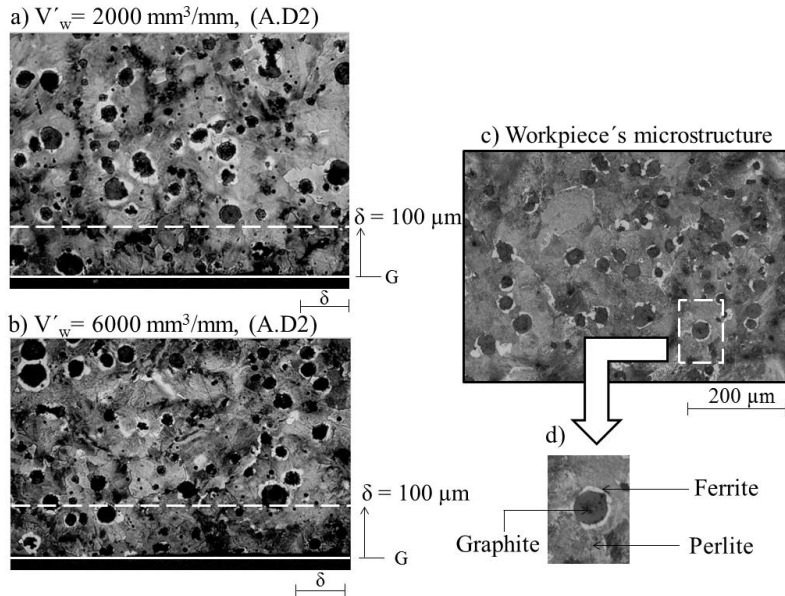
Source: (Developed by the author).

The images shown on the left-hand side of Figure 58 (magnification= 100 x) are taken from the specimens´ surfaces after grinding $V'_w = 2000$ mm^3/mm (Figure 58-a) and $V'_w = 6000$ mm^3/mm (Figure 58-b) during the second series of experiments (i.e., A.D2). On the right-hand side of the figure, the detached image shows the metallographic result of a distinct specimen, extracted from a central portion of the workpiece, which has not been ground (Figure 58-c). The uneven black areas represent the graphite structures which are surrounded by ferrite and dispersed in a perlite matrix on the microstructure of the nodular casting iron, (Figure 58-d) (BDG, 2007).

The images related to $V'_w= 2000$ mm^3/mm and $V'_w= 6000$ mm^3/mm highlight that a similar pattern among the images exists, which is characterized by two different regions in each image. In the region ranging from the vicinity of the ground surface (Figure 58-a and Figure 58-b, ground, "G") up to the depth layer $\delta \approx 100$ µm (Figure 58-a and Figure 58-b, dashed lines), both images show that the average size of the graphite nodules are considerably smaller than the average size of the graphite nodules lying in the deeper region of the specimens (i.e., $\delta > 100$ µm). Furthermore, it is also possible to observe that the ferrite-phase which involves the graphite nodules tends to reduce in the layer varying from $\delta= 0$ µm (i.e., ground surface, "G") up to $\delta= 100$ µm.

When comparing the images related to $V'_w= 2000$ mm^3/mm and $V'_w= 6000$ mm^3/mm in the same layer (i.e., 0 µm $< \delta < 100$ µm), a significant drop in the ferrite-phase is perceptible at $V'_w= 2000$ mm^3/mm. The noted change in the microstructure of the layer can be related to the flat-like topography of the grinding wheel at $V'_w= 2000$ mm^3/mm. This leads to a higher overall friction between the tool and the workpiece, thus increasing the overall thermal stress (energy) which is transferred to the worpiece´s layer. Despite the mentioned changes in the specimens´ microstructural layer, no cracks have been noted neither at $V'_w= 2000$ mm^3/mm nor at $V'_w= 6000$ mm^3/mm.

In addition to the flat-like topography at $V'_w= 2000$ mm^3/mm, further influencing factors on the heat generation that could not be neglected are: a) large contact length between the grinding wheel and workpiece during the Scratch Experiments (i.e., plunge grinding); b) reduced thermal conductivity coefficient of the aluminum oxide grits at higher temperatures (KÖNIG; KLOCK, 2005) and c) relatively reduced v_w in the course of the Scratch Experiments.

6.5 DYNAMIC IN-PROCESS CHARACTERIZATION METHOD (DICM)´S RESULTS

The results regarding the DICM are based on both the time and frequency domain outputs which are obtained in-process through the AE Quick Test Method. These outputs are instantaneously visualized on the laptop´s screen (when pushing the "stop" button of the acquisition program) immediately after finishing the AE Tactile Scanning Experiments. The obtained results in the course of the experiment series are exposed and discussed in the coming sections.

6.5.1 Dynamic In-process Characterization Method (DICM)´s Results (First Experiment Series)

In the first experiment series, the DICM´s results are firstly related to the time domain outputs by employing the AE Quick Test Method: a) parameter N (AE oversteps), and b) parameter σ_x (standard deviation), (see Section 5.3.2.3). Figure 59 shows the achieved time domain results for the experimental condition "abc" (i.e., f_s= 400 kS/s, T.S= AE_{RAW}, T_h= high).

Figure 59 – In-process time domain outputs (AE Quick Test Method), first experiment series.
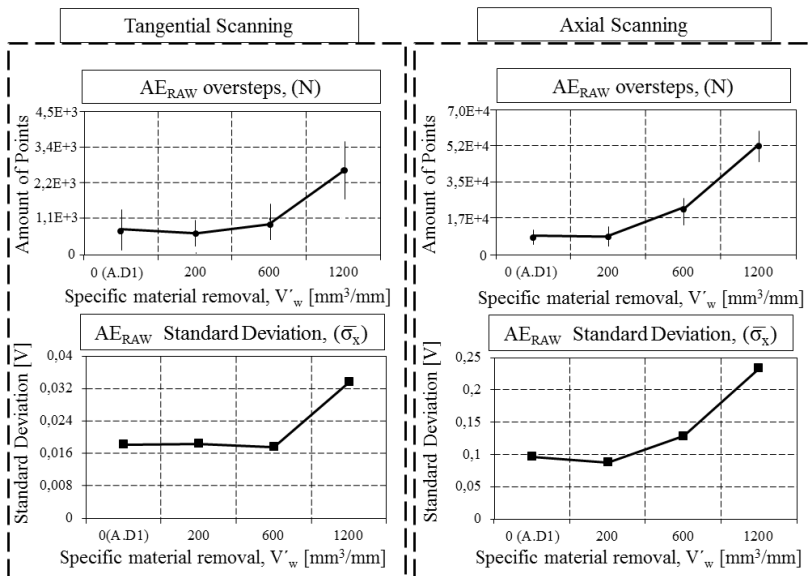
Source: (Developed by the author).

The upper part of Figure 59 shows the time domain outputs resulted from the in-process analysis based on the parameter N. On the top-left part of the figure, the achieved outputs with the tangential scanning trajectory are indicated, while the N outputs obtained with the axial scanning trajectory are represented on the top-right part of the figure. The centralized points represent the N mean value (sample size, n= 3 replicates) and the vertical lines denote the N mean´s variance. The N results plotted on the left portion of both graphs show the initial

condition of the grinding wheel after dressing it for the first time (A.D1) and before grinding the workpiece (i.e., $V'_w = 0$ mm^3/mm).

The graphs show a similar trend for both the tangential and the axial scanning trajectories by employing the AE Quick Test Method. Either scanning trajectories show a remarkable growth in the average number of N for increasing values of V'_w ground in the specimens along the experiments. When considering the tangential scanning trajectory, such a trend is quite pronounced in the range from $V'_w = 600$ mm^3/mm up to $V'_w = 1200$ mm^3/mm, while for the axial scanning trajectory the computed average values of N are significantly different from $V'_w = 200$ mm^3/mm up to $V'_w = 1200$ mm^3/mm. A further comparison among both scanning trajectories permits to realize that the N means´ dispersion by using the axial scanning trajectory is considerably reduced than the N means´ dispersion when employing the tangential trajectory. Additionally, it is also possible to note a higher slope between $V'_w = 200$ mm^3/mm and $V'_w = 1200$ mm^3/mm for the mean values of N obtained by using the axial scanning trajectory.

The bottom part of Figure 59 displays the time domain outputs derived from the in-process evaluation of σ_x. The outputs achieved by means of the tangential scanning trajectory are indicated on the left side and the outputs obtained with the axial scanning trajectory are shown on the right side. The plotted squares illustrate the σ_x mean values (i.e., $\overline{\sigma}_x$, sample size n= 3 replicates). When comparing the outputs from both scanning trajectories, the graphs show a similar increasing trend over higher values of V'_w, which also matches the previous results shown for the parameter N. Particularly for the tangential scanning trajectory, such increasing trend is more pronounced between $V'_w = 600$ mm^3/mm and $V'_w = 1200$ mm^3/mm, while maintaining practically constant from $V'_w = 0$ mm^3/mm up to $V'_w = 600$ mm^3/mm. On the other hand, the results obtained with the axial scanning trajectory present a tendency for higher values which initiates previously at $V'_w = 200$ mm^3/mm when compared with the tangential scanning.

The combined evaluation of both time domain parameters indicates that both the tangential and the axial scanning trajectories recognize different grinding wheel´s topographies associated with distinct wear of the grinding wheel (i.e., between $V'_w = 200$ mm^3/mm and $V'_w = 1200$ mm^3/mm). Furthermore, the axial scanning trajectory shows a better accuracy (i.e., less dispersion) in recognizing small differences in the grinding wheel´s topography, as noted for example between $V'_w = 200$ mm^3/mm and $V'_w = 600$ mm^3/mm).

In order to obtain complementary information about the changes occurring in the grinding wheel´s topography, the frequency domain output is also computed in-process. Figure 60 shows the frequency domain outputs for the experimental condition "abc" (i.e., f_s= 400 kS/s, T.S= AE_{RAW}, T_h= high), when running the AE Quick Test Method.

The frequency domain outputs show the evaluation of the AE_{RAW} spectrum by computing the Power Spectral Density function (PSD). The graphs on the top and on the bottom part of the figure show the results derived from the tangential and the axial scanning trajectory, respectively.

Figure 60 – In-process frequency domain outputs (AE Quick Test Method), first experiment series.
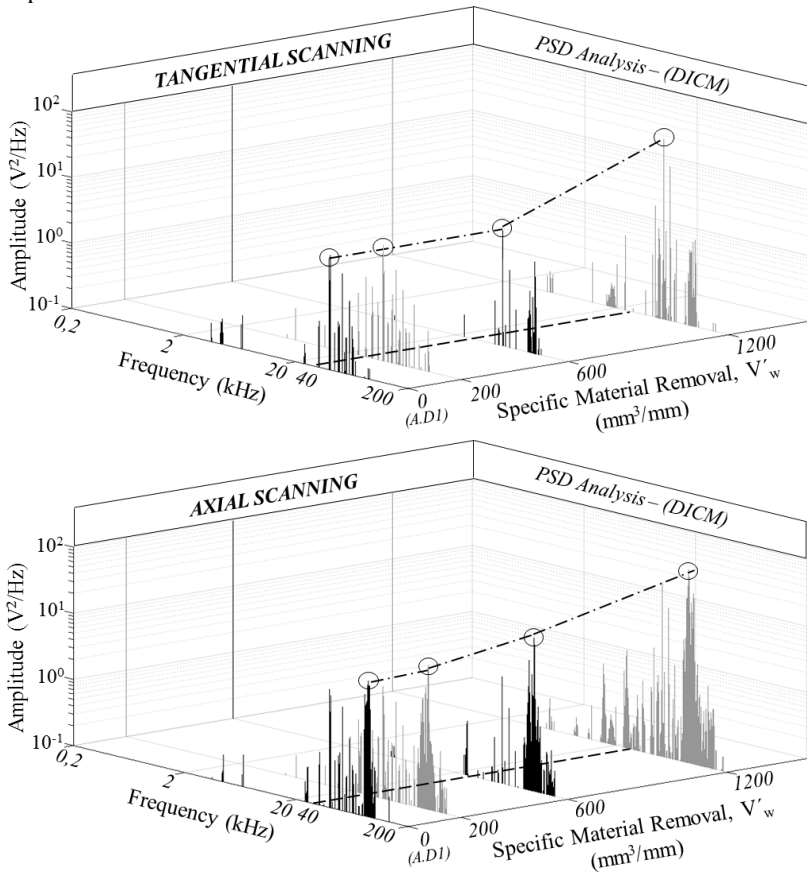
Source: (Developed by the author).

The graphs labelled as "0 (A.D1)" express the initial in-process condition of the grinding wheel, right after the first dressing process (D1) and before grinding the workpiece (i.e., $V'_w= 0$ mm³/mm). The additional plotted graphs are also appraised in-process for each specific stage of the experiment series and are related to a predefined specific material removal V'_w ground on the workpiece. By observing the PSD graphs derived from both scanning trajectories, the maximum frequency content is $f_{max}= 200$ kHz, as in this experimental run the AE_{RAW} signals are digitized by using $f_s= 400$ kHz. Such value is twice as high as the selected cut-off frequency of the analog low-pass filter (i.e., $f_{cut-off}= 200$ kHz) adjusted in the AE coupler.

For both the tangential scanning trajectory and the axial scanning trajectory, the frequency domain signals present a similar trend as V'_w increases. This trend is characterized by a progressively shift in the general spread of the AE_{RAW} spectrum, which displays a significant growth in the high frequency content above 40 kHz (dashed line, Figure 60), as V'_w gets higher.

Regarding the RMS level of the AE_{RAW} signals (i.e., PSD´s magnitude, Figure 60, circular markers), it is also possible to note that a substantial rise occurs from $V'_w= 0$ mm³/mm up to $V'_w= 1200$ mm³/mm when running both scanning trajectories (Figure 60, dash-dot line connecting the circular markers). The RMS level of the AE_{RAW} signals obtained by means of the tangential scanning trajectory shows, however, a substantial difference in the grinding wheel´s topography is only noticeable between $V'_w= 600$ mm³/mm up to $V'_w= 1200$ mm³/mm. On the other hand, the computed RMS level of the AE_{RAW} signals by using the axial scanning trajectory indicates that significant differences in the grinding wheel´s topography arise earlier (i.e., at $V'_w= 200$ mm³/mm) and progress up to the end of the experiment series (i.e., at $V'_w= 1200$ mm³/mm).

The trends verified in the AE_{RAW} spectrums for both scanning trajectories match the previous obtained results in the correspondent time domain analyses. Such tendency noted in the AE_{RAW} spectrums can be attributed to the growth of N_{kin} taking effect on the grinding wheel´s topography as V'_w gets higher. This assumption is confirmed through the validation of the results (see Section 6.6).

6.5.2 Dynamic In-process Characterization Method (DICM)´s Results (Second Experiment Series)

In the second experiment series, both the time and frequency domain analyses are investigated under a distinct condition in the topography of the grinding wheel. The dissimilar topography in the fused aluminum oxide grinding wheel is obtained by changing only the specific material removal rate during the Scratch Experiments (i.e., $Q'_{w=}$ 12 mm^3/mm.s). All the additional dressing and grinding parameters are kept constant and equal to those used during the first experiment series. The assessment of the grinding wheel´s topography is performed through the AE Quick Test Method, by firstly in-process evaluating the time domain parameters N and σ_x. Figure 61 shows the achieved time domain results for the experimental condition "abc" (i.e., f_s= 400 kS/s, T.S= AE$_{RAW}$, T_h= high).

Figure 61 – In-process time domain outputs (AE Quick Test Method), second experiment series.
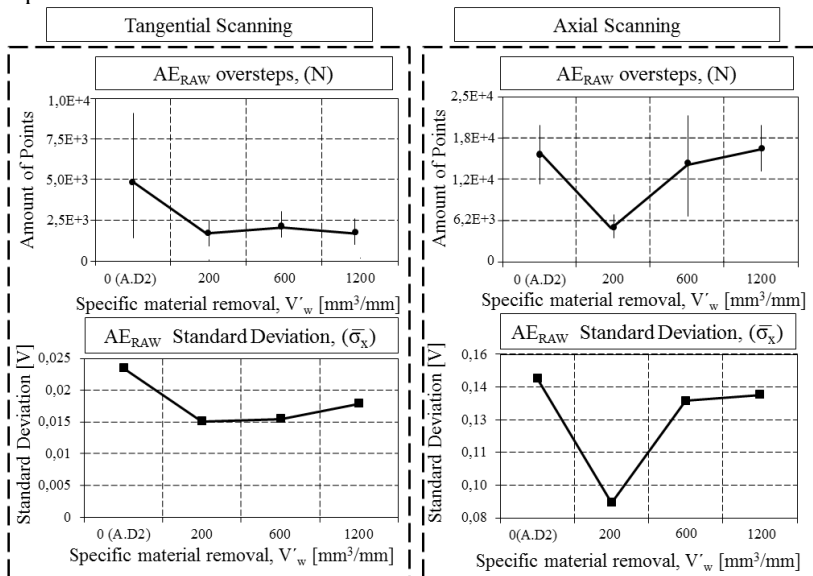
Source: (Developed by the author).

The time domain outputs related to the parameters N and $\overline{\sigma}_x$ are plotted on the upper and on the bottom part of the figure, respectively. The left-hand part of Figure 61 indicates the outputs accomplished with

the tangential scanning trajectory and the right-hand part shows the outputs obtained with the axial scanning trajectory. Both the centralized points and squares in the plotted graphs denote the mean values (sample size, n= 3 replicates) of N and $\bar{\sigma}_x$, respectively. The vertical lines consist in the means´ variances of the time domain parameter N. The initial condition of the grinding wheel after the second dressing process (A.D2) and before grinding the workpiece (i.e., V'_w= 0 mm^3/mm), is plotted on the left portion of each graph.

The plotted graphs for the parameters N and $\bar{\sigma}_x$ feature an analogous trend for both the tangential and the axial scanning trajectories in the ground range from V'_w= 0 mm^3/mm up to V'_w= 200 mm^3/mm. Such trend is characterized by a substantial drop in the average values of N and $\bar{\sigma}_x$. The comparison between both scanning trajectories in this range shows that the means´ variances of N are considerably reduced when using the axial scanning trajectory than when running the tangential scanning trajectory. Moreover, it is also possible to notice that the slopes between the average values of N and $\bar{\sigma}_x$ are significantly higher for the axial scanning trajectory than for the tangential scanning trajectory.

In the ground range from V'_w= 200 mm^3/mm up to V'_w= 1200 mm^3/mm, the plotted graphs for both the parameter N and $\bar{\sigma}_x$ feature two different trends concerning the tangential and the axial scanning trajectories. The time domain results for the tangential scanning trajectory in this range show that no significant changes occur in the grinding wheel´s topography. On the other hand, the achieved results by means of the axial scanning trajectory point out that both time domain parameters increase (from V'_w= 200 mm^3/mm up to V'_w= 600 mm^3/mm) and subsequently tend to stabilize (from V'_w= 600 mm^3/mm up to V'_w= 1200 mm^3/mm). From V'_w= 200 mm^3/mm up to V'_w= 600 mm^3/mm the nearness of the N means´ variances leads to the fact that the variation in the topography is not as significant as observed in the previous range (i.e., from V'_w= 0 mm^3/mm up to V'_w= 200 mm^3/mm). From V'_w= 600 mm^3/mm up to V'_w= 1200 mm^3/mm the steady values of both N and $\bar{\sigma}_x$ permit to realize that the grinding wheel´s topography stays stabilized.

Aiming at gaining supplementary information about the variations in the grinding wheel´s topography taking effect during the experiments, the frequency domain analysis is implemented (i.e., PSD evaluation). The in-process PSD results gained with the frequency domain analysis

by employing the experimental condition "abc" (i.e., f_s= 400 kS/s, T.S= AE_{RAW}, T_h= high) are shown in Figure 62.

Figure 62 – In-process frequency domain outputs (AE Quick Test Method), second experiment series.
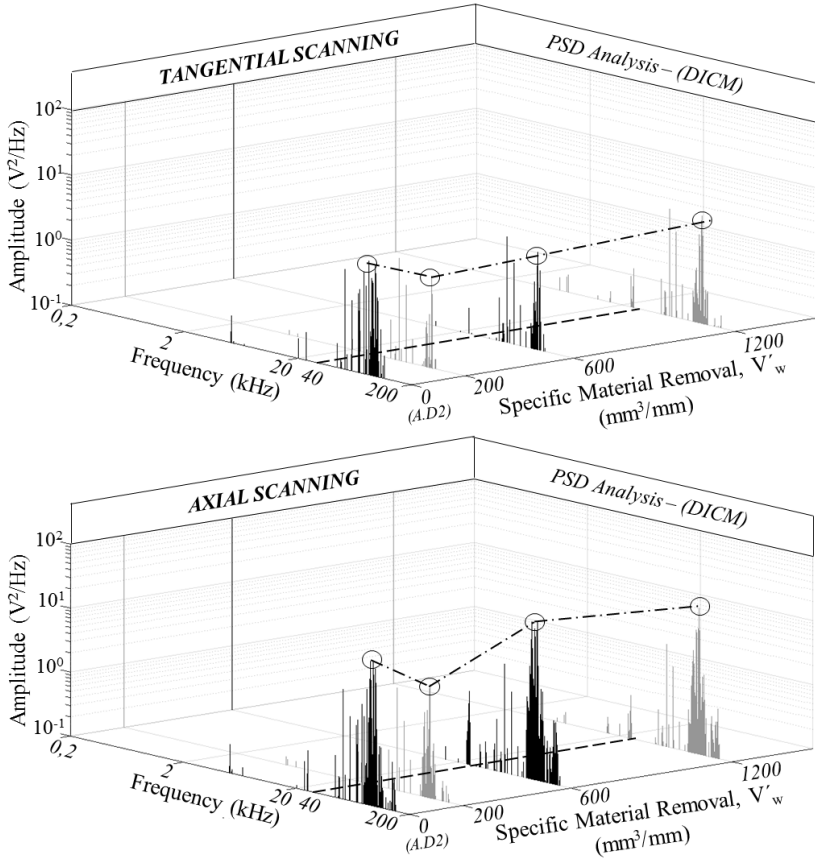
Source: (Developed by the author).

The graphs labelled as "0 (A.D2)" express the initial in-process condition of the grinding wheel, right after the second dressing process (D2) and before grinding the workpiece (i.e., $V´_w$= 0 mm³/mm), while the following graphs are computed in-process for each specific stage of the experiment series. These outputs are related to a predefined specific material removal $V´_w$ ground in the workpiece. The resulting PSD outputs derived from both scanning trajectories show that the maximum

frequency content is f_{max}= 200 kHz due to the used sampling rate f_s= 400 kHz.

For either scanning trajectories, the frequency domain signals present a similar trend as V'_w increases during the experiment series. In the range from V'_w= 0 mm^3/mm up to V'_w= 200 mm^3/mm, such a trend is characterized by a change in the AE_{RAW} spectrum, which shows a significant drop of the active frequencies in the high spectrum content above 40 kHz (dashed lines, Figure 62). Furthermore, in the range varying from V'_w= 600 mm^3/mm up to V'_w= 1200 mm^3/mm, the AE_{RAW} spectrum shows a noticeable stabilization.

The observation of the PSD´s magnitude (i.e., RMS level of the AE_{RAW} signals, Figure 62, circular markers) shows that a substantial drop occurs from V'_w= 0 mm^3/mm up to V'_w= 200 mm^3/mm when running both scanning trajectories (Figure 62, dash-dot lines connecting the circular markers). The RMS level of the AE_{RAW} signals obtained by means of the tangential scanning trajectory shows, however, a substantial difference in the grinding wheel´s topography does not occur between V'_w= 200 mm^3/mm and V'_w= 1200 mm^3/mm. On the other hand, the computed RMS level of the AE_{RAW} signals by using the axial scanning trajectory indicates that the grinding wheel´s topography changes in the range from V'_w= 200 mm^3/mm up to V'_w= 600 mm^3/mm and stays practically unchanged up to V'_w= 1200 mm^3/mm).

The achieved frequency domain results by means of both the tangential and axial scanning trajectories indicate that does exist substantial differences in the grinding wheel´s topography between V'_w= 0 mm^3/mm and V'_w= 200 mm^3/mm. These changes are more perceptible when running the axial scanning trajectory than by using the tangential scanning trajectory. In addition, the frequency results associated with both scanning trajectories point to a steady behaviour on the grinding wheel´s topography in the range from V'_w= 600 mm^3/mm up to V'_w= 1200 mm^3/mm.

The PSD outputs obtained in the range from V'_w= 0 mm^3/mm up to V'_w= 200 mm^3/mm exhibit an inverse tendency in the AE_{RAW} spectrum when compared with the previous in-process frequency domain outputs (i.e., first experiment series, Q'_w= 6 mm^3/mm.s). Such tendency verified in the AE_{RAW} spectrum is attributed to a drop of N_{kin} taking effect on the grinding wheel´s topography as V'_w gets higher. This assumption is validated in the next section (see Section 6.6).

6.6 DYNAMIC IN-PROCESS CHARACTERIZATION METHOD (DICM)´s VALIDATION

This section describes the procedures and measurements which have been executed for validating the achieved results of the AE Quick Test Method in the DICM. The validation of the results is based on the post-process evaluation of the specific grinding cutting force components (F'_n, F'_t) as well as on the analysis of the R_{ts} (actual grinding wheel surface roughness) derived from the Scratch Experiments.

6.6.1 Specific Grinding Cutting Force Components (F'_n, F'_t)

The validation of the results derived from the first experiment series employing the AE Quick Test Method relies initially on the evaluation of the specific grinding cutting force components (i.e., F'_n, and F'_t). This is carried out by processing the cutting force signals (i.e., F_x, F_y, F_z, and M_z) which are on-line acquired during the grinding process. Such evaluation occurs out of the grinding process, after finishing the Scratch Experiments, that is, it represents a post-process evaluation (Appendix D). Figure 63 shows the evaluated values of the specific grinding cutting force components F'_n and F'_t over V'_w related to the first experiment series (i.e., $Q'_w= 6$ mm^3/mm.s).

Figure 63 – Specific grinding cutting force components (F'_n, F'_t), first experiment series.
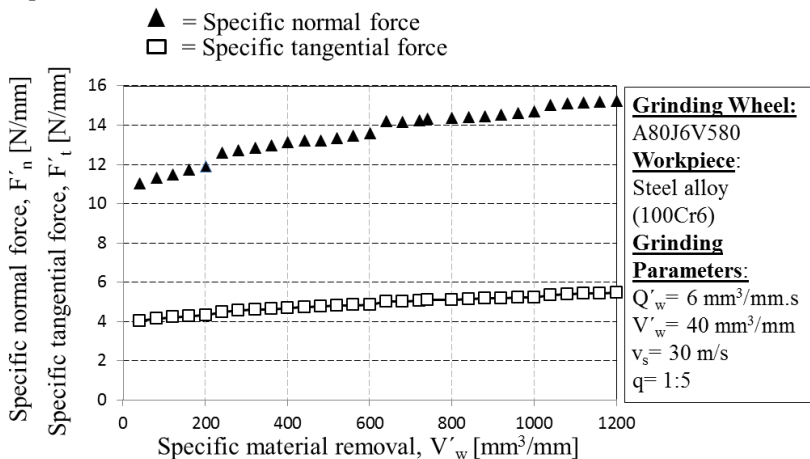
Source: (Developed by the author).

Each plotted point in Figure 63 represents the magnitude of the specific grinding cutting force components during the plunge movement of the grinding wheel onto the workpiece´s surface. It can be seen that both F'_n as well as F'_t increase with gradually enlarged values of V'_w. As all the grinding process input parameters are kept constant during the Scratch Experiments (with the exception of V'_w), the increasing trend observed in Figure 63 is associated with the overall growth of N_{kin} (i.e., number of kinematic cutting edges per surface area) for the investigated grinding wheel, (KLOCKE; KÖNIG, 2005; KÖNIG, 1989). Such trend correlates with the results found both in the time and frequency domains through the AE Quick Test Method in the first experiment series (see Figure 59 and Figure 60).

In the second experiment series, the topography of the grinding wheel is purposely changed by setting $Q'_w = 12$ mm^3/mm.s. The other grinding parameters are set to the same values as done before by the first experiment series. Figure 64 shows the post-process evaluated values of F'_n and F'_t over V'_w related to the second experiment series (i.e., $Q'_w = 12$ mm^3/mm.s).

Figure 64 – Specific grinding cutting force components (F'_n, F'_t), second experiment series.
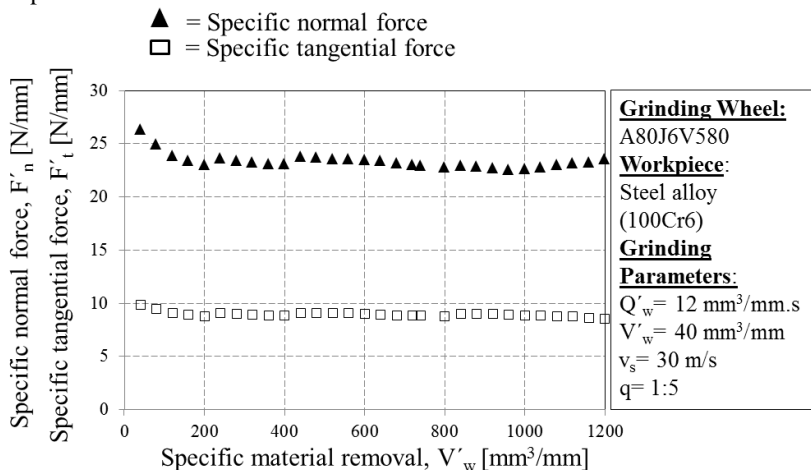
Source: (Developed by the author).

The plotted points in Figure 64 denote the magnitude of the specific grinding cutting force components which arise due to the plunge movement of the grinding wheel onto the workpiece. In the

range from $V´_w = 0$ mm^3/mm up to $V´_w = 200$ mm^3/mm a significant drop in both $F´_n$ and $F´_t$ is verified. From $V´_w = 200$ mm^3/mm up to $V´_w = 600$ mm^3/mm there is a slight increase in either specific grinding cutting force components. Although such increasing trend presents a less pronounced slope than the slope in the preceding range, the analysis of the absolute values of F_n and F_t reveals that these values are significantly distinct at $V´_w = 200$ mm^3/mm and at $V´_w = 600$ mm^3/mm. This is explained by the fact that the absolute difference in the values of both F_n and F_t is higher than the smallest detectable value that can be measured by the dynamometer (based on the parameter "threshold", see Section 2.7.1.1.2). The evaluated values of $F´_n$ and $F´_t$ in the range varying from $V´_w = 600$ mm^3/mm up to $V´_w = 1200$ mm^3/mm can be considered practically constant, as the absolute differences in the values of F_n and F_t lie in the limit of the smallest possible measurement variation that can be sensed by the dynamometer. Therefore, it is assumed that the topography of the grinding wheel in this range does not considerably vary, but rather stays practically unchanged.

As all the grinding process input parameters are kept constant during the Scratch Experiments (with the exception of $V´_w$), the decreasing trend observed in the range from $V´_w = 0$ mm^3/mm up to $V´_w = 200$ mm^3/mm in Figure 64 is associated with the overall drop of N_{kin} for the investigated grinding wheel. Such trend correlates with the results found both in the time and frequency domains through the AE Quick Test Method in the second experiment series (see Figure 61 and Figure 62).

6.6.2 Actual Grinding Wheel Surface Roughness (R_{ts})

In addition to the analyses of the main components of the grinding cutting force (see Section 6.6.1), the evaluation of the actual grinding wheel surface roughness (R_{ts}) has also been implemented. Such analysis occurs out of the grinding process, after finishing the Scratch Experiments, thus representing a post-process evaluation. Figure 65 shows the R_{ts} measurement results related to the first experiment series (i.e., $Q´_w = 6$ mm^3/mm.s).

Figure 65 – Actual grinding wheel surface roughness R_{ts}, first experiment series.
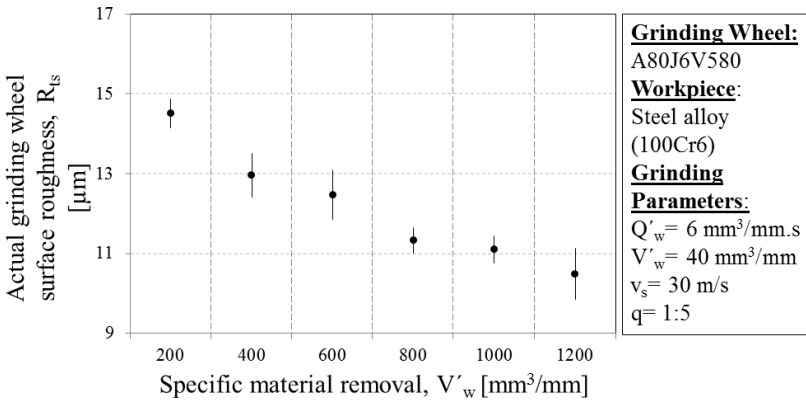
Source: (Developed by the author).

The centralized points plotted in Figure 65 correspond to the mean values based on 12 R_a roughness measurements in the predefined positions on the workpiece. The vertical straight lines in Figure 65 represent the spread of the R_a measurement results (i.e., means´ variances). It is observed that the R_{ts} mean values continuously decrease over gradually enlarged values of $V´_w$, thus indicating that more kinematic cutting edges are taking part in the grinding process. This tendency can also be explained by the fact that higher values of N_{kin} reduce h_{cu} (statistically average maximum underformed chip thickness) what in turn leads to smaller R_{ts} values evaluated on the workpiece (KLOCKE; KÖNIG, 2005; KÖNIG, 1989). Hence, such trend of the grinding wheel´s topography leads to the assumption that N_{kin} increases with higher values of $V´_w$ for the specific set of grinding parameters used in the Scratch Experiments. This trend also correlates with the previous grinding cutting force analysis as well as with the time and frequency domain results obtained through the AE Quick Test Method in the first experiment series.

In the second experiment series, the verified changes on the topography of the grinding wheel (i.e., due to $Q´_w = 12$ mm³/mm.s) can also be inferred from the roughness measurements on the workpiece. Figure 66 shows the R_{ts} measurement results related to the second experiment series (i.e., $Q´_w = 12$ mm³/mm.s).

Figure 66 – Actual grinding wheel surface roughness R_{ts}, second experiment series.
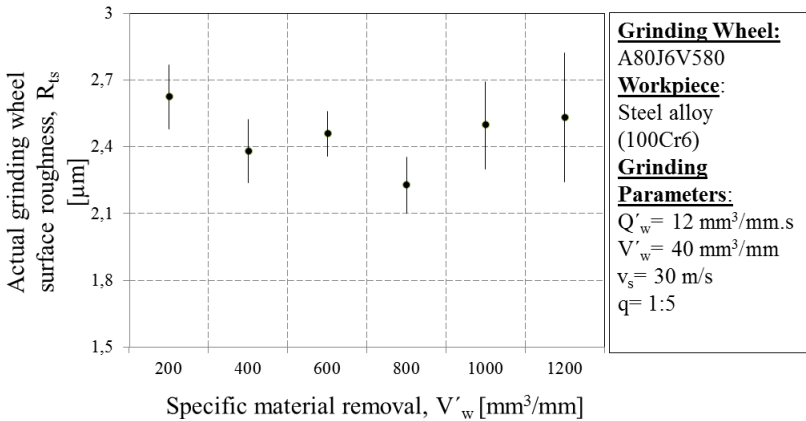
Source: (Developed by the author).

Each centralized point and vertical line shown in Figure 66 indicates, respectively, the mean value of the R_a roughness (n=12 measurements) and its variance. The comparison of the R_{ts} mean values associated with $V'_w = 200$ mm³/mm, $V'_w = 600$ mm³/mm and $V'_w = 1200$ mm³/mm indicates that initially a slight drop occurs when increasing the amount of ground material from $V'_w = 200$ mm³/mm up to $V'_w = 600$ mm³/mm. Afterwards, a stabilized behaviour on the topography of the grinding wheel is perceived between $V'_w = 600$ mm³/mm and $V'_w = 1200$ mm³/mm.

The initial drop observed in the mean values of R_{ts} (i.e., from $V'_w = 200$ mm³/mm up to $V'_w = 600$ mm³/mm) indicates that N_{kin} softly increases in this range, thus reducing h_{cu} and leading to reduced R_{ts} values on the workpiece at $V'_w = 600$ mm³/mm. This trend correlates with the previous grinding cutting force´s analysis (see Section 6.6.1) as well as with both the time and frequency domain results obtained in this range by using the AE Quick Test Method (see Section 6.5.2).

The stabilizing trend of the R_{ts} values between $V'_w = 600$ mm³/mm and $V'_w = 1200$ mm³/mm points out that no appreciable change in the topography of the grinding wheel takes effect when grinding the workpiece in this range. This tendency also matches the previous grinding cutting force analysis (see Section 6.6.1) and both the time and frequency domain results obtained during the second experiment series through the AE Quick Test Method (see Section 6.5.2).

6.7 ANALYSIS OF INFLUENCING FACTORS ON THE ACOUSTIC
EMISSION OVERSTEPS – N (TIME DOMAIN ANALYSIS)

By implementing a 2_{III}^{3-1} Fractional Factorial Analysis (i.e., 3
factors, each factor at 2 levels), an empirical model for both scanning
trajectories used in the AE Quick Test Method was achieved (Appendix
E). Such empirical model allows defining the experimental conditions
which optimize the grinding wheel´s characterization, by considering
the 3 influencing factors mentioned in the previous chapter (see Section
5.5.1, Table 13, and Appendix E). The Fractional Factorial Analysis
enables verifying the existing main effects and the interactions among
the factors´ levels (i.e., level high "↑", and level low "↓"), which have
been varied during the experiments. A main effect is present when the
mean of the response varies at the different levels of the factor
(MONTGOMERY, 2001). Main effects are only interpretable if the
interaction effects are not important. An interaction occurs when the
difference in response between the levels of one factor is not the same at
all levels of the other factors (MONTGOMERY, 2001). The input values
for the Fractional Factorial Analysis correspond to the AE oversteps,
(i.e., time domain parameter N, obtained in-process) derived from the
AE Quick Test Method along the first experiment series, after grinding
$V´_w = 600$ mm^3/mm. Based on these N values, the Fractional Factorial
Analysis is carried out as a post-process analysis (see Appendix E).

The optimized condition for both scanning trajectories is
associated with the factors combinations (and their respective levels)
which maximize N, while still maintaining the higher possible accuracy
of the proposed AE Quick Test Method. This optimization is based on
the increasing trend of N, verified in the range from $V´_w = 600$ mm^3/mm
up to $V´_w = 1200$ mm^3/mm (see Section 6.7.1, Figure 70, first
experiment series), which also represents the overall increasing trend of
N in the first experiment series. Further details about the optimization of
N are described in the following section (see Section 6.7.1).

Based on this analysis it was possible to evaluate the factors´
effects and the factors´ interactions that present the highest influence on
the response (i.e., AE oversteps, N). The first results regarding the 2_{III}^{3-1}
Fractional Factorial Analysis are represented by a Pareto chart showing
the absolute factors´ effects when employing both the tangential and the
axial scanning trajectories during the AE Quick Test Method, Figure 67.

Figure 67 – Pareto charts for the factors´ effects.
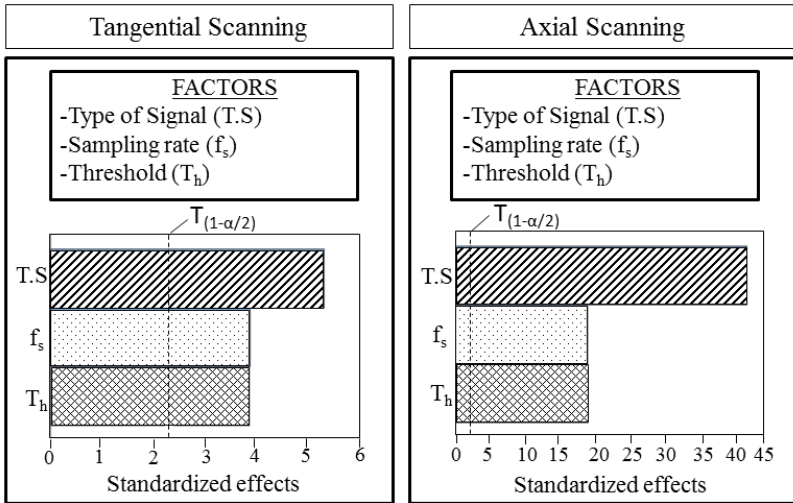
Source: (Developed by the author).

Both x-axes in Figure 67 express the values of the t-statistics (Student) for each factor and the reference line consists in the $(1-\alpha/2)$ quantile of a t-distribution, where $\alpha= 0,05$ (MONTGOMERY, 2001). The charts clearly show that the most influencing factor on N is the factor "Type of Signal" (T.S), because it farthest extends the reference line. Nevertheless, the isolated set of the factor T.S to its highest level does not guarantee an effective optimization of N. This is in addition justified by the fact that in a Fractional Factorial Analysis (2^{3-1}_{III}) each main effect is confounded (i.e., aliased) with two-factor interactions. That is, it is not possible to estimate all the factors´ effects separately without analyzing the existence and the influence of the two-factor interactions (MONTGOMERY, 2001). Therefore, the analysis of the two-factor interactions must be considered. Table 14 and Table 15 show additional obtained results through the proposed Fractional Factorial Analysis.

Table 14 – Fractional Factorial Analysis for the Tangential Scanning.

Factor	Effect	Coefficient	p-value
Constant		115788	0,001
Type of Signal (T.S)	- 228947	- 114474	0,001
Sampling rate (f_s)	166963	83482	0,005
Threshold (T_h)	- 166243	- 83121	0,005

Source: (Developed by the author).

Table 15 – Fractional Factorial Analysis for the Axial Scanning.

Factor	Effect	Coefficient	p-value
Constant		263269	0,000
Type of Signal (T.S)	- 483724	- 241862	0,000
Sampling rate (f_s)	220438	110219	0,000
Threshold (T_h)	- 221575	- 110788	0,000

Source: (Developed by the author).

The exposed results express that all the main effects exert significant influence on the achieved values of N, as their p-values are considerably smaller than the p-value defined previously to the experiments (i.e., $\alpha = 0,05$). This trend is practically the same for both scanning trajectories. By plotting the factors´ effects considered earlier (Table 14 and Table 15), it is noticed that the factors´ effects of either scanning trajectories exhibit a similar behaviour, Figure 68.

Figure 68 – Main effect plots for the response N (AE oversteps).
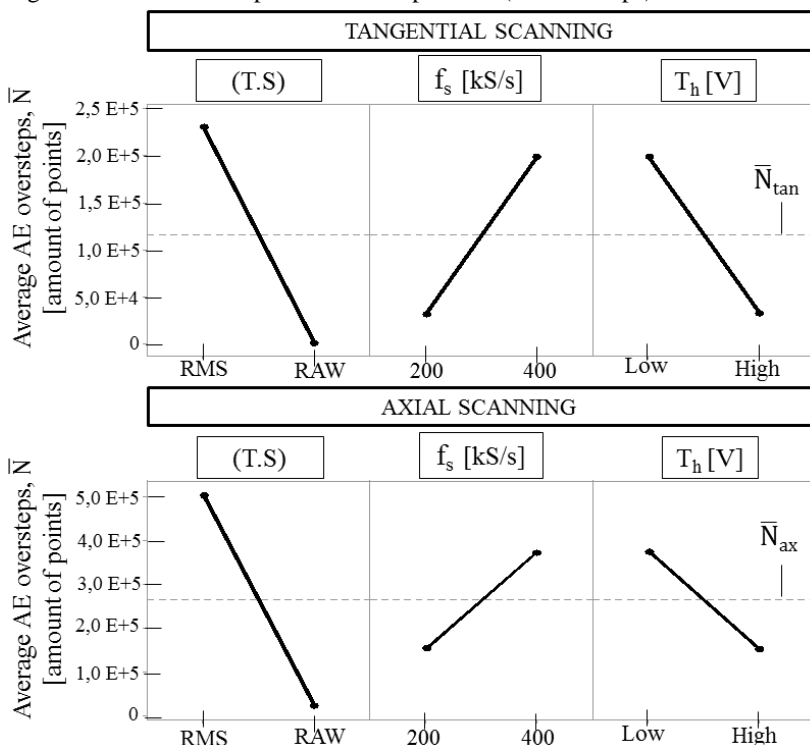
Source: (Developed by the author).

The analysis of the graphs also shows that the factor T.S yields the highest influence on the average values of N when employing both scanning trajectories.

This is represented by the pronounced slope between its low and high levels, (i.e., AE_{RMS} signal and AE_{RAW} signal, respectively) compared with the evaluated slopes for the other factors. Additionally, the effects of the factors f_s and T_h show a higher influence on the response N when using the tangential scanning trajectory than when employing the axial scanning trajectory.

Both y-axes in Figure 68 evidence the mean values of N ($\overline{N}$) which are calculated for each level of the factors. The horizontal dashed lines express the overall mean values of N (considering all the experimental runs and their replicates) obtained by means of either the tangential scanning trajectory ($\overline{N}_{tan}$) or through the axial scanning trajectory ($\overline{N}_{ax}$). The isolated observation of the main effect plots could occasionally lead to the false conclusion that the maximization of N is possible by just setting the factors T.S and T_h to their lower levels, and the factor f_s to its higher value. Nonetheless, as previously mentioned, one needs to verify the existence of interaction among the factors´ levels in order to extract reliable information about the optimized condition for maximizing N. Figure 69 shows the graphs for examining the interactions among the factors´ levels and their magnitudes.

Figure 69 – Interaction plots for the response N (AE oversteps).
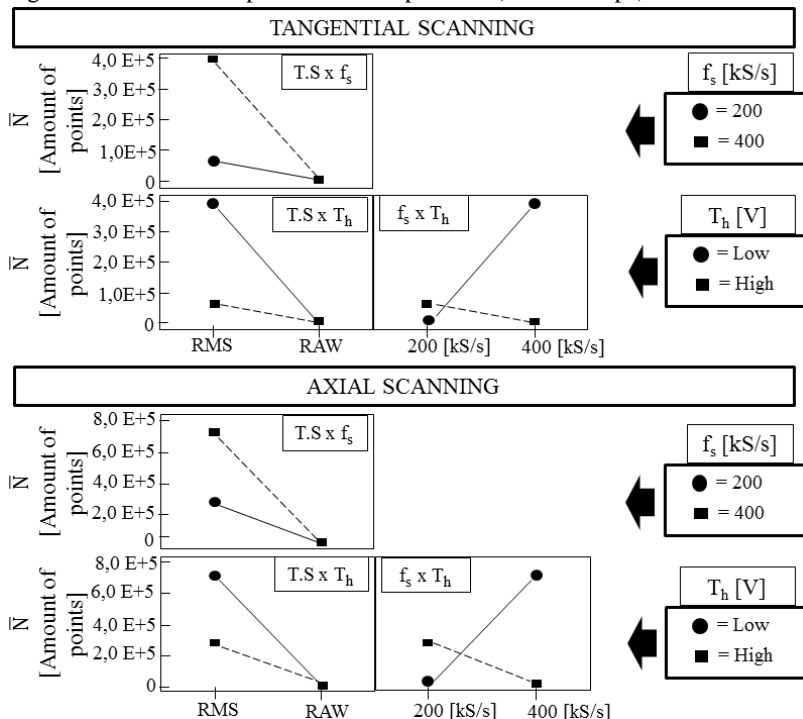
Source: (Developed by the author).

All the three possible combinations of the two-factor interactions obtained with both the tangential and the axial scanning trajectories are displayed. The analysis of the interaction plots for either scanning trajectories shows a very similar behaviour regarding the existing interactions among the factors´ levels. The magnitude of such interactions is considerably high, as there is substantial difference in the verified slope of the lines connecting the mean values of N between the factors´ levels in the interaction plots.

Especially for the interaction involving the factors f_s and T_h (i.e., interaction "f_s x T_h") it is noted that the magnitude of the interaction is higher than the existing interactions amid the other factors.

6.7.1 Optimization of the Time Domain Outputs (Regression Model through a 2_{III}^{3-1} Fractional Factorial Analysis)

By gathering the information obtained with the 2_{III}^{3-1} Fractional Factorial Analysis, it was possible to elaborate an empirical model which helps determining the optimized condition for the AE Quick Test Method. The model consists in a regression model which takes into account the coefficients shown in Table 14 and Table 15 as well as the two-factor interactions already mentioned. This model can be used to predict N over the experimental region (MONTGOMERY, 2001). Equation 15 and Equation 16 show the achieved empirical models for both the tangential and the axial scanning trajectories, respectively, (Appendix E).

$$N_{TAN} = 115788 - 114474\ (T.S) + 83482\ (f_s) - 83121\ (T_h) \qquad (15)$$

$$N_{AX} = 263269 - 241862\ (T.S) + 110219\ (f_s) - 110788\ (T_h) \qquad (16)$$

The term N_{TAN} in Equation 15 represents the average value of N by using the tangential scanning trajectory, whereas N_{AX} in Equation 16 denotes the average value of N when running the axial scanning trajectory during the experiments through the AE Quick Test Method. The independent variables T.S, f_s, and T_h in both equations represent the factors "Type of Signal", "Sampling rate", and "Threshold", respectively. The coefficients in both equations consist in the factors´ effects divided by 2, and the constant values C_{TAN}= 115788 and C_{AX}= 263269 are assigned to the overall mean of N (n= 12 experimental replicates), which are obtained while running both the tangential and the axial scanning trajectories, respectively (MONTGOMEY, 2001).

The optimized condition for both scanning trajectories is associated with the factor combinations (and their respective levels) which maximize N, while still maintaining the higher possible accuracy of the proposed AE Quick Test Method. This optimization is based on the increasing trend in the average values of N (over higher values of V´$_w$) verified in the first experiment series.

For optimizing the responses (N_{TAN} and N_{AX}) by means of the regression models, it is essential to consider the effect of the two-factor interactions on both N_{TAN} and N_{AX} equations. As in a 2_{III}^{3-1} Fractional Factorial Design the main effects are confounded with two-factor interactions, the coefficients of the factors in both Equation 15 and

Equation 16 also express the effects of the two-factor interactions, if these interactions are significant. The analysis of Figure 69 shows that the two-factor interactions do exist e must be considered for optimizing N in either scanning trajectories.

By analyzing the Equation 15 and Equation 16 it is observed that the coefficients of the factor T.S possess the highest absolute values. This also indicates that the associated two-factor interaction effect (i.e., interaction between f_s and T_h) is considerably high and significantly influences the response N. The further analysis of the coefficients related to the factors f_s and T_h permits to realize that the effect of the respective two-factor interactions are not negligible, as the sum of those coefficients equals the coefficients of the factor T.S in both equations.

Based on these considerations, the starting point for optimizing the responses (i.e., N_{TAN} and N_{AX}) consists in analyzing the interactions in which the factor T.S is present, as this factor exhibits the highest effect (see Figure 68). Next, the levels of the two-factor interactions are multiplied and the resulting signals are also multiplied by the coefficients´ signals. The high level of the factors (↑) receives the signal (+), whereas the low level of the factors (↓) is assigned to the signal (-). The resulting products should result in a positive signal in order to maximize the responses (MONTGOMERY, 2001). In this procedure, the factor T.S was set to its highest level (i.e., ↑= AE_{RAW} signal), as the AE_{RAW} signals have presented the better sensitivity over increased values of $V´_w$ by employing the AE Quick Test Method. This is justified by the higher slopes observed in the graphs of N x $V´_w$ when employing the AE_{RAW} signals in comparison with the slopes obtained by using the AE_{RMS} signals, Figure 70.

Figure 70 – Influence of the factor "Type of Signal" (T.S) on the response N
(AE oversteps) by employing the axial scanning trajectory.
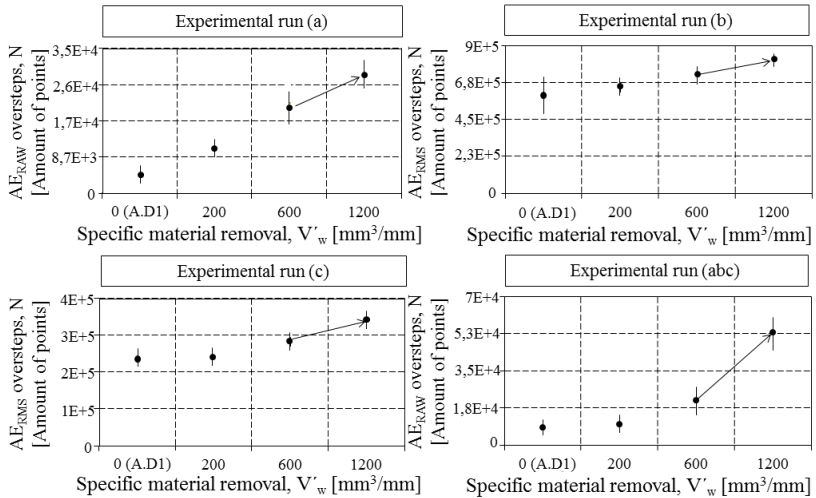
Source: (Developed by the author).

All the centralized points represent the mean values of N (n= 3
replicates) and the vertical bars symbolize the N means´ spreads. The
arrows connecting the N mean values show the increasing trend of N in
the considered experimental region. The N values are plotted for the
experimental runs 'a", "b", "c" and "abc", by using the axial scanning
trajectory. The same trend is verified when using the tangential scanning
trajectory.

The selection of the factor T.S to its high level (i.e., ↑= AE_{RAW}
signal) leads in turn to set the levels of the factors T_h and f_s to their ↑
and ↓ values, respectively. This set of the factors´ levels guarantees that
all the terms in both equations are positive, and therefore the responses
are maximized. Figure 71 summarizes the optimized settings of the
factors´ levels for both scanning trajectories.

Figure 71 – Optimized settings of the factors´ levels for both scanning trajectories.

REGRESSION MODEL (TANGENTIAL SCANNING)

$N_{TAN} = 115788 - 114474 \,(T.S) + 83482 \,(f_s) - 83121 \,(T_h)$ **(15)**

	FACTORS	LEVELS
Optimized condition	- Type of Signal (T.S) - Sampling Rate (f_s) - Threshold (T_h)	$T.S = \uparrow$ $f_s = \downarrow$ $T_h = \uparrow$

REGRESSION MODEL (AXIAL SCANNING)

$N_{AX} = 263269 - 241862 \,(T.S) + 110219 \,(f_s) - 110788 \,(T_h)$ **(16)**

	FACTORS	LEVELS
Optimized condition	- Type of Signal (T.S) - Sampling Rate (f_s) - Threshold (T_h)	$T.S = \uparrow$ $f_s = \downarrow$ $T_h = \uparrow$

Source: (Developed by the author).

7 CONCLUSIONS AND OUTLOOK

The achieved results in the scope of the current research show that the developed Dynamic In-process Characterization Method (DICM) is feasible for assessing in-process the topography of conventional grinding wheels. Such method affords fast in-process outputs (in both the time and frequency domains) which can be used to characterize the topography of conventional grinding wheels. By properly in-process controlling the topography of grinding wheels, additional benefits can be obtained. These, on the one hand, are related to an optimized use of the conventional grinding wheels by eliminating unproductive tasks concerning for example early redress of the tool. Such unproductive tasks are also generally related to unnecessary interruption of the grinding process, thus leading to the production standstill and hence to higher production costs. On the other hand, the possibility of in-process characterizing the topography of conventional grinding wheels as proposed by the DICM also allows maintaining process quality aiming to achieve a predefined working result on the ground parts.

The DICM is based on the prior development and validation of the Dynamic Post-process Characterization Method (DPCM) in which the characterization of the grinding wheel is only achieved out of the grinding process.

The results regarding the DPCM show that the time and the frequency domain analyses correlate among each other. Both analyses also correlate with the measuring results (i.e., roughness R_{ts}, thermally affected layer, SEM microscopy images, and replicas of the grinding wheel) and with the information available on the literature.

In the time domain, the results related to the parameters N e σ_x show an increasing trend over higher values of $V´_w$. This trend was the same when using both the tangential and the axial scanning trajectories.

In the frequency domain, on the other hand, the changes on the topography of the grinding wheel originate considerable variations in the AE spectrum. Such variations are represented by different dispersions in the content of the AE spectrum as well as by a rise of the AE energy (i.e., higher RMS level) as $V´_w$ gets higher. This pattern turned out to be similar for both scanning strategies (i.e., tangential and axial scanning trajectories).

By comparing the tangential and the axial scanning trajectories in terms of their achieved results (in both the time and frequency domains), one can affirm that both scanning trajectories are able to recognize the

changes on the grinding wheel´s topography. Nonetheless, in the course of the experiment series, the axial scanning trajectory has presented a better sensitivity than the tangential scanning trajectory. This suggests that both scanning trajectories should be employed complementarily in order to improve the topography characterization.

The tendencies derived from the analyses of the AE Tactile Scanning Experiments (in both the time and frequency domains for the axial and the tangential trajectories) and through the Scratch Experiments (in the frequency domain) are attributed to a rise of N_{kin} over higher values of $V´_w$ in both experiment series related to the DPCM. Additionally, the results of the measurements carried out on the workpieces and on the grinding wheel´s replicas show that the microtopography of the grinding wheel changes from a flat-like to a peak-like characteristic. Such trend indicates that the grinding wheel presents a pronounced friability while grinding the workpiece, thus generating sharped cutting edges over higher values of $V´_w$. The increasing trend of N_{kin} has also contributed to the improvement of the workpiece´s roughness which was evaluated after the experiment series by means of the roughness measurements.

The results connected with the utilization of the SOM-NN have shown that at least three appreciable classes of wear are derived from the Scratch Experiments regarding the DPCM. The possibility of obtaining such information without the need of a prior knowledge of the process and based on a set of input values representing the entire time-history of the Scratch Experiment signals (i.e., total duration= 1500 s) consists in a good result from such class of NN. Nonetheless, in the same way as the other post-process analyses used in the DPCM, it was time-consuming and could not be implemented in-process.

Based on the achieved results derived from the DPCM as well as on its proposed signal processing techniques, the DICM could be successfully implemented. This was carried out through the development and validation of the AE-based quick test method (AE Quick Test Method) which has enabled extracting in-process quantified information related to the grinding wheel´s topography.

The quantitative information is achieved in-process (i.e., same grinding setup and experimental rig) and instantaneously visualized on the laptop´s screen (when pushing the "stop" button of the signal acquisition program) after finishing the AE Tactile Scanning Experiments. Such versatility presented by the proposed AE Quick Test Method turns out to be the first main advantage of the method. Moreover, when comparing the AE Quick Test Method´s results with

other characterization methods presented in the literature, the proposed method allows to obtain quantified in-process information related to the topography of the grinding wheel by employing customary cutting speeds commonly used in industrial praxis (e.g., v_s= 30 m/s). Such information is obtained without the need for decreasing v_s, thus representing significant information related to the grinding process. The AE Quick Test Method permits to evaluate both time domain and frequency domain in-process parameters, in order to afford consistent information regarding the changes occurring in the grinding wheel´s topography throughout the experiment series.

The in-process outputs derived from both the time domain analysis (i.e., parameters N and σ_x) and the frequency domain analysis (i.e., PSD function) show that there exists a correlation between these outputs and the grinding cutting force components (F'_n and F'_t). In addition, both the time and frequency domain in-process outputs also correlate with the roughness parameter R_{ts} (related to both the first and the second experiment series) by using the tangential and the axial scanning trajectories.

When comparing the patterns related to the mean values of N ($\overline{N}$) and σ_x ($\overline{\sigma_x}$) with the in-process PSD outputs, it is noticed a correlation among those analyses for both the tangential and the axial scanning trajectories throughout the experiment series.

In the first experiment series regarding the DICM, the obtained time and frequency domain results correlate with both the post-process measurements (i.e., F'_n, F'_t, and R_{ts}) and with the results related to the DPCM. The increasing trend verified in the time domain outputs is associated with a rise of N_{kin} over higher V'_w values, which is also confirmed by analyzing the results extracted from the Scratch Experiments. The frequency domain results point out that a remarkable tendency in the AE_{RAW} spectrum occurs when increasing the amount of V'_w in the course of the first experiment series. This tendency is characterized by a significant change in the AE spectrum distribution, which exhibits a significant growth in the high frequency content (i.e., above 40 kHz), as V'_w gets higher. This permits to distinguish in-process both the initial condition and the final condition of the grinding wheel´s topography. In addition, the evaluation of the magnitude of the AE_{RAW} spectrum (i.e., the RMS level) also shows an increasing trend as V'_w assumes higher values. The difference in the RMS level of the AE_{RAW} spectrum verified in the range varying from V'_w= 600 mm³/mm up to V'_w= 1200 mm³/mm suggests that considerable changes in the grinding wheel´s topography occur, while from V'_w= 0 mm³/mm up

V'_w= 200 mm^3/mm no appreciable changes take effect. These results also correlate with the results achieved by means of the time domain analysis, and can also be associated with a growth of N_{kin} over increased values of V'_w in the course of the first experiment series.

In the second experiment series concerning the DICM, the different characteristic of the grinding wheel´s topography was also recognized by means of the time and the frequency domain outputs. In the range varying from V'_w= 0 mm^3/mm up to V'_w= 200 mm^3/mm the time domain outputs show a substantial drop which also correlates with the grinding cutting force measurements related to the Scratch Experiments. On the other hand, the PSD outputs present an inverse trend both in the AE spectrum dispersion and in the AE RMS level (i.e., spectrum magnitude). Such inverse trend correlates with the time domain outputs and are associated with a drop of N_{kin} in this experimental range. In the experimental range varying from V'_w= 600 mm^3/mm up to V'_w= 1200 mm^3/mm both the time domain and the frequency domain outputs show no significant changes. This is due to a constant topography of the grinding wheel which has also matched the Scratch Experiments´ results by means of the grinding cutting force analysis (i.e., F'_n and F'_t) and the R_{ts} measurements.

A further comparison between the obtained results (time and frequency domains) by using the tangential and the axial scanning trajectories regarding the DICM experiments shows that both scanning trajectories are feasible to detect the variations occurring in the grinding wheel´s topography over the experiment series (in both the first and second experiment series). Nevertheless, the axial scanning trajectory has presented a higher sensitivity and accuracy than the tangential scanning trajectory, being able to recognize small variations in the grinding wheel´s topography and totally dissimilar conditions on the surface of the grinding wheel. This is confirmed by observing the R_{ts} values in the range from V'_w= 200 mm^3/mm up to V'_w= 600 mm^3/mm (R_{ts}= 2 µm) as well as in the range varying from V'_w= 200 mm^3/mm up to V'_w= 1200 mm^3/mm (R_{ts}= 4 µm), related to the first experiment series. These results point out that both scanning trajectories should be used complementarily aiming at obtaining reliable information about the topography of the grinding wheel. The use of both scanning trajectories in-process consists in a possible alternative, as the scanning trajectories and the derived outputs are not time-consuming, demanding nearly 5 s each to be implemented, after defining the reference position on the periphery of the grinding wheel.

The proposed values for the scanning depths ($a_{e,scan}$) employed for both the tangential scanning trajectory ($a_{e,scan\_tan}$= 2 µm) and the axial scanning trajectory ($a_{e,scan\_axial}$= 1 µm) were suitable in terms of getting a measurable AE signal during the experiments. At the same time, the $a_{e,scan}$ values did not provoke any damage neither on the grinding wheel´s topography nor in the single-point diamond tip, thus enabling the evaluation of the topography of the grinding wheels in the elastic deformation range. This has been proved to be true by comparing the initial profile of the single-point diamond tip (evaluated by microscopy previously to the experiments) with the final profile of the single-point diamond tip after finishing the experiment series regarding the DICM. By the end of the experiment series, a total of 192 AE signals have been measured which were derived from the replicated experimental runs (i.e., sample size, n= 3 replicates) by using both scanning trajectories. As in each experiment stage a total of 12 replicates are obtained consecutively for each individual scanning trajectory, and the AE signals present similar amplitude among each other, it is possible to affirm that the elastic deformation range is not exceeded.

The transducer-fusion technique utilized during the DICM and involving the acquisition of AE signals and Force signals has proved to be efficient in terms of obtaining reliable information related to the grinding wheel´s topography. Such technique improves signal analysis and signal interpretation and avoids ambiguities or signal misinterpretations which commonly happen when analyzing only one isolated process characteristic.

7.1 OUTLOOK

Taking into consideration all the exposed results regarding the Dynamic In-process Characterization Method (DICM), further investigations in the grinding process are encouraged and suggested as follow:

7.1.1 Running the Dynamic In-process Characterization Method (DICM) in a Production Environment (Industrial Application)

The experimental runs carried out during the current research have been investigated under a well-controlled laboratorial environment, free of the most common disturbances that exist in a production environment. Therefore, further investigations of the effectiveness of the

proposed method in a normally noisy production environment would be a challenge and required task to be accomplished.

7.1.2 Investigating the Dynamic In-process Characterization Method (DICM) for Superabrasive Grinding Wheels and Higher Cutting Speeds

The ever increasing trend in grinding for using superabrasive grinding wheels aiming to grind difficult-to-cut materials and to reduce costs regarding redress of the tools demands additional investigations of the DICM for superabrasive materials. As the utilization of superabrasive grinding wheels is also connected with higher v_s values (due to advantages concerning tool wear and grindability), further investigations of the DICM should also take into account the effectiveness of the method for considerably higher v_s values used in industry, i.e., up to $v_s= 100$ m/s.

7.1.3 Integrating the Contact Recognition Procedure into the Dynamic In-process Characterization Method (DICM)

The precise determination of the first contact between the grinding wheel and the single-point diamond tip plays an important role on the effectiveness of the DICM. In the course of the current research it was not possible to integrate both the DICM and the contact recognition procedure (as presented by the DPCM in this research) due to limited time resources. The precise definition of the first contact is a time-consuming activity which also leads to a significant degree of variation if not correctly controlled. Hence, further improvements of the DICM should also consider this topic.

7.1.4 Evaluating Broader AE Frequency Ranges during the AE Tactile Scanning Experiments regarding the Dynamic In-process Characterization Method (DICM)

The spectral content of AE signals in grinding is not yet well defined and covers a wide range which can vary from for example 100 Hz up to 1000 kHz. The experiments carried out in this research have shown that appreciable information is gained by properly analyzing higher spectral contents of the AE signal (i.e., $f_{max}= 100$ kHz during the DPCM´s experiments, $f_{max}= 200$ kHz during the DICM´s experiments). This relies on the correct choice of components in the signal condition

chain (i.e., transducers, analog high-pass filters, analog low-pass filters, etc.) in order to avoid unwanted disturbances on the acquired AE signals and to allow extracting useful information from the digitized signals.

7.1.5 Investigating Additional Signal Processing Techniques on Digitized AE$_{RAW}$ Signals

The signal processing techniques employed in the scope of the current research were able to characterize the topography of the conventional grinding wheels both out of the grinding process (DPCM) and in-process (DICM). Additional techniques to those mentioned in this research should be investigated in order to improve process knowledge and to afford a better use of the conventional grinding wheels.

REFERENCES

AGUIAR, P. R.; SERNI, P. J. A.; BIANCHI, E. C.; DOTTO, F. R. L. In process grinding monitoring by acoustic emission. **Journal of the Brazilian Society of Mechanical Sciences and Engineering,** 2006.

AKBARI, J.; SAITO, Y.; HANAOKA, T.; HIGUCHI, S.; ENEMOTO, S. Effect of grinding parameters on acoustic emission signals while grinding ceramics. **Journal of Material Processing Technology**, 1996.

ALICONA INFINITE FOCUS. **Infinite focus hardware IFM G4 3.5**. 2009.

ALICONA INFINITE FOCUS. **Technical specification**. Available at: < www.alicona.com >, Access: November/2010.

AMBROSIUS, E. E.; FELLOWS, D. R.; BRICKMANN, D. A. **Mechanical measurement and instrumentation:** Part II dynamic measurements. Pennsylvania State University: Ronald Press Company, 2009.

BASERI, H. Modeling of grinding wheel sharpness by using neural network. **International Conference on Computer Systems and Technologies**, Sofia, June 2010.

BDG: BUNDESVERBAND DER DEUTSCHEN GIEβEREI INDUSTRIE. **Gusseisen mit Kugelgraphit:** Herstellung, Eingeschaften, Anwendung. 2007.

BENDAT, S. J.; PIERSOL, G. A. **Random data:** Analysis and measurement procedures. California: [s.n.], 1971.

BIFANO, T. G.; YI, Y. Acoustic emission as an indicator of material-removal regime in grass micro-machining. **Journal of the American Society for Precision Engineering**, v.14, p. 219-228, Oct. 1992.

BOARON, A. **Determinação do posicionamento relativo entre rebolo e peça com o auxílio da emissão acústica**. 2009. 151 f. Dissertação (Mestrado em Engenharia Mecânica) - Universidade Federal de Santa Catarina, Florianópolis, 2009.

BOARON, A.; WEINGAERTNER, W. L.; MARTINENGUI, G. Aplicação industrial do reconhecimento de contato entre rebolo e peça. **Revista Máquinas e Metais - MM**, v. 550, p. 50-71, nov. 2011.

BOARON, A.; WEINGAERTNER, W. L. Determination of the relative position between grinding wheel and a cylindrical workpiece on a 7 axis grinding machine by using acoustic emission. **Journal of the Brazilian Society of Mechanical Sciences and Engineering**, Rio de Janeiro, v. 34, n.1, p. 24-31, Mar. 2012a.

BOARON, A.; WEINGAERTNER, W. L.; UHLMANN, E. A quick-test method based on acoustic emission for the in-process characterization of conventional grinding wheels. **58th IWK Ilmenau Scientific Colloquium: Shaping the Future by Engineering**, Technische Universität Ilmenau, Ilmenau, p.1-15. Sept. 2014.

BRAGA, A. P.; CARVALHO, A. P. L. F.; LUDERMIR, T. B. **Redes neurais artificiais:** Teoria e aplicações. Rio de Janeiro: LCT, 2000.

BRINKSMEIER, E.; HEINZEL, C.; MEYER, L. Development and application of a wheel based process monitoring system in grinding. **Annals of CIRP - Manufacturing Technology**, 2005.

BYRNE, G.; DORNFELD, D. A.; INASAKI, I.; KETTELER, G.; KÖNIG, W.; TETI, R. Tool condition monitoring (TCM): The status of research and industrial application. **Annals of CIRP**, v.4, p.541-567, 1995.

CAI, R.; ROWE, W. B.; MORGAN, M. N.; MILLS, B. Measurement of vitrified CBN grinding wheel topography. **Key Engineering Materials**, 2003.

CERTI. **Relatório de medição**. Universidade Federal de Santa Catarina (UFSC), Abril 2012.

CHEN, X.; LIMCHIMCHOL, T. Monitoring grinding wheel redress-life using support vector machines. **International Journal of Automation and Computing**, 2006.

DAVIS, J.R.(Ed.); LAMPMAN, S.R. (Ed.); ZORC, T.B. (Ed.); FRISSEL, H.J. (Ed.); CRANKOVIC, G.M. (Ed.); RONKE, A.W. (Ed.); KEEFE, K.L. (Ed.); PATITSAS, J. (Ed.); ABEL, L.A. (Ed.); KIEPURA, R.T. (Ed.); THOMAS, P. (Ed.); WHEATON, N.D. (Ed.); STEDFELD, R.L(Ed.). **ASM Handbook-machining**. 9th ed. [S.I]: ASM International, 1995, v. 16.

DIMLA, E. Sensor signals for tool-wear monitoring in metal cutting operations: A review of methods. **International Journal of Machine Tools and Manufacture**, p.1073-1078, 2000.

DEUTSCHES INSTITUT FÜR NORMUNG. **DIN 4768:** Ermittlung der Rauheitskenngröβen mit elektrischen Tatschnittgeräten - Begriffe und Meβbedingungen. 1990.

DEUTSCHES INSTITUT FÜR NORMUNG. **DIN 8589-11:** Fertigunsverfahren Spanen: Schleifen mit rotierendem Werkzeug - Einordnung, Unterteilung, Begriffe. 2003.

DEUTSCHES INSTITUT FÜR NORMUNG. **DIN EN ISO 25178-2:** Geometrische Produktspezifikation (GPS) – Oberflächenbeschaffenheit Flächenhaft: Begriffe und Oberflächen-Kenngrößen. 2008.

DORNFELD, D.; LEE, D. **Precision manufacturing**. New York: Springer, 2008.

DUSCHA, M.; KLOCKE, F.; WEGNER, H. Erfassung und Charakterisierung der Schleifscheibentopographie für die anwendungsgerechte Prozessauslegung. **Diamond Business,** 2009.

HEWLETT PACKARD. **The fundamentals of signal analysis**: Application Note 243. 1994.

FIGLIOLA, R. S.; BEASLEY, D. E. **Theory and design for mechanical measurements.** 3rd ed. New York: John Wiley & Sons Inc., 2000.

GAUTSCHI, G. **Piezoelectric sensorics**. Berlin: Springer, 2001.

GERGES, S. N. Y. **Processamento e análise de sinais de acústica e vibrações**. Universidade Federal de Santa Catarina, Florianópolis, 2006.

GOMES, J. J. F. **Identificação em processo de mecanismos de desgaste de rebolos**. 2001. 131 f. Tese (Doutorado em Engenharia Mecânica) - Universidade de São Paulo, Escola de Engenharia de São Carlos, São Carlos, 2001.

GOVINDHASAMY, J. J.; MCLOONE, S. F.; IRWIN, G. W.; FRENCH, J. J.; DOYLE, R. P. Neural modelling control and optimization of an industrial grinding process. **Elsevier Science – Control Engineering Practice**, Oct. 2005.

HASSUI, A.; DINIZ, A.E.; OLIVEIRA, J.F.G.; FELIPE, J.; GOMES, J.J.F. Experimental evaluation on grinding wheel wear through vibration and acoustic emission. **Wear - Elsevier Science**, Feb. 1998.

HWANG, T.W.; WHITENTON, E.P.; HSU, N.N.; BLESSING, G.V.; EVANS, C.J. Acoustic emission monitoring of high speed grinding of silicon nitride. **Elsevier Science**, 2000.

INASAKI, I. Application of acoustic emission sensor for monitoring machining process. **Elsevier Science – Ultrasonics**, p.273-281, 1998.

INASAKI, I. Sensor fusion for monitoring and controlling grinding process. **The International Journal of Advanced Manufacturing Technology**, Londres, 1999.

JENOPTIK GROUP; HOMMEL-ETAMIC NANOSCAN 855. **Oberflächenmessung:** Messbedingungen. 2008.

JENOPTIK GROUP; HOMMEL-ETAMIC NANOSCAN 855. **Roughness and contour measurement with maximum precision**. 2009.

JU, K.; KIM, H.; HONG, S. Monitoring of grinding wheel wear in surface grinding process by using laser scanning micrometer. **International Journal of the Korean Society of Precision Engineering**, v.2, n.1, 2001.

KARPUSCHEWSKI, B. Sensoren zur Prozessüberwachung beim Spanen. **Fortschrittsbericht VDI Reihe 2**, n. 581. Düsseldorf: VDI-Verlag, 2001.

KIRCHGATTER, M. **Einsatzverhalten genuteter CBN-Schleifscheiben mit keramischer Bindung beim Außenrund-Einstechschleifen**. 2010. 153 f. Thesis (Doktor der Ingenieurwissenschaften) - Technischen Universität Berlin, Berlin, 2010.

KISTLER INSTRUMENT CORPORATION. **Acoustic emission:** Piezotron coupler Type 5125B. 2006.

KISTLER INSTRUMENT CORPORATION. **Acoustic emission sensor:** Type 8152B. 2007.

KISTLER INSTRUMENT CORPORATION. **Rotating 4-component dynamometer RCD**: Type 9124B. 2008.

KISTLER INSTRUMENT CORPORATION. **Instruction manual:** Rotating cutting force dynamometer Type 9123C. 2010.

KLOCKE, F.; KÖNIG, W. **Fertigungsverfahren – band 2:** Schleifen, Honen, Läppen. 4. Aufl. Berlin: Springer Verlag, 2005.

KLUFT, W. **Process monitor GD 200, G200 und D200**. Aachen, 1989.

KÖNIG, W. **Fertigungsverfahren band 2**: Schleifen, Honen, Läppen. 2. Aufl. Düsseldorf, 1989.

KÖNIG, W.; MEYEN, H. P. AE in grinding and dressing: Accuracy and process reliability. **Society of Manufacturing Engineers: 4th International Grinding Conference**, Oct. 1990.

KÖNIG, W.; ALTINTAS, Y.; MEMIS, F. Direct adaptive control of plunge grinding process using acoustic emission (AE) sensor. **Institute of Machine Tools and Production Engineering (WZL)**, Aachen, July 1994.

KWAK, J.; HA, M. Neural network approach for diagnosis of grinding operation by acoustic emission and power signals. **Journal of Materials Processing Technology**, p. 65-71, Nov. 2003.

LACHANCE, S.; WARKENTIN, A.; BAUER, R. Development of an automated system for measuring grinding wheel wear flats. **Journal of Manufacturing Systems,** v. 22, n. 2, p.130–135, 2003.

LAPPORT SCHLEIFTECHNIK GMBH. **Lagerliste Scheiben**. 2010.

LEE, D. E.; HWANG, I.; VALENTE, C.M.O.; OLIVEIRA, J.F.G.; DORNFELD, D.A. Precision manufacturing process monitoring with acoustic emission. **International Journal of Machine Tools and Manufacture**, 2005.

LEME, S.P.L. **Dressamento por toque de rebolos de CBN**. 1999. Dissertação (Mestrado em Engenharia Mecânica) - Universidade Federal de Santa Catarina, Florianópolis, 1999.

LIAO, T. W. A wavelet-based methodology for grinding wheel condition monitoring. **International Journal of Machine Tools and Manufacture**, p. 580-592, 2007.

LIAO, T. W. Feature extraction and selection from acoustic emission signals with an application in grinding wheel condition monitoring. **Journal Engineering Applications of Artificial Intelligence**, 2010.

LINKE, S. B. **Wirkmechanismen beim Abrichten keramisch gebundener Schleifscheiben**. 2007. 147 f. Thesis (Doktorin der Ingenieurwissenschaften) - Rheinisch Westfälischen Technischen Hochschule, Aachen, 2007.

LIU, Q.; CHEN, X.; GINDY, N. Fuzzy pattern recognition of AE signals for grinding burn. **International Journal of Machine Tools and Manufacture**, v. 45, n. 8, p. 811-818, 2005.

MAHR DO BRASIL LTDA. **Parâmetros de rugosidade**. São Paulo, Available at: < http://www.mahr.com>. Access: November/2011.

MALKIN, S.; GUO, C. **Grinding technology:** Theory and applications of machining with abrasives. 2nd ed. 2008. Available at: < http://books.google.com.br >. Access: May/2014.

MARGOT, R. D. Y. **Strategische Signalerfassung mit piezoelektrischen Sensoren für die Prozessüberwachung in der Zerspanung**. 2005. 149 f. Thesis (Doktor der Wissenschaften) - Eidgenössichen Technischen Hochschule Zürich, Zurïch, 2005.

MARINESCU, I. D.; HITCHINER, M.; UHLMANN, E.; ROWE, W. B.; INASAKI, I. **Handbook of machining with grinding wheels**. USA: CRC Press Taylor & Francis Group, 2007.

MEHROTRA, K.; MOHAN, C. K.; RANKA, S. **Elements of artificial neural networks**. [S.I.:s.n.], 1996.

MOKBEL, A. A; MAKSOUD, T.M.A. Monitoring of the condition of diamond grinding wheels using acoustic emission technique. **Journal of Materials Processing Technology**, v. 101, n. 1-3, p. 292-297, 2000.

MONTGOMERY, D. C. **Design and analysis of experiments**. 5th ed. Arizona State University: John Willey & Sons Inc., 2001.

NATIONAL INSTRUMENTS. **Labview signal processing course manual:** Edition Part Number 321569A-01. 1997.

NATIONAL INSTRUMENTS. **NI 625x specifications**. 2004.

NATIONAL INSTRUMENTS. **Installation guide**: BNC-2110. 2007.

NATIONAL INSTRUMENTS. **DAQ M series**: M Series User Manual NI 622x NI 625x and NI 628x Devices. 2008.

NATIONAL INSTRUMENTS. **Labview help tutorial**. 2010.

NATIONAL INSTRUMENTS. **Datasheet:** Type 621x. 2012.

OLIVEIRA, J. F. G.; DORNFELD, D. A. Application of AE contact sensing in reliable grinding monitoring. **Annals of CIRP**, v.1, 2001.

PATHARE, S.; GAO, R.; VARGHESE, B. A DSP-based telemetric data acquisition system for in-process monitoring of grinding operation. **IEEE Instrumentation and Measurement Technology Conference**, Minesota, 1998.

QI, H. S.; ROWE, W. B.; MILLS, B. Experimental investigation of contact behavior in grinding. **Tribology International**, 1997.

RAVINDRA, H. V.; SRINIVASA, Y. G.; KRISHNAMURTHY, R. Acoustic emission for tool condition monitoring in metal cutting. **Department of Mechanical Engineering, Indian Institute of Technology,** India, June 1997.

REHSTEINER, F.; KUSTER, F.; HUNDT, W. Model-based AE monitoring of the grinding process. **Annals of CIRP**, v. 46/1, 1997.

ROISENBERG, M. **Tópicos especiais em aplicações tecnológicas I**. Departamento de Informática e Estatística, mar. 2011. Notas de aula.

ROWE, W. B.; MARINESCU, I. D.; DIMITROV, B.; INASAKI, I. **Tribology of abrasive machining processes**. USA: William Andrew, 2004.

ROWE, W. B. **Principles of modern grinding technology**. 1st ed. Oxford: William Andrew, 2009.

SCHAUDT GMBH. **PF 51 Universal cylindrical grinding machine:** Technical manual. Available at: < www.schaudt.com >, Access: November 2010.

SCHÜHLI, L. A. **Monitoramento de operações de retificação usando fusão de sensores**. 2007. 119 f. Dissertação (Mestrado em Engenharia de Produção Mecânica) - Universidade de São Paulo, Escola de Engenharia de São Carlos, São Carlos, 2007.

SENSIS IND. COM. EQUIPAMENTOS ELETRÔNICOS LTDA. **Manual de operação do sistema de monitoramento MSM**. São Carlos, 2002.

SHIN, K.; HAMMOND, J. K. **Fundamentals of signal processing for sound and vibration engineers**. Chichester: John Wiley & Sons Ltd., 2008.

SMITH, S. W. **The scientist and engineer´s guide to digital signal processing**. 2nd ed. [S.I]: California Technical Publishing, 2003.

SOUZA, A. J. **Aplicação de multisensores no prognóstico da vida da ferramenta de corte em usinagem**. 2001. 211 f. Tese (Doutorado em Engenharia Mecânica) - Universidade Federal de Santa Catarina, Florianópolis, 2001.

SPUR, G.; STÖFERLE, T. **Handuch der Fertirgungstechnik:** Band 3/2 Spanen. München, 1980.

SUSIC, E.; GRABEC, I. Characterization of the grinding process by acoustic emission. **International Journal of Machine Tools and Manufacture**, p. 225-238, 2000.

TAYLOR, J. S.; PISCOTTY, M. A.; DORNFELD, D. A.; BLAEDEL, K. L.; WEAVER, L. F. Investigation of acoustic emission for use as a wheel-to-workpiece proximity sensor in fixed-abrasive grinding. **Energy Citation Database**, Sept. 1995.

TÖNSHOFF, H. K.; FRIEMUTH, T.; BECKER, J. C. Process monitoring in grinding. **Annals of CIRP – Manufacturing Technology**, v.51, n.2, 2002.

VARGHESE, B.; PATHARE, S.; GAO, R.; GUO, C.; MALKIN, S. Development of a sensor-integrated "intelligent" grinding wheel for in-process monitoring. **Annals of CIRP**, 2000.

WEBSTER, J.; DONG, W. P.; LINDSAY, R. Raw acoustic emission signal analysis of grinding process. **Annals of CIRP**, Center for Grinding Research and Development, University of Connecticut, v. 45, p. 335- 340, Jan. 1996.

WEINGAERTNER, W. L.; BOARON, A. A quick-test method to determine the grinding wheel topography based on acoustic emission. **Advanced Materials Research**, Sttutgart, v.14, p. 282-288, Sept. 2011.

WEINGAERTNER, W. L.; BOARON, A. A method to determine the grinding wheel's topography based on acoustic emission. **International Journal of Abrasive Technology**, v.5, n.1, p.17-32, Apr. 2012b.

XIAOQI, C.; HAO, Z.; WILDERMUTH, D. In-process tool monitoring through acoustic emission sensing. **SIMTech Technical Report, Singapore Institute of Manufacturing Technology,** 2001.

ZEMA ZSELICS LTDA. **Manual de operação**. 2002.

ZIMMERMANN, S. **Systematische Untersuchungen zum Leistungspotenzial strukturierter Schleifwerkzeuge**. 2013. 93 f. Diplomarbeit (Ingenieurwissenschaften) - Institut für Werkzeugmaschinen und Fabrikbetrieb, Technische Universität Berlin, Berlin, 2013.

APPENDIX A – Mounting and Clamping of the Workpiece During Scratch Experiments Regarding the Dynamic In-process Characterization Method (DICM)

The mounting of the workpiece throughout the Scratch Experiments regarding the DICM occurs by means of a cylindrical mounting support, Figure A.1. Before running the Scratch Experiments, each workpiece is mounted on the appropriate cylindrical surface of the mounting support (Figure A.1, surface A, diameter $\emptyset_A$). Next, the workpiece is clamped by using both a ring and a round nut, which are mounted on the cylindrical surface B (diameter $\emptyset_B$) and on the cylindrical surface C (diameter $\emptyset_C$), respectively, Figure A.1. The fastening of the workpiece on the cylindrical mounting support is carried out by applying a torque on the round nut.

Figure A.1 – Schematic representation of mounting and clamping of the workpiece during the Scratch Experiments regarding the Dynamic In-process Characterization Method (DICM).
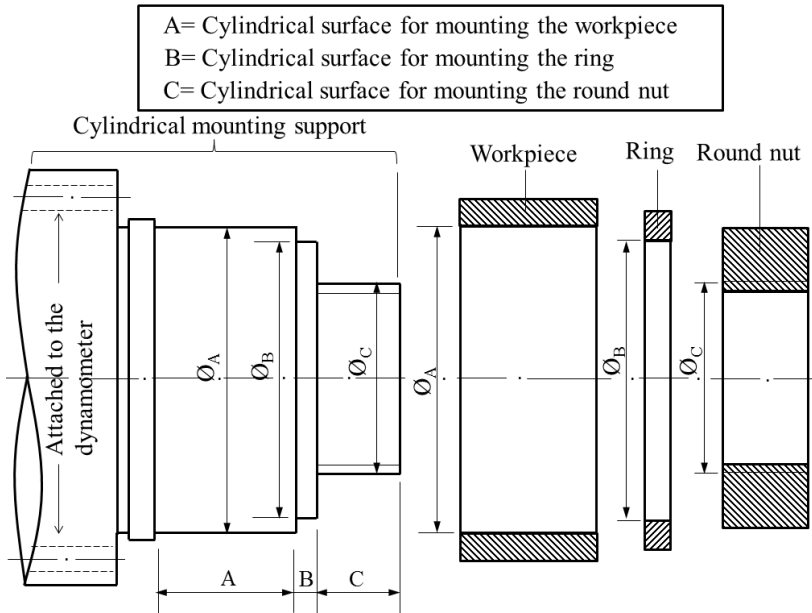
Source: Developed by the author and based on (ZIMMERMANN, 2013), (KIRCHGATTER, 2010), (KISTLER, 2010).

Figure A.2 shows the mounting and clamping of the workpiece inside the working chamber of the grinding machine by using the cylindrical mounting support. The enclosed dynamometer is mounted on the headstock of the grinding machine and directly attached to the cylindrical mounting support of the workpiece.
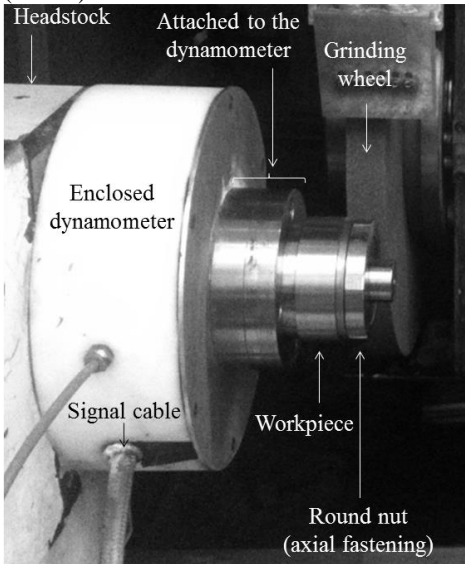
Figure A.2 – Mounting and clamping of the workpiece during the Scratch Experiments regarding the Dynamic In-process Characterization Method (DICM).

Source: Developed by the author and based on (ZIMMERMANN, 2013), (KIRCHGATTER, 2010), (KISTLER, 2010).

APPENDIX B – Preparation of Grinding Wheel´s Replicas

The preparation of the grinding wheel´s replicas was initially carried out inside the working chamber of the grinding machine by maintaining the tool static. Firstly a coarse silicon-based material was pressed onto the periphery of the grinding wheel with the aid of a mounting support, Figure B.1-a.

After some minutes pressed onto the grinding wheel, the coarse silicon-based material represents an inverse replica of the grinding wheel, but only with a limited resolution. In order to get a replica with higher resolution, a fine gel-based material is deposited on the coarse silicon-based replica and once again pressed onto the grinding wheel´s periphery by using the same mounting support, Figure B.1-b. The required pressure during this procedure is accomplished by using the screw of the mounting support.

Figure B.1 – Preparation of the Grinding Wheel´s Replicas.
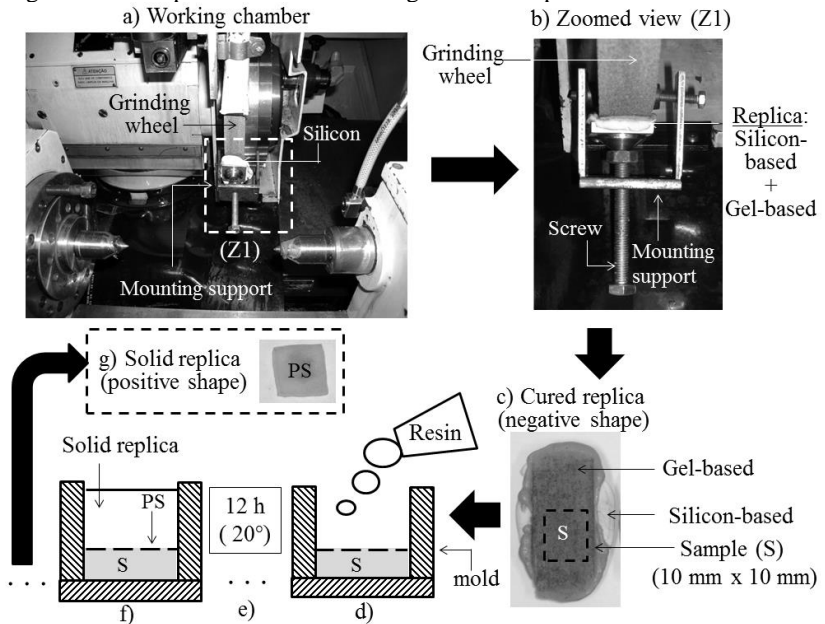
Source: (Developed by the author).

The replica is removed from the grinding wheel after cured and consists in a high defined negative shape of the grinding wheel´s topography, Figure B.1-c. Next, a sample "S" (length= 10 mm, width= 10 mm, thickness= 5 mm) is extracted from the replica, adopted in a solid mold, and a resin-based material is poured on it, Figure B.1-d. After pouring the resin-based material until it reaches the complete volume of the mold, the solution is set to solidify inside the mold. The stabilization of the solution takes about 12 hours and occurs in a separate room under controlled temperature (i.e., about 20°), Figure B.1-e. The cured and solid replica presents on its bottom surface the positive shape (PS) of the grinding wheel´s topography, which can be measured (Figure B.1-f, "PS"). The solid replica is extracted from the mold in order to measure its PS surface. Each solid replica has a cubic form (i.e., length= 10 mm, width= 10 mm, and thickness= 10 mm) and only the PS surface is measured, Figure B.1-g.

APPENDIX C – Mounting of the AE Transducers throughout the AE Tactile Scanning Experiments

Figure C.1 – Mounting of the AE transducer throughout the AE Tactile Scanning Experiments regarding the Dynamic Post-process Characterization Method (DPCM).
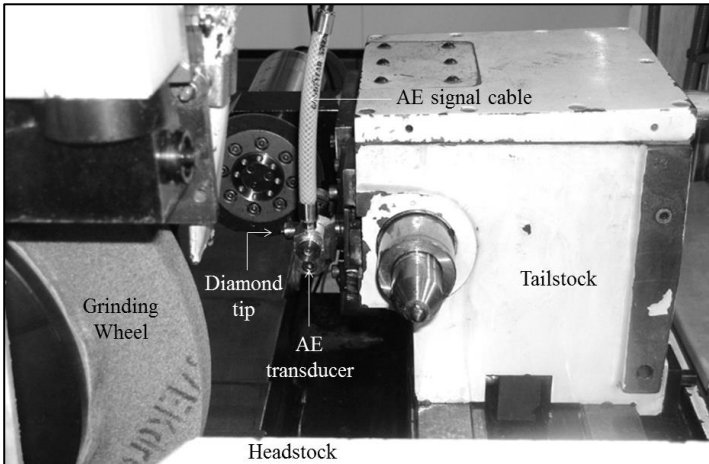
Source: (Developed by the author).

Figure C.2 – Mounting of the AE transducer throughout the AE Tactile Scanning Experiments regarding the Dynamic In-process Characterization Method (DICM).
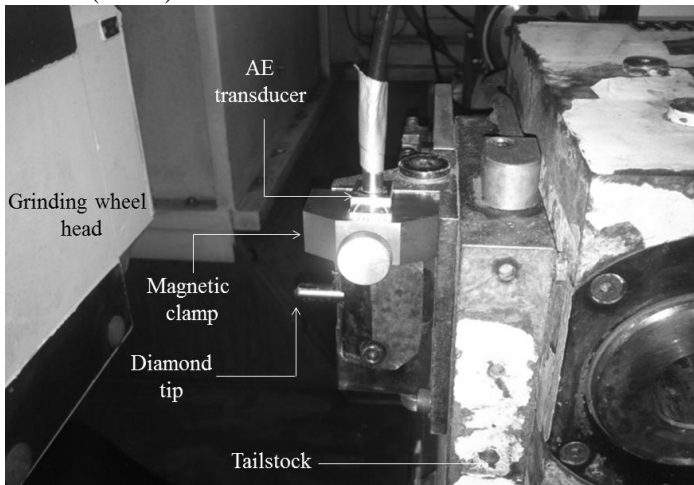
Source: (Developed by the author).

APPENDIX D – Evaluation of the Grinding Cutting Force Components (F_n and F_t)

During the Scratch Experiments regarding the DICM, the grinding cutting force (F) arises due to the interferences between the grinding wheel and the workpiece. Such grinding cutting force can be decomposed into two main grinding cutting force components: a) normal force component, F_n and; b) tangential force component, F_t. The evaluation of both F_n and F_t is based on the post-process analysis of the acquired force signals (i.e., F_x, F_y, and M_z) which are on-line measured (during the grinding process) by means of the rotating dynamometer.

The grinding cutting force component F_t is evaluated based on both the measured torque signal M_z (i.e., torque around the z-axis of the dynamometer) and on the workpiece diameter, d_w, Equation D.1, (KIRCHGATTER, 2010; KISTLER, 2010; ZIMMERMANN, 2013):

$$M_z = F_t \cdot r \tag{D.1}$$

Where (r) refers to the distance from F_t to the z-axis of the dynamometer so that (r) is equal to $d_w/2$. The utilization of M_z for assessing F_t is conceivable due to the fact that for each instant of time, the distance between the F_t source (i.e., interface between the grinding wheel and the workpiece) and the dynamometer´s z-axis is known. Additionally, this is also possible as the axes of both the workpiece and the dynamometer are aligned and concentric (KIRCHGATTER, 2010).

During idle process (i.e., no contact between the rotating grinding wheel and the rotating workpiece) as well as in the course of the grinding process, the Cartesian coordinate system of the dynamometer (x, y, and z) rotates. Therefore, the vectors of F_x and F_y also rotate. As the dynamometer and the workpiece are coupled and assembled aligned, the rotation of the workpiece (n_w) as well as the rotation of the workpiece´s support (n_{sup}) and the rotation of the dynamometer (n_{dyn}) are the same (i.e., $n_w = n_{sup} = n_{dyn}$).

When running idle (i.e., no contact between the rotating grinding wheel and the rotating workpiece, Figure D.1-a), the resulting force $F_{R,idle}$ denotes the sum of the forces related to the weight of the workpiece (F_W), to the weight of the mounting support (F_{sup}), (in which the workpiece is mounted), and to the force component F_x. By using the Pythagoras´ theorem the resulting force ($F_{R,idle}$) can be evaluated.

Figure D.1 – Evaluation of the grinding cutting force components (F_n and F_t).
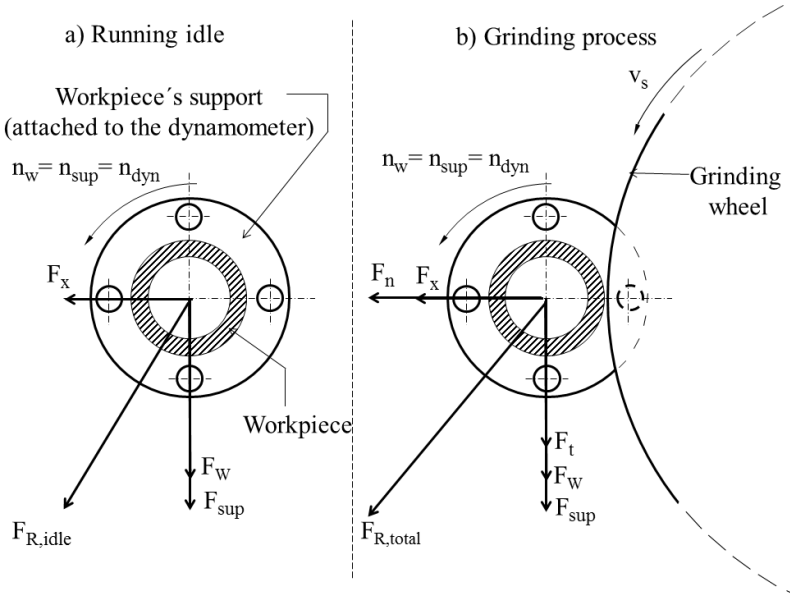
a) Running idle   b) Grinding process

Source: Developed by the author and based on (ZIMMERMANN, 2013), (KIRCHGATTER, 2010), (KISTLER, 2010).

On the other hand, in the course of the grinding process the total resulting force $F_{R,total}$ comprises the grinding cutting force components (F_n and F_t) as well as F_W and F_{sup}, Figure D.1-b. Due to the machine setup and the v_s direction used during the Scratch Experiments, the vectors F_W, F_{sup}, and F_t take effect in the same direction and hence might be added. By using the Pythagoras´ theorem, F_n is evaluated.

In order to achieve representative values of the grinding cutting force components, F_n and F_t are divided by the effective width of the grinding wheel (i.e., L_{eff}). This leads to the definition of the specific normal force (F'_n) and the specific tangential force (F'_t), respectively. The use of both F'_n and F'_t also allows improving comparability of experimental results (KÖNIG, 1989).

APPENDIX E – Fractional Factorial Analysis and Regression Models

The empirical models related to both the tangential and the axial scanning trajectories (and associated with the AE Tactile Scanning Experiments) were derived from a Statistical Fractional Factorial Analysis. This analysis relies on the evaluation of specific statistical parameters which were computed by means of the software Excel. The achieved empirical model consists in a regression model which takes into account the effect of the main influencing factors (i.e., factor T.S= Type of AE Signal, factor f_s= Sampling rate, and factor T_h= Threshold level) on the response N (i.e., AE oversteps). The values of N are obtained in-process (after grinding V'_w= 600 mm^3/mm) and are used as input data for the Fractional Factorial Analysis which is implemented out of the grinding process as a post-process analysis. For obtaining the experimental model the following procedure has been adopted:

a) Constructing the 2_{III}^{3-1} Fractional Factorial Design, (Appendix E.1).
b) Computing the ANOVA (Analysis of Variation) and its statistical related parameters, (Appendix E.2).
c) Defining the regression model, (Appendix E.3).
d) Model validation by analyzing the statistical parameters R^2, R^2-adjusted (Appendix E.4).

The upcoming sections describe the main statistical parameters and the procedure which has been adopted to obtain the empirical models.

APPENDIX E.1 - Constructing the 2_{III}^{3-1} Fractional Factorial Design

The Fractional Factorial Design used in the current research consists of the one-half fraction of a full 2^k design, where k denotes the number of factors under investigation and "2" denotes the number of levels for each factor. As three factors are considered (i.e., T.S, f_s, and T_h, see previous paragraph) and each factor presents two levels of variation (i.e., low= ↓, and high= ↑), the full 2^3 design leads to eight experimental runs, whereas the one-half fraction of such design (called as 2_{III}^{3-1} design, III= design resolution) leads to only four experimental

runs. The construction of the 2^{3-1}_{III} design is obtained by firstly writing down the full 2^2 factorial as the basic design, Table E.1, (MONTGOMERY, 2001).

Table E.1 – Construction of the basic design (2^2 factorial).

Experimental run	Treatment combination	Basic design	
		Factor T.S	Factor f_s
1	[1]	RMS	200
2	a	RAW	200
3	b	RMS	400
4	ab	RAW	400

Source: (Developed by the author).

The four possible experimental runs are represented by the numbers "1", "2", "3", and "4" and their related factor level combinations (also known as treatment combinations) are represented by [1], "a", "b" and "ab", respectively. By coding the factors´ levels (i.e., high level, ↑= +1 and low level, ↓ = -1), the previous table assumes the following content, Table E.2.

Table E.2 – Codification of the factors´ levels.

Experimental run	Treatment combination	Basic design	
		Factor T.S	Factor f_s
1	[1]	-1	-1
2	a	+1	-1
3	b	-1	+1
4	ab	+1	+1

Source: (Developed by the author).

Based on Table E.2, the column concerning the third factor (i.e., factor T_h) is obtained by equating the factor T_h to the two-factor interaction between T.S and f_s (i.e., T.S x f_s). Therefore, the levels of the factor T_h are easily obtained by multiplying the factor levels of both T.S and f_s in each row, Table E.3.

Table E.3 – Construction of the 2_{III}^{3-1} Fractional Factorial Design.

Experimental run	Treatment combination	Factor T.S	Factor f_s	Factor T_h
1	c	-1	-1	+1
2	a	+1	-1	-1
3	b	-1	+1	-1
4	abc	+1	+1	+1

Source: (Developed by the author).

The factor columns in Table E.3 can be considered as coded vectors. Two vectors are orthogonal if the sum of the products of their corresponding elements is "0" (zero). The notion of orthogonality is important in Design of Experiments (DoE) because it states whether the experimental effects are independent. Typically, the experimental analysis of an orthogonal design is straightforward because one can estimate each main effect and interaction independently. If the design is not orthogonal, the interpretation might not be as straightforward (MONTGOMERY, 2001). To show each factor column (i.e., vector) is orthogonal to the other factor columns, one only needs to multiply (T.S)x(f_s), (T.S)x(T_h), and (f_s)x(T_h) and sum the corresponded elements, Table E.4. As the total sum equals to "0", orthogonality does exist. Therefore, factor T.S is estimated independently from factor f_s and from factor T_h and vice versa.

Table E.4 – Orthogonality.

FACTORS			PRODUCTS		
T.S	f_s	T_h	T.S x f_s	T.S x T_h	f_s x T_h
-1	-1	+1	+1	-1	-1
+1	-1	-1	-1	-1	+1
-1	+1	-1	-1	+1	-1
+1	+1	+1	+1	+1	+1
TOTAL SUM			0	0	0

Source: (Developed by the author).

In order to allow getting an average representative response value, each experimental run ("a", "b", "c", and "abc") is replicated three times. Replicates are regarded as being multiple experimental runs with the same factor settings (levels). Hence, Table E.3 assumes the values shown in Table E.5, where "rep.1", "rep.2" and "rep.3" represent the first, the second and the third experimental replications, respectively.

Table E.5 – Replication of the experimental runs.

Experimental run	Treatment combination	Factor T.S	Factor f_s	Factor T_h
1(rep.1)	c	-1	-1	+1
1(rep.2)	c	-1	-1	+1
1(rep.3)	c	-1	-1	+1
2(rep.1)	a	+1	-1	-1
2(rep.2)	a	+1	-1	-1
2(rep.3)	a	+1	-1	-1
3(rep.1)	b	-1	+1	-1
3(rep.2)	b	-1	+1	-1
3(rep.3)	b	-1	+1	-1
4(rep.1)	abc	+1	+1	+1
4(rep.2)	abc	+1	+1	+1
4(rep.3)	abc	+1	+1	+1

Source: (Developed by the author).

For the sake of averaging out uncontrolled time-dependent effects that could arise in the course of the AE Tactile Scanning Experiments (i.e., machine warm up, machine vibrations, etc.) the experimental runs were completely randomized before carrying out the experiments. Such randomization of the twelve possible experimental runs also allows inferring the inherent variability of the response N (i.e., AE oversteps) obtained during the experiments (MONTGOMERY, 2001). Table E.6 and Table E.7 show the randomized experimental sequences which were used during the AE Tactile Scanning Experiments by employing the tangential and the axial scanning trajectories, respectively. The response column corresponds to the N values which are evaluated in-process through the AE Quick Test Method and instantaneously visualized on the laptop´s screen. The column "Rand. sequence" refers to the randomized numbers assigned to each factor level combination, whereas the column "Run sequence" shows the sequential order in which the factor level combinations (i.e., experimental runs) are carried out in the course of the experiments.

Table E.6 – Randomization during AE Tactile Scanning Experiments (Tangential scanning trajectory).

Coded Experimental runs and in-process AE oversteps (N)					
Rand. sequence	Run sequence	Factor T.S	Factor f_s	Factor T_h	Response (N)
10	1	+1	-1	-1	696
1	2	-1	-1	+1	4853
8	3	+1	+1	+1	2147
7	4	-1	+1	-1	273345
2	5	+1	-1	-1	1344
11	6	-1	+1	-1	510174
3	7	-1	+1	-1	407076
12	8	+1	+1	1	2368
6	9	+1	-1	-1	824
5	10	-1	-1	+1	20359
4	11	+1	+1	+1	510
9	12	-1	-1	+1	165765

Source: (Developed by the author).

Table E.7 – Randomization during AE Tactile Scanning Experiments (Axial scanning trajectory).

Coded Experimental runs and in-process AE oversteps (N)					
Rand. sequence	Run sequence	Factor T.S	Factor f_s	Factor T_h	Response (N)
4	1	+1	+1	+1	31367
2	2	+1	-1	-1	26448
10	3	+1	-1	-1	27505
7	4	-1	+1	-1	752109
8	5	+1	+1	+1	22285
11	6	-1	+1	-1	735409
5	7	-1	-1	+1	273504
9	8	-1	-1	+1	307388
12	9	+1	+1	+1	8864
1	10	-1	-1	+1	271483
6	11	+1	-1	-1	11975
3	12	-1	+1	-1	690896

Source: (Developed by the author).

APPENDIX E.2 - Computing the Analysis of Variation (ANOVA)

The evaluation of the Analysis of Variation (ANOVA) is based on the previous tables (i.e., Table E.6 and Table E.7) and aims at determining the factors influence on the response (N). Additionally, the ANOVA also provides information about the statistical significance among each of the influencing factors and their role on the N variability. Such analysis is achieved by computing specific statistical parameters: a) Degrees of Freedom (DF), b) Sum of Squares (SS), c) Mean Square (MS), d) Statistic-F, and e) P-value (MONTGOMERY, 2001).

In general, the parameter DF measures how much "independent" information is available to calculate each sum of squares (SS). The sum of squares (SS) measures the amount of variation in the response (N) that is attributable to each influencing factor. The mean square (MS) for each factor is simply the SS divided by DF. F-statistic is used to test whether the effect of a factor is significant. The F-statistic is also used to determine the p-value which is related to the appropriateness of rejecting the null hypothesis in a hypothesis test. If the P-value is less than or equal to the α-level selected previously to the experiments (i.e., α= 0,05), then the considered factor presents a significant effect on N. On the other hand, if the P-value is larger than the α-level, the factor´s effect is not significant. If a factor effect is significant, thus the level means for the factor are significantly different from each other (MONTGOMERY, 2001). Table E.8 and Table E.9 show the ANOVA results when employing the tangential and the axial scanning trajectories, respectively.

Table E.8 – Analysis of Variation (ANOVA)´s results (Tangential scanning trajectory).

Source	DF	SS	MS	F-Value	P-Value
Factor T.S	1	1,6 E+11	1,6 E+11	28,62	0,001
Factor f_s	1	8,3 E+10	8,3 E+10	15,22	0,005
Factor T_h	1	8,3 E+10	8,3 E+10	15,09	0,005
Error	8				
Total	11				

Source: (Developed by the author).

Table E.9 – Analysis of Variation (ANOVA)´s results (Axial scanning trajectory).

Source	DF	SS	MS	F-Value	P-Value
Factor T.S	1	7,0E+11	7,0E+11	1742,3	0,000
Factor f_s	1	1,5E+11	1,5E+11	361,8	0,000
Factor T_h	1	1,5E+11	1,5E+11	365,5	0,000
Error	8	3,2E+9	4,0E+8		
Total	11	9,9E+11			

Source: (Developed by the author).

APPENDIX E.3 - Defining the Regression Model

The definition of the regression model for both the tangential and the axial scanning trajectories is firstly based on the significant factors found previously by the ANOVA results. The ANOVA results show that the three considered factors are significant and do exert influence on N. Therefore, these factors need to be included in the regression model. Nonetheless, the significance of the three influencing factors is not meaningful without a prior analysis of the existing interactions among the factors´s levels (Section 6.7, Figure 69).

The regression model consists in an algebraic equation which can be used to represent the factorial design data set. Such equation describes the statistical relationship between the influencing factors and the response (N). The general form of the regression equation is as follows, Equation E.1 (MONTGOMERY, 2001):

$$Y = \beta_0 + \beta_1 x_1 + \beta_2 x_2 + \beta_3 x_3 + \epsilon \tag{E.1}$$

Where Y represents the response (i.e., AE oversteps, N), β´s are parameters whose values are to be determined, and x_1, x_2, and x_3 are coded variables that represent the factors T.S, f_s, and T_h, respectively. The coded variables are defined on a coded scale which assumes the values -1 (for the low factor level, ↓) and +1 (for the high factor level, ↑). The parameter β_0 corresponds to the average of all the N responses.

The β parameters in this regression model consist of the one-half value of the related factors´ effects. On the other hand, the factors´ effects are derived from the evaluation of the statistical parameter "contrast". The parameter "contrast" for each influencing factor is obtained by assessing the linear combination between the contrast

coefficients (i.e., the factor columns in Table E.6 and Table E.7) and their associated responses (N) (MONTGOMERY, 2001).

Table E.10 and Table E.11 show the evaluated factors´ effects and coefficients related to the tangential and the axial scanning trajectories, respectively.

Table E.10 – Factors´ effects and coefficients (Tangential scanning trajectory).

Factors	Effect	Coefficient
T.S	-228947	-114474
f_s	166963	83482
T_h	-166243	-83121

Source: (Developed by the author).

Table E.11 – Factors´ effects and coefficients (Axial scanning trajectory).

Factors	Effect	Coefficient
T.S	-483724	-241862
f_s	220438	110219
T_h	-221575	-110788

Source: (Developed by the author).

Based on the coefficients shown in Table E.10 and Table E.11, the regression equations for both the tangential and axial scanning trajectories are achieved, Equation E.2 and Equation E.3, respectively:

$$N_{TAN} = 115788 - 114474 \, (T.S) + 83482 \, (f_s) - 83121 \, (T_h) \qquad (E.2)$$

$$N_{AX} = 263269 - 241862 \, (T.S) + 110219 \, (f_s) - 110788 \, (T_h) \qquad (E.3)$$

The constants $C_{TAN} = 115788$ and $C_{AX} = 263269$ express the overall N mean values related to the twelve experimental runs when employing the tangential and the axial scanning trajectories, respectively. The factors´ coefficients in each equation represent the influence of each isolated factor on N, by holding constant all the other influencing factors in the equation. The sign of each coefficient indicates the "direction" of the relationship, that is, if there exists either direct correlation (i.e., sign "+") or inverse correlation (i.e., sign "-") between the considered factor and the response N. For example, in Equation E.2, for each 1 kS/s increase in the factor f_s, N_{TAN} increases by 83482 digitized oversteps. On the contrary, for each 1 V increase in the factor T_h, N_{TAN} decreases by 83121 digitized oversteps.

APPENDIX E.4 – Regression Model Validation

The previous empirical models represented by both Equation E.2 and Equation E.3 are validated by analyzing the statistical parameters R^2 and R^2_{adj}. The parameter R^2 describes the amount of variation in the observed response values (i.e., AE oversteps, N) that is explained by the influencing factors (also known as predictors). R^2 increases with additional predictors. Therefore, R^2 is most useful when comparing models of the same size. The parameter R^2 is defined by Equation E.4, (MONTGOMERY, 2001):

$$R^2 = 1 - \frac{SS_E}{SS_T} \tag{E.4}$$

Where SS_E is the error sum of squares and SS_T refers to the total sum of squares. The statistical parameter R^2_{adj} is a modified R^2 that is adjusted to the number of terms in the model. Unlike R^2, R^2_{adj} may get smaller when unnecessary factors are added to the model. Therefore, R^2_{adj} is useful for comparing models with different numbers of factors. When both R^2_{adj} and R^2 expressively diverge, there is a good chance that the factors included in the model are not significant. The parameter R^2_{adj} is defined by Equation E.5 (MONTGOMERY, 2001):

$$R^2_{adj} = 1 - \left(\frac{n-1}{n-p}\right)\left(1 - R^2\right) \tag{E.5}$$

Where "p" is the number of factors in the model including the constant term. Table E.12 and Table E.13 show the evaluated values of R^2 and R^2_{adj} when considering both the tangential and the axial scanning trajectories, respectively. The evaluated values show that both models can be considered suitable to model N. Additionally, as the R parameters (i.e., R^2 and R^2_{adj}) for each model present close values among each other, the amount of influencing factors is considered relevant to model N based on the collected experimental data (MONTGOMERY, 2001).

Table E.12 – Model adequacy (Tangential Scanning Trajectory).

Statistical parameter R^2	Statistical parameter R^2_{adj}
88,05%	83,56%

Source: (Developed by the author).

Table E.13 – Model adequacy (Axial Scanning Trajectory).

Statistical parameter R^2	Statistical parameter R^2_{adj}
99,68%	99,56%

Source: (Developed by the author).